

**FABRICATION AND STUDY OF ITO THIN FILMS
PREPARED BY MAGNETRON SPUTTERING**

Dissertation

zur Erlangung des Grades
Doktor der Naturwissenschaften
(Dr. rer. nat.),
vorgelegt am Fachbereich Physik der
Universität Duisburg-Essen

von

Zhaohui Qiao

aus

Hebei, V. R. China

Erstgutachter: Prof. Dr. D. Mergel

Zweitgutachter: Prof. Dr. V. Buck

Tag der mündlichen Prüfung: 08 Mai 2003

Content

1	Introduction	1
2	Background Theory and Literature Review	3
2.1	Introduction to ITO Films	3
2.2	Crystal Structure	3
2.3	Electrical Properties of ITO Films	4
2.3.1	Free Carrier Density.....	5
2.3.2	Free Carrier Mobility	7
2.4	Optical Properties	9
2.4.1	Optical Constants.....	9
2.4.2	Band Structure	10
2.5	Deposition Techniques of ITO	12
2.5.1	Thermal Evaporation.....	12
2.5.2	Spray Hydrolysis (Pyrolysis)	13
2.5.3	Chemical Vapor Deposition	14
2.5.4	Sputtering.....	15
2.6	Effects of Deposition Parameters on the Properties of ITO Films for Sputter Techniques	21
2.6.1	Substrate Temperature	21
2.6.2	Oxygen Partial Pressure	22
2.6.3	Target-Substrate Distance	23
2.6.4	Total Pressure.....	25
2.6.5	Sputtering Power	26
2.6.6	Post-Annealing.....	27
2.6.7	Structure Zone Models.....	28

3	Preparation of ITO Thin Films	30
3.1	Deposition Equipment.....	30
3.1.1	Process Chamber	31
3.1.2	Vacuum System.....	31
3.1.3	DC-Sputtering System	31
3.1.4	RF-Sputtering System.....	32
3.2	Experiment Method and Procedures	34
3.3	Substrate Temperature.....	34
4	Characterization of ITO Films	36
4.1	Measurement of the Mass of the Films.....	36
4.2	Determination of the Film Thickness	37
4.2.1	Stylus Method-Profilometer.....	37
4.2.2	Optical Spectrum Simulation.....	38
4.3	Measurement of Transmittance and Reflectance Spectra.....	39
4.3.1	Principle	39
4.3.2	The Approach to the Spectra Measurement.....	39
4.3.3	Measuring Results	42
4.4	Determining the Structure of ITO Films by X-ray Diffraction.....	43
4.4.1	Information Obtained from the X-ray Diffractogram.....	43
4.4.2	Evaluating X-ray Diffractograms by Computer Program.....	45
4.5	Determining the Electrical Resistivity of the Films	46
4.6	Measuring the Surface Morphology by AFM	47
5	Results and Discussions	50
5.1	Dielectric Modeling of Optical Spectra	50
5.1.1	General Method	50
5.1.2	Results for ITO Films	54
5.1.3	Results for SrTiO ₃ Films.....	64

5.1.4	Results for TiO ₂ Films	69
5.2	DC Magnetron Sputtered ITO Films	74
5.2.1	Effect of Lattice Distortion on the Properties of ITO Films	74
5.2.2	Effect of Sputter Geometry and Plasma Distribution on the Structural and Electrical Properties of ITO Films	84
5.2.3	Effect of the Film Thickness on the Properties of ITO Films	94
5.3	RF-sputtered ITO Films	107
5.3.1	Method of the Experiments	107
5.3.2	Results and Discussion (comparing with dc-sputtered films).....	107
6	Conclusions	118
7	Summary	124
7.1	Summary (in English)	124
7.2	Zusammenfassung (in German)	130
8	References	135
9	Acknowledgments	146

List of Figure

Figure 2-1	Two non-equivalent sites of In atoms in In_2O_3 crystal	4
Figure 2-2	Dependence of the free-electron density N_e on the Sn concentration	6
Figure 2-3	Transmittance and reflectance of the ITO film with thickness of $1.656 \mu\text{m}$	9
Figure 2-4	Dielectric constant and refractive index of the ITO film	10
Figure 2-5	Assumed parabolic band structure of undoped In_2O_3 and the effect of Sn doping	11
Figure 2-6	Schematic diagram of the spray hydrolysis apparatus	13
Figure 2-7	CVD system for preparation of ITO films	14
Figure 2-8	Interactions of ions with surfaces	15
Figure 2-9	Schematic diagram of a dc sputtering system	17
Figure 2-10	Voltage distribution in a dc glow discharge process	17
Figure 2-11	Schematic illustrations of the (a) convention dc-diode and (b) planar magnetron cathode sputtering	19
Figure 2-12	Three different mechanisms for reactive sputter deposition	20
Figure 2-13	Relative configuration of target, substrate, and virtual source	24
Figure 2-14	Schematic representation of the influence of substrate temperature and argon working pressure on the structure of metal coatings deposited by sputtering	29
Figure 3-1	Schematic diagram of the construction of the LA 500S system	30
Figure 3-2	Interface of the control software WICON of the system	31
Figure 3-3	The constructure of ITO target (PPS 90)	32
Figure 3-4	Function layout of the sputtering system	33
Figure 3-5	Schematic illustration of the substrate holder	35
Figure 4-1	The diagram of the principle of the spectrometer	39
Figure 4-2	Variable-angel reflectance accessories (a) is installed in the sample cell, (b) is mounted in the reference cell	40

Figure 4-3	Sketch of the optical path of B008-6703, Angel 6°	41
Figure 4-4	The measured transmittance curve and the modified and calculated reflectance curve of quartz	42
Figure 4-5	The (222)-reflex of XRD for an ITO film	44
Figure 4-6	Reflection of x-rays from a crystal	44
Figure 4-7	Schematic of in-line four-point probe configuration	47
Figure 4-8	Working principle of the AFM	48
Figure 5-1	Band gap assumed by OJL model	51
Figure 5-2	Experimental transmittance spectrum and its simulation with the standard and the modified dielectric model	55
Figure 5-3	Dielectric function (real and imaginary part) used to simulate the spectrum shown in Figure 5-2, calculated with the standard and the modified model	56
Figure 5-4	Frequency dependent damping factor $\Gamma_{Dr}(1/\lambda)$ for four representative samples	57
Figure 5-5	Band gap energies as a function of $N_{Dr}^{2/3}$, with N_{Dr} being the optically determined carrier density	59
Figure 5-6	Value of the dielectric function at 550 nm and its contributions from free carriers (Drude term), ϵ_{Dr} , band gap transition, ϵ_{BG} , and bulk interband transition, ϵ_{HO} , modeled by a harmonic oscillator. ϵ_{inf} designates all contribution except the Drude term	59
Figure 5-7	Square of the Drude frequency Ω_{Dr}^2 for various models of the plasma edge as a function of the electrically determined electron density n_{dc}	61
Figure 5-8	Optically determined mobilities M_{Dr} vs. direct current mobility μ_{dc}	62
Figure 5-9	Fitting results for STO-A with standard dielectric model	66
Figure 5-10	Fitting result for STO-B with standard dielectric model	66
Figure 5-11	Fitting results for STO-B with modified models	67
Figure 5-12	Experimental and simulated spectra with standard model for STO films: (a) Sr2b, (b) Sr6b	68
Figure 5-13	Fitting results for Sr6b with improved models (adding an additional harmonic oscillator to the standard model)	68

Figure 5-14	Experimental and simulated spectrum with standard models for evaporated TiO ₂ film: (a)TiQ, (b)TiG	71
Figure 5-15	Simulation results for TiG with modified model (introducing a Drude term to the standard model)	72
Figure 5-16	Experimental and simulated spectra with standard models for sputtered TiO ₂ films: (a) R9, (b) R1	72
Figure 5-17	Lattice distortion $\Delta d/d_0$ for the various deposition parameters	74
Figure 5-18	Grain size D_g (“vertical grain diameter”) against $\Delta d/d_0$	75
Figure 5-19	Transmittance and reflectance of ITO films together with their simulation curves (the white lines)	75
Figure 5-20	Electron density N_{Dr} , evaluated from the plasma edge, against (a) q_{O_2} (b) $\Delta d/d_0$	76
Figure 5-21	Electron mobility and its reciprocal ($1/M_{Dr}$), as evaluated from the plasma edge, against (a) N_{Dr} and (b) $\Delta d/d_0$	77
Figure 5-22	Optical transmittance ($\lambda = 550$ nm) against the electron density N_{Dr} . The curve serves as a guide to the eye	77
Figure 5-23	Surface roughness derived from the AFM measurement against $\Delta d/d_0$..	78
Figure 5-24	Conductivity σ_{Dr} , as calculated from N_{Dr} and M_{Dr} , against direct current conductivity σ_{dc}	79
Figure 5-25	XRD peak width against the corresponding reflex tangent angle.....	81
Figure 5-26	Statistical rms strains against average lattice distortion.....	82
Figure 5-27	Line width as a function of $\sin\theta$	83
Figure 5-28	Refractive index (550 nm) as a function of N_{Dr}	83
Figure 5-29	Sketch of the deposition geometry (to scale). Top: cross section; Bottom: top view.....	84
Figure 5-30	Thickness profiles of a centrally and a peripherally positioned film.....	85
Figure 5-31	Deposition rate, defined as mass equivalent thickness d_m , as a function of the oxygen partial pressure q_{O_2}	86
Figure 5-32	Packing density ρ_p of the films as a function of the oxygen admixture q_{O_2} to the sputter gas	87
Figure 5-33	XRD patterns for films sputtered with Ar	88
Figure 5-34	XRD patterns for films sputtered with Ne	88

Figure 5-35	Lattice distortion $\Delta d/d_0$ as a function of the oxygen admixture q_{O_2} to the sputter gas	89
Figure 5-36	AFM micrographs (500×500 nm) of the (a) central and (b) peripheral sample prepared in the same run (Ar, $q_{O_2} = 0.33\%$, 400°C), and (c) the profile of the sample shown in (b) along the horizontal direction	90
Figure 5-37	Profile of the peripheral sample (Ne, $q_{O_2} = 4\%$) with low packing density of 0.82	90
Figure 5-38	Electrical resistivity ρ_e as a function of q_{O_2}	91
Figure 5-39	Electrical resistivity ρ_e as a function of the average lattice distortion $\Delta d/d_0$	92
Figure 5-40	Deposition rate as a function of d_m	95
Figure 5-41	The intensity of XRD peak from the quartz substrate as a function of the film thickness coated on it	95
Figure 5-42	Mass density as a function of d_m	96
Figure 5-43	X-ray spectra of samples with different thickness	96
Figure 5-44	Lattice distortion as a function of d_m	97
Figure 5-45	Grain size (left) and inhomogeneous microstrain (right) as a function of d_m	97
Figure 5-46	Texture as a function of d_m for (a) central (hw) (b) peripheral (hw) (c) central (hw^3) (d) peripheral (hw^3) samples	98
Figure 5-47	Intensity ratio of $I(222)/I(400)$ as a function of d_m (the intensity is derived from hw^3 (left) and hw (right))	99
Figure 5-48	Transmittance and reflectance of films with $d_m = 0.2, 1, \text{ and } 1.75 \mu\text{m}$ together with simulated curves which is shown as a white line inside the experimental curves	99
Figure 5-49	Carrier density and Drude mobility as a function of d_m	100
Figure 5-50	Band gap and refractive index (at 550 nm) as a function of d_m	101
Figure 5-51	Electrically and optically derived electrical resistivity as a function of d_m	102
Figure 5-52	Surface roughness as a function of d_m	102
Figure 5-53	AFM images ($2 \times 2 \mu\text{m}$) of film surface morphology. (a) $0.3 \mu\text{m}$, ce; (b) $1 \mu\text{m}$, ce; (c) $1 \mu\text{m}$, pe	102

Figure 5-54	The scattering power of four representative peaks in ITO films as a function of d_m by means of hw^3 (left) and hw (right) 104
Figure 5-55	SEM micrographs of the cross section of ITO films with the thickness of 0.65 μm (a) and 1.35 μm (b) 105
Figure 5-56	Comparison of the physical properties of dc and rf sputtered ITO films. (a) The deposition rate, (b) mass density, (c) band gap, (d) free carrier density (e) carrier mobility, (f) electrical conductivity as a function of q_{O_2} 108
Figure 5-57	Conductivity σ_{Dr} , as calculated from N_{Dr} and M_{Dr} , against direct current conductivity σ_{dc} (The symbols have their usual meanings) 110
Figure 5-58	X-ray diffraction patterns for ITO films prepared by rf sputtering 111
Figure 5-59	X-ray diffraction patterns for ITO films prepared by dc sputtering 112
Figure 5-60	The grain size as a function of the average lattice distortion 114
Figure 5-61	The average vertical grain size and surface roughness (rms) as a function of packing density for dc- and rf-sputtered ITO films 115
Figure 5-62	Lateral grain size versus vertical grain size for rf-sputtered ITO films.... 115
Figure 5-63	(a) AFM image ($1 \times 1 \mu\text{m}$) of central film prepared by rf 400 W at $q_{O_2} = 0\%$ (b) the profile along the direction shown by the straight line in the AFM image 116
Figure 5-64	AFM images ($1 \times 1 \mu\text{m}$) of the ITO central films prepared with $q_{O_2} = 1\%$ by (a) rf 400 W and (b) rf 100 W 117
Figure 5-65	(a) AFM image ($2 \times 2 \mu\text{m}$) of central film prepared by dc 200 W at $q_{O_2} = 2\%$ and (b) the profile along the direction shown by the straight line in the AFM image 117
Figure 7-1	The photo of SrTiO_3 and TiO_2 thin films 128
Figure 7-2	The photo of ITO thin films 129

List of Tables

Table 4-1	The possible errors and actions for high-precision mass determination ..	36
Table 4-2	The wavelength (range) and the reflectance of the standard high reflectance mirror (Perkin Elmer AG)	42
Table 4-3	Evaluation of the computer program by comparing it with the manually results (the parameters input to the program is 5; 8; 8; 20)	46
Table 5-1	Nomenclature	53
Table 5-2	Physical properties of SrTiO ₃ (Bürger 2000)	64
Table 5-3	Fitting parameters for sample STO-A and STO-B simulated with standard and modified (in shadowing) dielectric models.....	65
Table 5-4	Fitting parameters for Sr2b and Sr6b with standard and modified (in shadowing) dielectric model	68
Table 5-5	Physical properties of TiO ₂ (Mergel et al 2000; Schenkel 1998).....	70
Table 5-6	Fitting parameters for TiQ and TiG with standard and modified (in shadowing) dielectric model	71
Table 5-7	Fitting parameters for R9 and R1 with standard and modified (in shadowing) dielectric model	73
Table 5-8	The main deposition conditions.....	85
Table 5-9	Lattice distortion, at $q_{O_2} = 1\%$ if not stated otherwise.....	88
Table 5-10	Grain size at $q_{O_2} = 1\%$ if not stated otherwise	89
Table 5-11	Deposition conditions of rf and dc sputtered samples (the deposition rates listed in the table belong to the central samples with $q_{O_2} = 0\%$)....	107
Table 5-12	Average grain size (D_g) and lattice distortion ($\Delta d/d_0$) for rf-sputtered ITO films	113
Table 5-13	Average grain size (D_g) and lattice distortion ($\Delta d/d_0$) for dc-sputtered ITO films	113

1 Introduction

The term “transparent conducting oxide (TCO)” refers to heavily doped oxide semiconductors that have a band gap sufficiently large (≥ 3 eV) to make them transparent over the visible spectral range and a conductivity high enough such that they exhibit metal like behavior. Due to their high conductivities, the films also show high reflectivity in the near infrared.

During the last thirty to forty years, the dominant TCOs have been tin oxide (SnO_2), indium oxide (In_2O_3), indium tin oxide ($\text{In}_2\text{O}_3:\text{Sn}$ or ITO), and zinc oxide (ZnO) (Coutts et al 1999), which have found applications in wide areas of electronic and optoelectronic fields.

Stoichiometric In_2O_3 is a transparent intrinsic semiconductor that can be doped by substituting Sn for In to yield *n*-type indium tin oxide (ITO), a well-known transparent semiconductor. ITO films are particularly attractive in applications such as liquid crystal displays, transparent electrodes of solar cells, and photodetectors. For these applications, the typical parameters required by high-quality ITO films are known as that the electrical resistivity is below $200 \mu\Omega\text{cm}$ and simultaneously the optical transmittance is 80 - 95% averaged over the visible spectrum. Nowadays, a great deal of efforts has been carried out both on the fundamental theory of the material and the preparation technology.

Investigations of the various manufacturing techniques have been developed to meet both economic and technological demands (Bel Hadja Tahar et al 1998). So far, high quality ITO films have been prepared by various deposition methods such as vacuum evaporation, dc and rf sputtering, rf ion plating, spray pyrolysis, sol-gel reaction and chemical vapor deposition (CVD). Among these methods, the magnetron sputtering is widely used in making ITO films for display devices since the method is superior in its controllability, high deposition rate and the film obtained by this method shows good uniformity over wide area on large size substrates (Meng 1996).

The electrical characteristics of ITO films are dependent on the presence of oxygen vacancies and substitutional tin atoms. Because a compromise between electrical conductivity and optical transmittance is encountered for an ITO film, a careful balance between the properties is required. Reduction of the resistivity involves either an increase in the carrier concentration or in the mobility.

Increasing the former also leads to an increase in the visible absorption. Increasing the mobility, however, has no deleterious effect and is probably the best direction to follow (Coutts et al 1999).

The optical and electrical properties of the films are intimately associated with microstructure and lattice defects of the films which, in turn, are dependent on the deposition method used and the process conditions, such as the oxygen partial pressure, the substrate temperature, the sputter power, etc. To characterize the optical and electrical properties of the films is also an important task in practice. The optical properties of a material are described through the dielectric function ($\varepsilon = \varepsilon_1 + i\varepsilon_2$). Some parameters of the films can be as well derived from the dependency of the dielectric function on the wavelength (Weijtens and Van Loon 1991).

To date, much effort has been focused on methods for the deposition of ITO with lower resistivity, and studies of the effect of Sn doping and film crystallinity (Shigesato, Paine and Haynes 1993). Sputtering yields a minimum film resistivity $\rho_{\min} = 115 \mu\Omega\text{cm}$ (Latz, Michael and Scherer 1991) or $130 \mu\Omega\text{cm}$ (Joshi, Singh and McClure 1995) when using direct current (dc) or radio-frequency (rf) power, respectively.

In this work, the ITO films were prepared by rf and dc magnetron sputtering methods. Films were deposited under various conditions. The main tasks of this dissertation can be focused on two aspects: studying the growth of the ITO films and investigating the correlation between the microstructure and the electrical and optical properties of the films; modeling the dielectric function of semiconductors ($\text{In}_2\text{O}_3:\text{Sn}$) and insulators (SrTiO_3 and TiO_2). The layout of the dissertation is arranged as follows:

In this dissertation the background theory and the relevant literature review are presented in the section 2. This is followed, in section 3, by a description of the equipment used to fabricate the ITO films, while section 4 consists of the details of the measurement and analysis techniques for characterizing the films. Section 5 contains the results and discussion of this research which are classified into two main parts, i.e. the dielectric modeling of the thin films (involving ITO, SrTiO_3 and TiO_2) and the experimental findings concerning the relation between the microstructure and the film properties; the effect of the sputtering geometry and the plasma distribution, and film thickness on the film properties of ITO films; comparison of the rf and dc sputtered ITO films. Finally, the conclusion and summary (in English, German and Chinese) of the work are presented in section 6 and section 7, respectively. The references cited by this dissertation are listed in section 8.

2 Background Theory and Literature Review

2.1 Introduction to ITO Films

$\text{In}_2\text{O}_3:\text{Sn}$ (also called indium tin oxide or ITO) is a well-known transparent conducting oxide (TCO). It is a highly degenerate n -type wide gap semiconductor that is produced by doping Sn atoms in In_2O_3 . Since ITO films have a high transmittance in the visible range and a high conductivity simultaneously, they are widely used in a variety of electronic and optoelectronic fields, such as liquid crystal displays (Latz, Michael and Scherer 1991), solar cells (Kobayashi et al 1992), photodiodes (Kim et al 1998) and antistatic coatings (Löbl, Huppertz and Mergel 1996). For typical high-quality ITO films, the transmittance is above 90% in the range of 400 - 700 nm and the electrical resistivity is below 200 $\mu\Omega\text{cm}$.

$\text{In}_2\text{O}_3:\text{Sn}$ films show an interesting and technologically important combination of properties: they have high luminous transmittance, high infrared reflectance, good electrical conductivity, excellent substrate adherence, hardness, and chemical inertness (Hamberg and Granqvist 1986). So far, many techniques have been developed to prepare ITO films. And it is known that both the optical properties and the electrical properties are strongly dependent on the deposition parameters in every process.

2.2 Crystal Structure

In_2O_3 crystallizes to form the bixbyite structure (also called the C-type rare-earth oxide structure, space group $T_h^7 Ia3$) (Galasso 1970). The lattice parameter is 1.0117 nm and the density is 7.12 g/cm^3 . Conventional unit cell consists of 16 formula units of In_2O_3 , which shows a fluorite-related superstructure where one-fourth of the oxygen anions located along the four $\langle 111 \rangle$ axes are missing. Indium cations are located in two non-equivalent (see Figure 2-1), where 8 In^{3+} ions are located in the center of trigonally distorted oxygen octahedrons (b site) and the remaining 24 In^{3+} ions are located in the center of the more distorted octahedrons (d site) (Nadaud et al 1998).

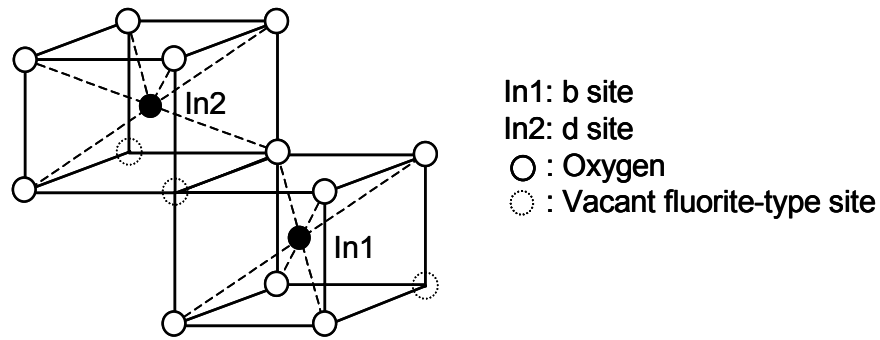


Figure 2-1 Two non-equivalent sites of In atoms in In_2O_3 crystal

Indium tin oxide is essentially formed by substitutional doping of In_2O_3 with Sn which replaces the In^{3+} atoms from the cubic bixbyite structure of indium oxide. And it was found that tin atoms preferentially occupy the less distorted b lattice sites in the expanded In_2O_3 lattice (Nadaud et al 1998; Yamada et al 1999).

For practical electronic structure calculations, a primitive unit cell containing 40 atoms was used. For the analysis of Sn-doped In_2O_3 a primitive unit cell similar to that of In_2O_3 crystal was used: For the supercell calculation, one of the indium atoms at the 8b or 24d site was replaced by a Sn atom, which led to a system with a 2.5 at.% concentration of Sn, and approximately $1 \times 10^{21}/\text{cm}^3$ concentration of free electrons should have appeared if all the substituted Sn atoms had donated free electrons (Odaka et al 2001). This theoretical result is in agreement with ITO films with very low resistivity, which are known to have about $1 \times 10^{21}/\text{cm}^3$ concentration of free electrons by some experimental methods (Shigesato, Hayashi and Haranoh 1992; Frank and Köstlin 1982). It implies that this supercell model seems to be a good approximation of real ITO films with very low resistivity.

It has been detected by Nadaud et al (1998) that the tin doping (up to 5 - 6% Sn) leads to an increase in the lattice constant of about 0.05% though the Sn^{4+} ionic radius (0.71 Å) is smaller than that of In^{3+} (0.81 Å).

2.3 Electrical Properties of ITO Films

Electrical properties of ITO films can be characterized by free carrier density n_e , carrier mobility μ , and electrical conductivity σ or resistivity ρ_e in the films. The relations among these quantities are as follows:

$$\sigma = n_e \mu e, \quad (2.3.1)$$

$$\sigma = 1 / \rho_e, \quad (2.3.2)$$

where e is the electron charge. In order to obtain films with high conductivity, high carrier concentration and mobility should be simultaneously realized.

2.3.1 Free Carrier Density

2.3.1.1 Defect models

In ITO films, the free carriers come from two different mechanisms: substitutional tetravalent tin atom and divalent oxygen vacancies. The free carrier density is governed by defects introduced in the bixbyite structure. The most famous work on this issue was done by Frank and Köstlin (1982). They carried out extensive experiments and analyses on films with varying Sn contents prepared by chemical vapor deposition (spray pyrolysis) and treated in oxidizing and reducing atmospheres. According to their results, the following five dominating lattice defects are summarized:

(1) Impurity ions –substitutional tin (Sn^*)

Tin acts as a cationic dopant in the In_2O_3 lattice and substitutes the indium. In In_2O_3 , since indium has a valence of three, the tin doping results in n -type doping of the lattice by providing an electron to the conduction band. Therefore, the overall charge neutrality is preserved.



where the superscript * stands for the positive charge.

(2) Neutral defect ($\text{Sn}_2^* \text{O}_i''$)

When two Sn^{4+} ions which are not on nearest neighbour positions loosely bound to an interstitial oxygen anion, a neutral compound of $\text{Sn}_2^* \text{O}_i''$ is formed. This interstitial defect dissociates on annealing under reducing conditions and O_i can drift out ($\text{Sn}_2^* \text{O}_i'' \Leftrightarrow 2\text{Sn}^* + 2e^- + 1/2\text{O}_2^{(g)}$). So this kind of defect is no “harmful”.



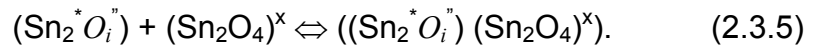
Here, O_i^{\times} is interstitial oxygen. The superscript “ \times ” stands for two negative charges.

(3) Neutral defect (Sn_2O_4) $^{\times}$

When two nearest-neighbour Sn^{4+} ions bound to three nearest neighbours on regular anion sites and an additional interstitial oxygen ion on nearest quasianion site, the $(\text{Sn}_2\text{O}_4)^{\times}$ which has a structure like Ca_2F_4 is formed. This case occurs at high doping level. Since the Sn–O bond is strong, it can not be reduced by heat treatment. Hence it is a “harmful” effect.

(4) Defect ($\text{Sn}_2^* \text{O}_i''$)(Sn_2O_4) $^{\times}$

Associate composed of the above two mentioned defects, containing loosely as well as strongly bound surplus oxygen. This neutral defect is a common phenomenon in very highly doped system.



(5) Oxygen vacancy V_{O}^{**}

The oxygen vacancies act as doubly ionized donors and contribute at a maximum two electrons to the electrical conductivity as shown in the following equation (Bel Hadja Tahar et al 1998):



Deposition in an oxygen-rich ambient will result in a film which is saturated with oxygen. Increasing temperature will shift both equilibrium Eq. (2.3.4) and (2.3.5) to the left, creating free electrons and dissolving interstitial oxygen and substitutional Sn. Interstitial oxygen (O_i) can diffuse through the ITO lattice and reach the grain boundaries. At the grain boundaries absorbed oxygen ($\text{O}_2(a)$) can be formed and desorbed. Of course, depending on the ambient, the reactions can also be reversed.

2.3.1.2 Limitation of free carrier density

The free carrier density changing with the concentration of the Sn dope is shown in Figure 2-2 (Köstlin, H. Jost, R. and Lems, W. 1975).

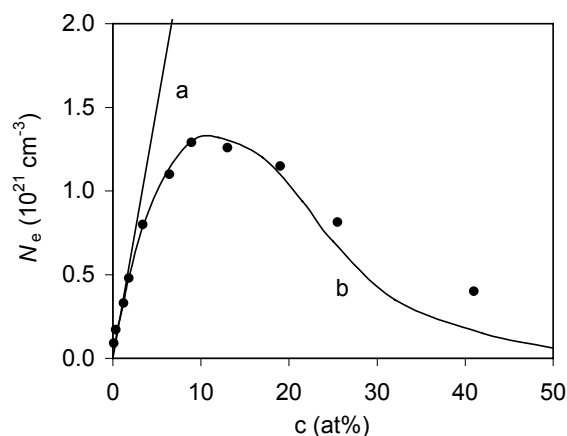


Figure 2-2 *Dependence of the free-electron density N_e on the Sn concentration c . Dots represent experimental points; drawn curves represent (a) $N_{\text{In}}c$, (b) $N_{\text{In}}c(1-c)^8$, where N_{In} is the concentration of indium site in In_2O_3 and c the concentration of Sn relative to all metal atoms (Köstlin, H. Jost, R. and Lems, W. 1975)*

In ITO films the theoretical maximum carrier density N_e due to only Sn doping is $N_e = N_{In} \times c$, where $N_{In} = 3.0 \times 10^{22} \text{ cm}^{-3}$ is the concentration of In atoms, c is the tin concentration. However, practically the carrier concentration does not increase as expected. As can be seen in Figure 2-2, only at very low Sn concentration ($c < 4 \text{ at.}\%$) the free carrier density follows a straight line (curve a), indicating that every substitutional tin atom acts as a donor which sponsors one free electron to the matrix. At higher Sn content, on the other hand, the free carrier density increases up to a maximum at about 10 at.% Sn, and then decreases with further increasing c following the function $N_e = N_{In} \times c (1 - c)^8$ (curve b). This implies that a portion of the tin are inactive at high doping level because the higher the tin content, the more probable the tin ions occupy the nearest-neighboring anion sites, leading to the formation of neutral defect (Sn_2O_4) as mentioned above. Therefore increasing the free carrier density via doping is self-limiting practically.

2.3.2 Free Carrier Mobility

2.3.2.1 Scattering mechanisms

For ITO films using as transparent electrodes, it is necessary to make a compromise between electrical conductivity and optical transmittance. Reduction of the resistivity involves either an increase in the carrier concentration or in the mobility. However, increasing the former also leads to an increase in the visible absorption. Hence increasing the mobility is very important for ITO films to achieving high electrical and optical properties.

The free carrier mobility μ can be defined as:

$$\mu = e\tau / m_{\text{eff}}, \quad (2.3.7)$$

where τ is the average collision time of electrons, m_{eff} is the effective electron mass in conduction band. There are many sources of electron scattering which may influence the mobility, such as ionized impurity scattering, neutral impurity scattering, grain boundary and external surface scattering, acoustical phonon scattering, defect lattice scattering, etc.

The scattering mechanisms mentioned above are expected to play different roles in ITO films. For ITO films with good crystallinity, the scattering resulting from the structural disorder can be neglected. Since no remarkable temperature dependence was observed between 100 and 500°C (Bel Hadja Tahar et al 1998), the scattering by acoustical phonons apparently is of a little importance in ITO films.

It is known that grain boundaries act as sites for impurity diffusion and these sites act as scattering centers for carriers. However, for a heavily degenerate semiconductor, the mean free path of electrons is much smaller than the crystallite size (Bel Hadj Tahar et al 1997). Therefore, grain boundary scattering is probably unimportant at high free electron densities. It is reported (Weijtes 1990) that the mobility is determined by grain boundary scattering when carrier density is below $7 \times 10^{20} \text{ cm}^{-3}$. Moreover, the mobility of the free carrier is not affected by surface scattering unless the mean free path is comparable to the film thickness. However, for polycrystalline material, the grain boundary scattering may predominate at very high carrier concentration ($>1 \times 10^{20} \text{ cm}^{-3}$) due to significant enhancement of the grain boundary potential (Kulkarni and Knickerbocker 1996).

It is well-known that the neutral scatter center density increases with increasing Sn concentration, which these defects are Sn-based as mentioned in section 2.3.1.1 (Frank and Köstlin 1982; Bel Hadj Tahar et al 1998).

2.3.2.2 Limitation of the carrier mobility

One important mechanism cannot be neglected, though, is the scattering against ionized donor impurities. According to the doping mechanism, these ions are essential in order to preserve charge neutrality in the doping films. The Coulomb interaction between these impurities and the free electrons provides a source of the scattering that is intrinsic to the doped materials. Consequently, the ionized impurity scattering sets a lower limit for the carrier mobility, regardless of the other scattering mechanisms described above, which more depends on the precise details of the preparation procedure (Bellingham, Phillips and Adkins 1992).

The contribution to the resistivity by ionized impurities was calculated on the basis of the Coulomb interaction and the following relation has been used by several authors to describe the effect of ionized scattering centers on the mobility μ_i of degenerate semiconductors (Bel Hadja Tahar et al 1998):

$$\mu_i = [24\pi^3 (\epsilon_0 \epsilon_r)^2 h^3 n] / [e^3 m^{*2} g(x) Z^2 N_i] \quad (2.3.8)$$

where n is the carrier concentration, N_i is the number density of the impurity center with charge Ze , ϵ_0 is the permittivity of free space, m^* is the effective mass of the free electrons, ϵ_r is the low-frequency relative permittivity, and $g(x)$ is the screening function. In the case of tin-doped In_2O_3 ($Z = 1$ and $N_i = n$), when the m^* and ϵ_r values were taken as $0.3 m_0$ and 9 (Frank and Köstlin 1982), respectively, a limit on the electron mobility of about $90 \text{ cm}^2/\text{Vs}$ was obtained (Bellingham, Phillips and Adkins 1992).

2.4 Optical Properties

The optical transmission and reflection spectra for a typical ITO film are shown in Figure 2-3. The optical properties of ITO in the spectral range of interest, 200 nm to 3 μm , are controlled by three types of electronic excitation: band gap transitions, interband transitions from the bulk of the valence band into the bulk of the conduction band, and intraband transitions of the free electrons in the conduction band. Consequently, there are three different regions can be distinguished for the transmission curve: In the ultraviolet region, a strong absorption edge is found. This absorption edge is called band edge which is decided by the band gap transition; In the visible region, the transmittance is very high and exhibits such extreme of minimum and maximum which are modified by interference effect; In the infrared region, the film enters a reflecting regime with metallic properties. The strong increasing of absorption and reflection region called plasma edge, which is associated with the excitation of the free electrons in the conduction band. Consequently the transmittance window is limited towards higher wavelengths by the plasma edge and towards lower wavelengths by the band edge.

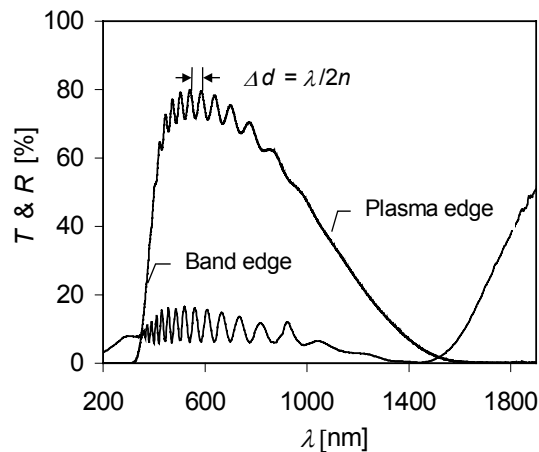


Figure 2-3 Transmittance and reflectance of the ITO film with thickness of 1.656 μm

2.4.1 Optical Constants

The optical properties of a material are described by the complex dielectric function ($\varepsilon = \varepsilon_1 + i\varepsilon_2$) or complex refractive index ($\tilde{n} = n + ik$). The relation between the dielectric function and the refractive index is given by:

$$\tilde{n} = \sqrt{\varepsilon}, \quad (2.4.1)$$

$$\varepsilon_1 = n^2 - k^2, \quad \varepsilon_2 = 2nk, \quad (2.4.2)$$

where n is usually called refractive index, and k is called extinction coefficient.

The corresponding complex dielectric index and refractive index of the ITO film shown in Figure 2-3 are displayed in Figure 2-3. Corresponding to the optical spectra, the dielectric function can also be divided into three regions. In the ultraviolet region, there is a steep increasing of the imaginary part of the dielectric function. In the visible region, the imaginary part is nearly zero. In the infrared region, ε_2 rises monotonically, whereas ε_1 goes down and crosses zero at plasma frequency, then it becomes strongly negative.

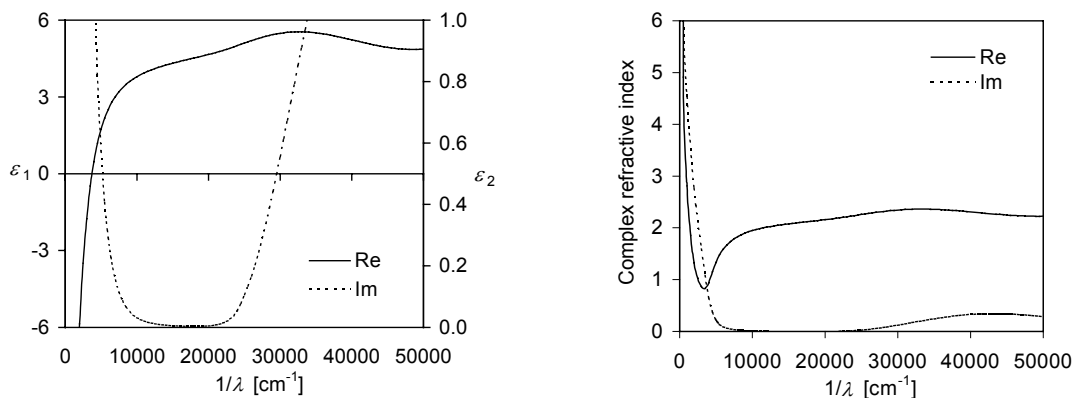


Figure 2-4 Dielectric constant (left) and complex refractive index (right) of the ITO film

2.4.2 Band Structure

In₂O₃ is a semiconducting material with a direct band gap of about 3.75 eV and an indirect band gap of about 2.6 eV (Weiher and Ley 1966).

The optoelectronic properties of materials are dominated by the electric structure near the band gap. The understanding of the band structure of ITO is based on the theory of In₂O₃. Some researchers have worked on the electric structure of In₂O₃ and ITO films (Fan and Goodenough 1977; Odaka et al 1997; Odaka et al 2001). But due to its complicated crystal structure, it has not been discovered very clearly so far.

According to the theoretical calculation on electronic structure of ITO by Odaka et al (2001), the substitution of Sn atom did not significantly destroy the shape of the density of states around the bottom of the conduction band. The only impurity band locates in the conduction band has the same s-like symmetry as that of conduction band. So the assumed parabolic shape for both valence band and conduction band around the band gap is almost retained independent of the concentration of substitutional Sn.

In literatures, several models were used to model the band gap transitions in In_2O_3 or in ITO. All of them incorporated direct allowed transitions. The minimum of the conduction band was assumed to be at $k = 0$ (Hamberg and Granqvist 1986) or $k > 0$ (Dietrich et al 1984). In order to account for the gradual onset of absorption, an Urbach tail (Hamberg and Granqvist 1986) or indirect forbidden transitions (Sczyrbowski, Dietrich and Hoffmann 1983) were assumed. In the Ref. (Weijtens and van Loon 1991), indirect transition gave a better fit to ellipsometry and reflectance data than an Urbach tail.

In direct transition model, the assumed parabolic band structure of undoped In_2O_3 is shown in Figure 2-5. For undoped In_2O_3 , the Fermi energy E_F is located in the middle of the band gap. The conduction band is empty. With the introduction of a low density of donor atoms, donor states formed just below the conduction band. And the E_F lies between the donor level and the conduction-band minimum. For increased donor density, the donor states merge with the conduction band at a certain critical density n_c , which was calculated to be $2.3 \times 10^{19} \text{ cm}^{-3}$ by Gupta, Mansingh and Srivastava (1989). When $n_e > n_c$ the material expected to exhibit free-electron properties. The intrinsic direct semiconductor band gap is 3.75 eV (Hamberg and Granqvist 1986).

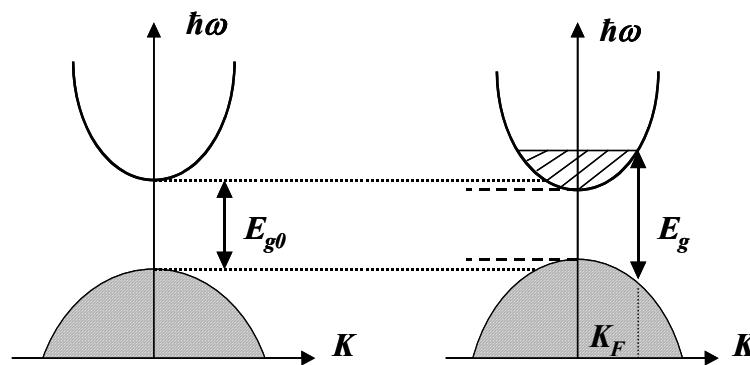


Figure 2-5 Assumed parabolic band structure of undoped In_2O_3 and the effect of Sn doping

2.4.2.1 Burstein-Moss shift

In ITO films, the fundamental absorption edge shifts towards high energy as the free carrier density increases. The widening of the band gap is known as Burstein-Moss shift (BM) (Burstein 1954; Moss 1954). For parabolic band edges the Burstein-Moss shift can be given by

$$\Delta E_g^{BM} = \left(\frac{\eta^2}{2m_{vc}^*} \right) (3\pi^2 n_e)^{2/3}, \quad (2.4.3)$$

where n_e is the density of electrons in the conduction band and m_{vc}^* is the reduced effective mass, defined by:

$$\frac{1}{m_{vc}^*} = \frac{1}{m_v^{eff}} + \frac{1}{m_c^{eff}}, \quad (2.4.4)$$

where m_v^{eff} and m_c^{eff} are the effective masses of the conduction band and valence band, respectively.

The widening of the band gap is partially compensated by many body effects such as electron-electron and electron-impurity scattering for more accurate calculation (Hamberg and Granqvist 1986).

2.5 Deposition Techniques of ITO

Nowadays, many methods can be used to deposit ITO films including thermal evaporation (Paine et al. 1999), sputtering deposition (both diode and magnetron) with dc or rf power (Hoon Yi et al 1995; Meng and Dos Santos 1996), dc support rf sputtering (Bender and Trude 1999), chemical vapor deposition (CVD) (Kane, Schweizer and Kern 1975), and spray pyrolysis (Ramaiah et al 2000). The choice of deposition techniques is determined by various factors such as quality and reproducibility of the films, the cost and complexity of the equipments, and specific disadvantage of each technique. The techniques most widely reported in the literatures and most widely used in industry are dc magnetron sputtering, dc/rf magnetron sputtering and electron beam evaporation. Of these, dc magnetron sputtering produces both high rates of deposition and good quality films (McMeeking 2000).

2.5.1 Thermal Evaporation

Solid material vaporizes when heated to sufficiently high temperature. The condensation of the vapor onto a cooler substrate yields thin solid films. Thermal evaporation may be achieved directly or indirectly (via a support) by variety of physical methods (Chopra 1969). This technique has several advantages: it is capable of yielding films which do not contain significant amount of uncontrollable contaminations; it is relatively easy to operate; it involves a minimum of critical process parameters; and it does not cause radiation damage to the substrate (Hamberg and Granqvist 1986; Yao, Hao and Wilkinson 1990).

The evaporation rate is a most important parameter for the film quality. When $\text{In}_2\text{O}_3:\text{Sn}$ is evaporated it decomposes slightly into suboxides and free oxygen. The oxygen release causes a nonstoichiometry in the films of a magnitude which

depends critically on the details of the deposition. In order to obtain reproducible results and high-quality coatings it was necessary to carefully control the amount of oxygen. For reactive deposition in the presence of oxygen, the governing parameter is then the relative impingement rate of oxygen molecules onto the surface of the growing film, which, in its turn, is determined by the evaporation rate and the oxygen pressure. Furthermore, the reactivity of the oxygen with the surface is important, which points at the fact that substrate temperature is another crucial parameter. The temperature also affects the crystallinity of the film.

2.5.2 Spray Hydrolysis (Pyrolysis)

The spray hydrolysis method has been used for the preparation of TCO films for many years because it is relatively simple and cheap. The conventional spray hydrolysis technique consists of spraying a dilute solution of appropriate chloride from an atomizer onto a heated substrate under normal atmosphere conditions or controlled atmosphere. High pressure argon, nitrogen, or air is usually used as spraying gas (Jarzębski 1982). A schematic diagram of such apparatus is shown in Figure 2-6.

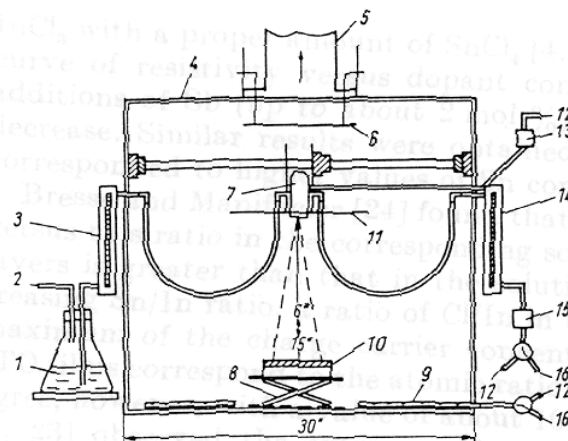


Figure 2-6 Schematic diagram of the spray hydrolysis apparatus; 1 spray solution; 2 vent; 3 solution flow meter; 4 acrylic chamber; 5 exhaust; 6 exhaust damper; 7 atomizer; 8 lab-jack; 9 perforated tube; 10 substrate heater; 11 shield; 12 air inlet; 13 solenoid valve (pulsed); 14 gas flow meter; 15 solenoid valve; 16 nitrogen inlet (Jarzębski 1982)

The ITO films deposited under normal atmospheric conditions contained an uncontrollable amount of oxygen which acted as an electron trap. To eliminate this excess oxygen, the films had to be subjected to heat treatment in vacuum or in reducing atmosphere at about 720 K (Köstlin, Jost and Lems 1975).

2.5.3 Chemical Vapor Deposition

Chemical vapor deposition (CVD) is a process in which a chemical reaction involving gaseous reacting species takes place on, or in the vicinity of, a heated substrate surface. The principle of CVD device is illustrated in Figure 2-7. The main controlling parameters are the substrate temperature, substrate material, composition of the reaction gas mixture, gas flow, total pressure, and the geometry of the deposition system. The gas flow and the apparatus geometry determine the uniformity of the deposited films over large areas. The substrate temperature and the gas flow control the deposition rate (Bel Hadja Tahar et al 1998).

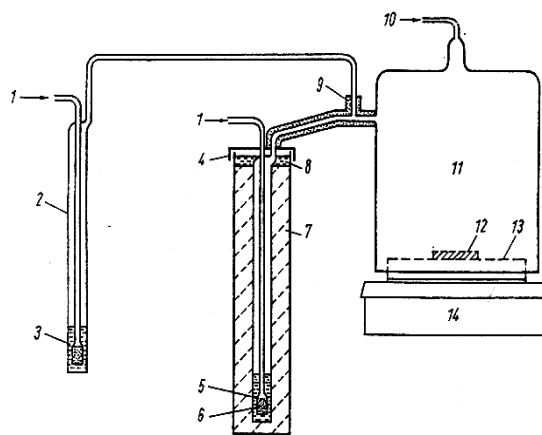


Figure 2-7 CVD system for preparation of ITO films; 1 nitrogen inlet; 2 glass bubbler; 3 antimony source; 4 plastic or metal cover; 5 tin source; 6 glass frit; 7 hot water bath; 8 oil; 9 heating tape; 10 oxygen inlet; 11 glass or metal reactor; 12 substrate; 13 rotating plate; 14 rotating reactor (Jarzębski 1982)

Films with high demands for purity, stoichiometry, and structural perfection could be obtained by CVD method (Jarzębski 1982). This technique has also the advantage of being cost effective with respect to the apparatus. It enables the production of coatings with good properties even on substrates of complicated shapes without the use of high vacuum. In particular, atmospheric pressure CVD (APCVD) is attractive in many applications in the sense that it offers high deposition rate and hence short process time. However, since CVD processes are based on interfacial chemistry, they are sensitive to contamination. The major limitations of the process are the small areas of uniform coatings and the cost of the starting reagents as in the case of indium compounds. The deposition of ITO films by the CVD method generally faces difficulties due to a lack of volatile and thermally stable source materials.

2.5.4 Sputtering

The sputtering phenomenon has been known since 1852 and exploited for deposition of films. The sputtering method is one of the most extensively used techniques for the deposition of ITO films. The sputtered ITO films have been deposited by either dc or rf power using either oxide ($\text{In}_2\text{O}_3\text{-SnO}_2$) or metallic alloy (In-Sn) target in argon-oxygen (Ar-O_2) mixture. Sputter deposition methods used today have common simple goals: to generate and maintain a desired plasma and to establish a bias or electric field for the acceleration of ions to the electrode or target being bombarded (McClanahan and Laegreid 1991).

2.5.4.1 Basic sputtering mechanisms

As shown in Figure 2-8, when an ion approaches the surface of a solid (target) one or all of the following phenomena may occur (Chapman 1980).

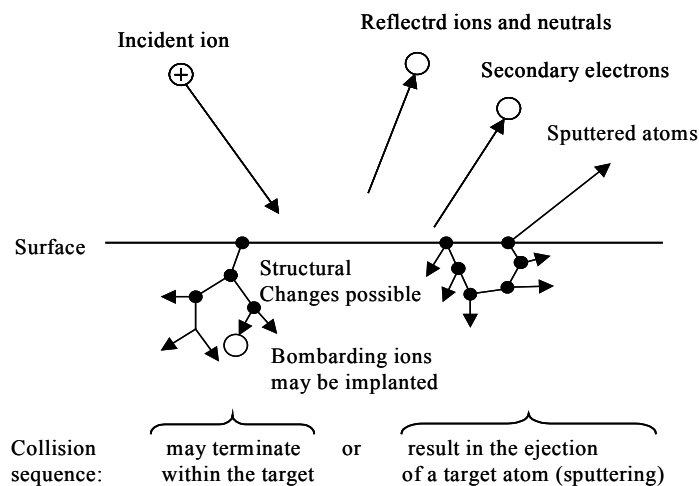


Figure 2-8 Interactions of ions with surfaces (Chapman 1980)

- The ion may be reflected, probably being neutralized in the process.
- The impact of the ion may cause the target to eject an electron, usually referred to as a secondary electron.
- The ion may become buried in the target. This is the phenomenon of *ion implantation*.
- The ion impact may also be responsible for some structural rearrangements in the target material.
- The ion impact may set up a series of collisions between atoms of the target, possibly leading to the ejection of one of these atoms. This ejection process is known as *sputtering*.

When an ion with energy of more than about 30 eV hits a surface, a small fraction of the energy and momentum of the incoming ion will, through lattice collisions, be reversed and may cause ejection of surface atoms, i.e. sputtering (Behrisch and Wittmaack 1991). The sputtered atoms leave the target surface with relatively high energies (~ 10 eV) compared with evaporation atoms (~ 0.1 eV). The average number of the atoms ejected from the surface per incident ion is called the *sputtering yield* (Behrisch 1983). The ion source is usually a plasma (i.e., an electrically neutral mixture of positive ions and electrons) generated by electron impact in a noble gas at subatmospheric pressures (typically 2 - 10 Pa). The ions are accelerated in an electric field obtained by applying a negative potential with respect to the plasma potential to an electrode immersed in that plasma. The ejected or sputtered atoms can be condensed on a substrate to form a thin film.

The sputtering yield S depends on many factors, such as the mass and the energy of the incident particles; the mass and the binding energy of the sputtered atoms; the crystallinity of the target; etc. And it can be described as (Ellmer 2000; Ohring 1992):

$$S = \text{const} (E_{ion} - E_{thres}) = \text{const} e(V_p - V_{dc} - V_{thres}), \quad (2.5.1)$$

$$E_{thres} = 8U_s(M_1/M_2)^{2/5}, \quad (2.5.2)$$

where E_{ion} is the energy of the incident ion, E_{thres} is a threshold energy, V_p is the plasma potential, V_{dc} is the dc voltage on the target (discharge voltage), U_s is the surface potential barrier and M_1 and M_2 are the mass number of the ion and the target, respectively.

The deposition rate R is proportional to the sputtering yield S , and $I(1 - \gamma)$, with I the discharge current and γ the secondary electron emission coefficient (Ellmer 2000):

$$R = \text{const} SI(1-\gamma) \quad (2.5.3)$$

2.5.4.2 Direct current (dc) sputtering

Due to a high sputtering rate and good film performances, dc-magnetron sputtering is used widely.

The arrangement for our dc sputtering system is shown in Figure 2-9. The material to be sputtered is used as a cathode (target) of an electrical circuit, and a high negative voltage $V(\text{dc})$ is applied to it. The substrate on which the film is to be deposited is placed on an electrically floating substrate holder (anode) 5 cm away. An inert gas (e.g., Argon) is introduced into the chamber to some specified pressure ($\sim 10^{-3}$ mbar). The action of the electric field is to accelerate electrons

which in turn collide with argon atoms, breaking some of them up into argon ions and more electrons to produce the glow discharge. The charged particles thus produced are accelerated by the field, the electrons tending towards the anode and the ions towards the cathode, so that a current I flows.

When the ions strike the cathode, they may sputter some of the target atoms off. They may also liberate secondary electrons from the target and it is these secondary electrons that are responsible for maintaining the electron supply and sustaining the glow discharge.

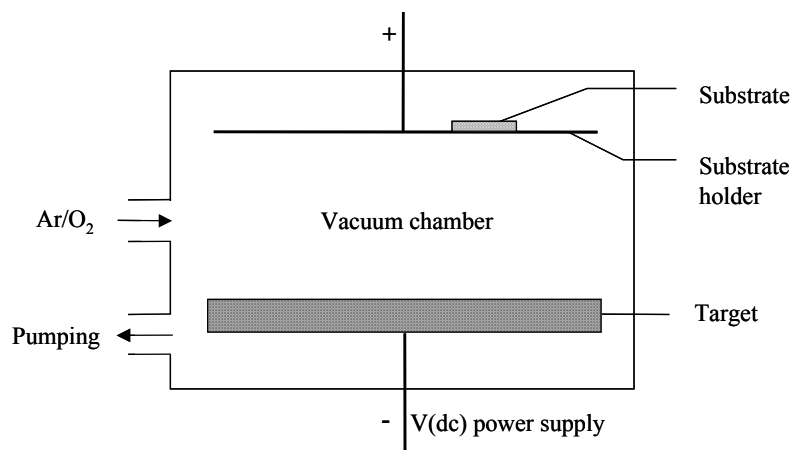


Figure 2-9 Schematic diagram of a dc sputtering system

The distribution of the potential between the cathode (target) and the floating anode is illustrated in Figure 2-10.

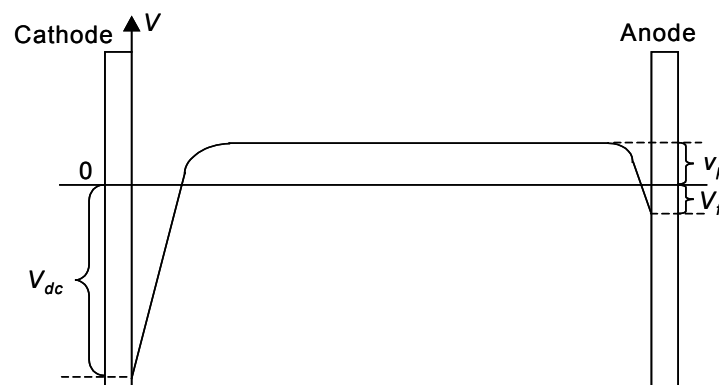


Figure 2-10 Voltage distribution in a dc glow discharge process

Energetic ion bombardment of the growth surface with both sputtered atoms (In and O) and gas species (Ar and O) is a characteristic of sputter deposition process (Shigesato and Paine 1994). The particles that form the film are with energies of several electron volts, the neutral Ar atoms reflected from the target and O⁻ ions accelerated from the target to the substrate with energies up to the cathode potential. The investigation has revealed that lower energy ion bombardment could

improve the performance of sputter-deposited ITO films (Shigesato, Takaki and Haranoh 1992) and it was speculated that the grain-subgrain microstructure of the sputtered films is a result of the bombardment of the growth surface by energetic (~20 eV) ions during deposition (Shigesato and Paine 1994). However, higher energetic bombardment will result in the damage of the film structure. The correlations between the energy of the impinge particles and the processes take place on the surface and the inside of the growing film are listed following:

- <1eV: surface diffusion of adatom
- 10eV: excitation of surface layer (higher surface mobility)
- 50eV: destruction of surface layer (amorphous of the growing film)
- 100eV: arriving atom is deposited below the surface (implantation) (crystalline films)

2.5.4.3 Radio frequency (rf) sputtering

DC method cannot be used to sputter nonconducting targets because of charge accumulation on the target surface. This difficult can be overcome by using radio frequency (rf) sputtering. A single rf sputtering apparatus can be used to deposit conducting, semiconducting, and insulating coatings. RF reactive sputtering offers a number of advantages compared with other techniques such as CVD and PVD: it is possible to predict the layer structure and thickness; compound materials may be sputtered roughly without losing the target stoichiometry; good adherence and high film density can be achieved because of the high kinetic energy of the incident target atoms; and uniform layer thickness are obtained (Carl, Schmitt and Friedrich 1997).

The technique of rf sputtering uses an alternating voltage power supply at rf frequencies (13.56 MHz), so that the sputtering target is alternately bombarded by ions and then electrons so as to avoid charge build-up. Hence, the insulators can be deposited by rf sputtering. In the case of rf sputtering, the plasma is mainly driven by ionization due to electrons which perform an oscillating motion in the plasma body. The electrons are able to follow the rf frequency of 13.56 MHz while the ions are not, due to their large inertia. This kind of excitation is much more effective compared to the ionization by non-oscillating secondary electrons (in the case of dc-sputtering) and leads to lower target voltages in an rf discharge (Ellmer 2000) and the operating pressure could also be practically extended down to 1 mtorr (Chapman 1980).

2.5.4.4 Magnetron sputtering

The magnetron target is based on the work carried out by Penning more than 60 years ago. Since then a lot of work had been done to develop this concept. However, the planar magnetron, which is the most widely used target assembly today, was not introduced until the early 1970s by Chapin (Klabunde 1985).

Sputter deposition of thin films for optical and electrical applications has increased markedly in the past few years. This has been mainly a result of the development of high-performance magnetron cathodes. In comparison to conventional diode sputtering, the magnetron cathode provides higher deposition rates at lower operating pressure and the ability to deposit high-quality films, which with greater adherence and greater uniformity over large areas, at low substrate temperature (Klabunde 1985).

The planar target in its simplest form is shown schematically in Figure 2-11 (b). As comparing the dc diode sputtering process is showed in Figure 2-11 (a). It consists of the target material backed by permanent magnets that provide a toroidal confinement field with the field lines forming a closed tunnel on the target surface. The field strength is chosen to provide effective confinement for electrons while allowing heavier ions considerable freedom.

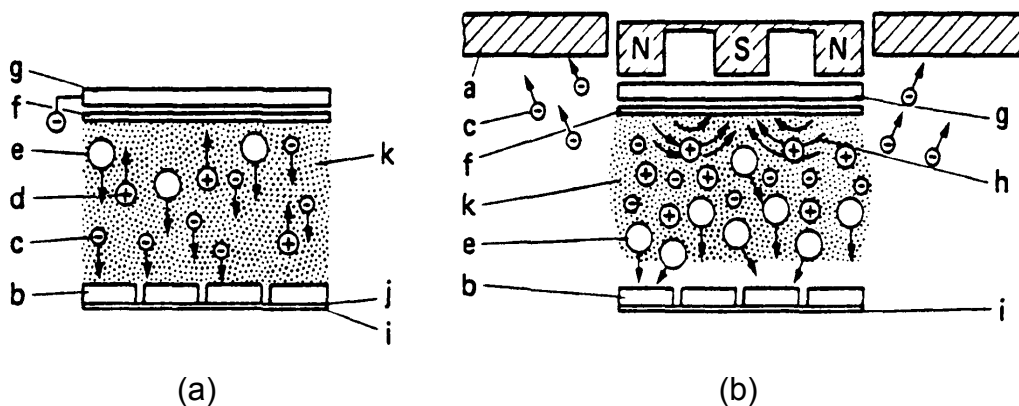


Figure 2-11 Schematic illustrations of the (a) convention dc-diode and (b) planar magnetron cathode sputtering (a. the wall of vacuum chamber, b. substrate, c. secondary electron, d. ion, e. metallic atom, f. target, g. cathode, h. magnet field line, i. substrate holder, j. anode, k. plasma) (Hartmut 1987)

Secondary electrons emitted from the target during the sputtering process are accelerated across the cathode dark space towards the highly charged plasma sheath. This path is modified by the $\mathbf{E} \times \mathbf{B}$ Lorentz force. One component of their motion is a helical path about the magnetic field lines. The electrons traveling

along these helical lines toward the center of the target are reflected due to the higher density of field lines in this region and the repulsive electric field encountered. After reflection the electrons eventually reach the perimeter of the target where the field lines again intersect the surface. An anode placed in this region effectively collects these electrons and prevents from reaching the substrate. A second component of their motion is a drift from one field line to another resulting in a race track effect about the toroidal tunnel on the target surface. The combined motion gives an extended path length resulting in a large number of collisions of the electrons with gas atoms. The ions, of course, experience the same Lorentz force as the electrons; however, due to the much higher mass, their motion is not as restricted (Klabunde 1985).

2.5.4.5 Reactive sputtering

The notation “reactive sputtering” refers to the case where neutral, excited, or ionized gaseous species react with the target, sputtered particles, or substrate (Behrisch and Wittmaack 1991). Instead of rf sputtering, nonconducting compounds thin films, such as oxides, nitrides, and sulfides can also be deposited by reactive sputtering in a chamber atmosphere consisting of reactive gas (O_2 , N_2 , or H_2S) mixed with inert gas. The target material may be the desired film compound or the metal of which the desired compound is to be formed.

It has been supposed (Holland 1956) that the active gas could combine with the metal in three ways to form a sputtered gas-metal film as shown in Figure 2-12.

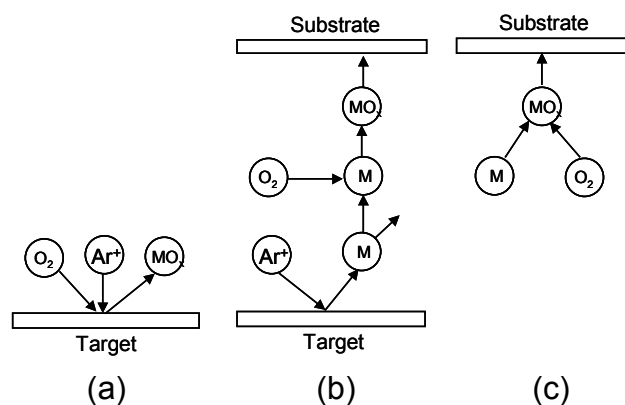


Figure 2-12 Three different mechanisms for reactive sputter deposition (Holland 1956): (a) at the target, (b) in the plasma volume, (c) at the substrate

2.6 Effects of Deposition Parameters on the Properties of ITO Films for Sputter Techniques

The properties of ITO films prepared by sputtering methods are quite sensitive to the deposition conditions, such as the oxygen partial pressure p_{O_2} , the substrate temperature T_s , sputtering gas and total pressure, sputtering power, the distance between target and substrate, etc.

2.6.1 Substrate Temperature

In the case of e-beam (EB) evaporation, polycrystalline ITO films can be deposited only if the substrate temperature (T_s) is above the crystallization temperature (around 150 - 160°C) (Song et al 1999), whereas, polycrystalline ITO films have reportedly been deposited even at T_s of room temperature (RT) by dc magnetron sputtering when the total gas pressure was rather low during the deposition (the energy of sputtered particles arriving at the substrate is higher as comment later) (Meng and Dos Santos 1998). It was also observed that the microstructure of ITO films deposited at T_s of RT comprised of two layers, i.e., a polycrystalline top layer and an amorphous bottom layer (El Akkad et al 2000).

It is clearly that the mobility of adatoms and clusters, which is in proportion to their energy, on the substrate will be increased with increasing the substrate temperature. Hence, the substrate temperature influences the microstructure and the orientation of ITO films. It has been observed by many authors (Meng and Dos Santos 1998; Vink et al 1995; Uthanna et al 1996) that the predominant orientation changed from (222) to (400) with increasing substrate temperature. The reason was attributed to the enhanced of the mobility of the adatoms on the substrate surface may favor the growth of the films along some simple crystal planes, such as $\langle 100 \rangle$ and $\langle 001 \rangle$.

Meng and Dos Santos (1998) have also observed that the lattice distortion decreases with increasing T_s , and the films are dense and the grain size along sample surface increases as the substrate temperature is increased. They reported as well as that the high substrate temperature may result in more tin atoms diffusing from grain boundaries and interstitial lattice locations to regular In_2O_3 lattice location, leading to higher electron concentration. El Akkad et al (2000) have also observed both grain size and carrier density increase with T_s increasing. However, they found that the lattice distortion is also increases with increasing T_s , which is contrary to the result of Meng and Dos Santos (1998). They

inferred that it might be due to the substitutional of Sn instead of oxygen incorporation model.

The substrate temperature will also play a role in the deposition rate in the case of alloy target. Meng and Dos Santos (1998) reported that the deposition rate begins to increase with the T_s when the temperature is higher than 200°C. Heating of the substrate results in the heating of the gas discharge and the target surface. As indium has a very low melting point (about 157°C), a small increase of the temperature of the target surface will result in a significant increase on the active energy of the indium atoms of the target surface and then an increase of the sputtering yield. This is only occurring for the alloy target.

2.6.2 Oxygen Partial Pressure

The oxygen partial pressure q_{O_2} is defined as the ratio of oxygen flow flux to the inert gas flux. It is necessary and important to add the oxygen for obtaining films prepared from metallic targets (Shigesato, Takaki and Haranoh 1992). A higher O_2 concentration tended to yield transparent films but of high sheet resistance. A lower O_2 concentration, on the contrary, gave films with a low sheet resistance and a slightly metallic appearance. The film is considered to be more oxygen deficient or metallic (Karasawa and Miyata 1993).

In the fabrication of ITO films with oxide target, the oxygen partial pressure is also very important for determining the electrical and optical properties of ITO films. It has been observed by many authors (Joshi, Singh and McClure 1995; Bender et al 1998; Carl, Schmitt and Friedrich 1997) that there exists a minimum of the electrical resistivity of ITO films as the q_{O_2} increases. This is due to the influence of oxygen partial pressure on electrical resistivity. This can be explained in terms of two competing effects: increase in q_{O_2} enhances the growth of crystalline phase of ITO films which leads to higher mobility of carriers; on the other hand, increased q_{O_2} decreases the carrier density (Latz, Michael and Scherner 1991; Joshi, Singh and McClure 1995). The carrier density decreases as the oxygen partial pressure increases, because the oxygen vacancy concentration decreased as the q_{O_2} increased (Choi et al 1995). An oxygen vacancy can donate two free electrons for conduction, but highly oxygen deficient films show reduced optical transmittance, lower optical band gap, poor Sn doping efficiency and a worsening of carrier mobility due to a more effective ionized impurity scattering phenomenon (Terzini, Thilakan and Minarini 2000). Hence, it has been observed that the transmission of the films is improved as q_{O_2} is increased (Joshi, Singh and McClure 1995).

Honda, Watamori and Oura (1996) have investigated the oxygen content of ITO films by means of $^{16}\text{O}(\alpha,\alpha)^{16}\text{O}$ resonant backscattering of a high-energy ion beam. The content of oxygen in the films changes with q_{O_2} . They concluded the improvement of the crystallinity of the ITO films with increasing oxygen content, since the intensity of the (222) peak, reflecting the In_2O_3 bixbyte structure, increased with increasing oxygen content. Furthermore, Kikuchi et al (2001) asserted that the crystallinity of the ITO films decreases with excess oxygen in the discharge gas (>25%).

The observation points out that the crystal growth of ITO is oxygen concentration dependent. If the film contains sufficient oxygen to maintain the stoichiometric ratio of In_2O_3 , the crystal growth is preferentially with (222) plane. Otherwise, far from the stoichiometric composition, the crystal growth is much faster, a polycrystalline structure is achieved even at RT and the film is always $\langle 100 \rangle$ oriented (Terzini, Thilakan and Minarini 2000). The lattice constant of as-deposited ITO films increases with increasing q_{O_2} (Kikuchi et al 2001).

2.6.3 Target-Substrate Distance

In sputtering techniques, the ejected target atom or molecule undergoes collisions with the ambient gas atoms and loses a part of its energy during its transit to the substrate (Vasant Kumar and Mansingh 1989). As the energy of the sputtered atoms or molecules is reduced to the thermal energy of the gas kT at a distance h from the target after a finite number of collisions, the sputtered atoms or molecules are said to be thermalized (Wu and Chiou 1994). The number of collisions n required to thermalize a sputtered atom, which is determined by its initial energy, relates with the thermalization distance h by:

$$h = n\lambda, \quad (2.6.1)$$

where λ is the mean free path, given by an empirical formula $\lambda p = 6.3 \times 10^{-3}$ mbar·cm (Megel et al 2000), p is the pressure. Therefore the thermalization distance h depends on the sputter power and sputter pressure. Nyaiesh (1986) suggested that a virtual source of the sputtered atoms is expected to form at this distance h . The virtual source separates the gap between the target and the substrate into two regions: thermalization region (from the target to the virtual source) and diffusion region (from the virtual source to the substrate), as shown in Figure 2-13.

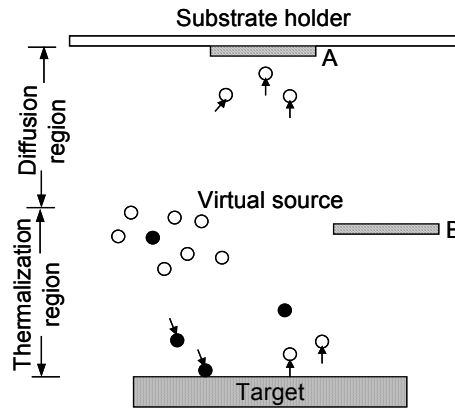


Figure 2-13 *Relative configuration of target, substrate, and virtual source. A and B represent different substrate position. ○ sputtered particles; • gas atoms (not to scale) (Wu and Chiou 1994)*

It was found that the virtual source was about 50 mm away from the target at an rf power of 50 W and argon pressure of 10 mTorr (Wu and Chiou 1994). This model can be used to explain the effect of the target-substrate distance on the deposition rate. The kinetic energy of the sputtered particles in thermalization region is large, and the deposition rate does not vary much with the T - S distance when the substrate is in this region (e.g. substrate B). However, the deposition rate decreases with increasing T - S distance when the substrate is in the diffusion region, because the transport of the sputtered particles from the virtual source to the substrate is by diffusion due to the material concentration gradient (Wu and Chiou 1994). Meng and Dos Santos (2000) also attributed the decrease of the deposition rate with increasing T - S distance to the angular emission from the target. The angular emission results in a cosine-like angular distribution from the target, so as the substrate moves further away from the target, some of the atoms hit the chamber walls before they can reach the substrate and also result in a decrease of the deposition rate.

Since the kinetic energy of the sputtered particles in the thermalization and the diffusion region are quite different, it is expected that the microstructure and the properties of ITO films deposited in these two different regions will be different. It was reported (Meng and Dos Santos 2000) that at very small T - S distance, the film showed a random orientation and very weak peak intensity, which indicated that the degree of crystallinity of the films decreased as the target-substrate distance decreased. In addition, the intensity ratio of $I(222)/I(440)$ and the free carrier mobility decreased with increasing T - S distance, whereas the electrical resistivity increased with increasing T - S distance.

The total pressure P_{tot} and the sputtering power can also strongly influence the deposition rate and the properties of ITO films, actually, via shifting the position of the virtual source. It was reported (Vasant Kumar and Mansingh 1989) that the virtual source was shifting away from the target with increasing rf power and decreasing the sputtering pressure. The increase of rf power caused an increase in the density of sputtered neutrals and their average initial energy, thus enhanced the number of collisions n and leading to a higher h . The moving of the virtual source with the sputtering pressure was attributed to the changing of the mean free path.

2.6.4 Total Pressure

Generally, for dc sputtering, the operating pressure limitations are imposed by the requirements of both the glow discharge and of the film deposition. The glow discharge sets a lower pressure limit on account of sustaining the discharge plasma. Below 30 mtorr, the current (and hence ion flux at the target) and sputtering rate in a dc discharge become quite small. On the other hand, the collision of the sputtered particles with the gas atoms on its way to the substrate, which will increase with increasing pressure, sets an upper limit of total pressure. The result of the collision is to decrease the deposition rate. The scattering process becomes serious above about 100 mtorr, so that taking both limitations into account; an overall operating range of about 30 - 120 mtorr is usual for dc sputter deposition (Chapman 1980).

When the other parameters of a deposition process are fixed the kinetic energy of Ar atoms reflected from the cathode and sputtered target atoms (In and Sn) are determined by the total sputtering pressure, causing by the collisions with the ambient gas molecules.

It has been revealed (Song et al 1999) that the crystallinity and the electrical properties of ITO films deposited at low T_s are clearly correlated with the total pressure P_{tot} in term of the kinetic energy of high-energy particles and sputtered In (or Sn) particles arriving at the substrate surface.

Generally, sputtered particles have kinetic energy of several eV (about 1 - 3 eV) which is up to one order of magnitude greater than that of the evaporated particles. These kinetic energies will enhance the surface mobility of the sputtered atoms reaching the substrate surface, and the crystallinity of the films is significantly affected by them. Therefore, polycrystalline ITO films have reportedly been deposited even at T_s of RT by dc sputter deposition (Song et al 1998). On the contrary, as the total pressure increases the kinetic energy of sputtered atoms

decreases as a result of the collision scattering. When the sputtered particles are not energetic enough for the enhancement of the surface migration, an amorphous structure of ITO films was deposited (Song et al 1999).

On the other hand, the bombardment particles such as Ar and O^- negative ions will also affect the growth of ITO films. These particles are generally considered to be high-energy particles. It is reported (Kubota et al 1994; Shigesato and Paine 1994) that the crystallinity of ITO films was improved by Ar ion bombardment with the bombardment energy of around 40 eV, whereas bombardment energy higher than 50 eV resulted in film damage. Therefore, a very low P_{tot} will contribute to a degradation in crystallinity of the films due to the damage caused by the bombardment of high-energy particles.

The dependence of crystallinity on P_{tot} was correlated with the transport processes of particles between the target and the substrate. These results were considered from the viewpoint of the kinetic energy of particles (sputtered In atoms and high-energy reflected Ar) arriving at the substrate surface.

Meng and Dos Santos (2000) have also reported the effects of the total pressure. In their experiment, ITO films were prepared by rf magnetron sputtering. The P_{tot} was varied from 8×10^{-4} to 7.6×10^{-3} mbar. They have observed that as the sputtering pressure was increased, the orientation changed from (222) to (440). And as the pressure was decreased, the films became denser. The electron scattering in the films prepared at high pressure was higher than at low pressure.

2.6.5 Sputtering Power

The influence of the sputtering power on ITO films is also involving the effect of kinetic energy of sputtered atoms and high energetic bombardment particles as mentioned above. The structure of ITO samples could be changed from amorphous to polycrystalline films as the sputtering power enhanced from 0.27 to 0.8 W/cm² (Terzini et al 1999).

It was also observed (Terzini, Thilakan and Minarini 2000) that the carrier density in ITO films increased with increasing rf power. This was attributed to the plasma density changing with the sputtering power, leading to the formation of more oxygen vacancies.

It is already clear from previous introduction that the change in the plasma density will influence the thermalization distance of the sputtered particles and consequently modify the films properties and the films stoichiometry (Terzini et al 1999). In fact, when the plasma thermalization distance is larger than the target-

substrate gap (high power regime), a removal of oxygen from the growing surface by energetic impingement of O^- ions could take place (Panicke and Essinger 1981). In the films deposited in this regime are $\langle 100 \rangle$ oriented. On the other hand, when the film grows close or far away from the thermalization distance (Vasanth Kumar and Mansingh 1989) the film stoichiometry is recovered and the crystalline structure results $\langle 111 \rangle$ oriented (Korobov, Leibovitch and Shapira 1993). Moreover, according to the study of Panicker and Essinger (1981), the mechanism of oxygen formation is ascribed to the recombination of negative charged O^- ions at the growing ITO surface to form volatile O_2 . This mechanism is even more enhanced at higher power because of the larger number of oxygen ions that can reach the substrate surface.

2.6.6 Post-Annealing

The post-deposition annealing is a common practice in many of the device fabrication processes and significant for the stability and reproducibility of the entire process (Karasawa and Miyata 1993). There are three possible effects of postannealing: (1) improvement of crystallinity, (2) formation of oxygen vacancies, and (3) release of excess oxygen (Kikuchi et al 2001). However, according to Omata et al (1998), released oxygen originating from the lattice oxygen, which leads to the oxygen vacancies, took place at >973 K. Therefore, in most cases, the effect (1) and (3) are more functional in improving the quality of ITO films when the annealing temperature is not so high. The effectiveness of postannealing, however, depends on the properties of the as-deposited ITO (Karasawa and Miyata 1993).

Annealing the ITO films in air at a temperature higher than the deposition temperature provides oxygen to the ITO if it is excessively oxygen deficient and reduces it if it is relatively oxygen rich. Heat treatment therefore can optimize the film properties if it is deposited with near-optimum condition. Annealing may also enhance grain growth and recovery of disordered structure. A large grain size increases the carrier mobility which will lower the resistivity and reduce the light loss by scattering (Karasawa and Miyata 1993).

Kikuchi et al (2001) carried out a postannealing process for ITO films at 437K. It was found that the carrier density and mobility increased by postannealing and the increase was almost complete after 30 min. It indicated that oxygen loosely bound to Sn ions and behaved as a neutral impurity defects ($Sn_{In} \bullet O_i$) was released completely. It was also supposed that these excess oxygens mainly exist in the grain boundary, because the lattice constant did not change after postannealing.

Additionally, the transmission of ITO films was also improved with increasing annealing temperature (Joshi, Singh and McClure 1995).

2.6.7 Structure Zone Models

It probably involves four basic processes as incident atoms deposit onto the growing film (substrate): shadowing, surface diffusion, bulk diffusion, and desorption (Ohring 1992). The dominance of one or more of these four processes as a function of T/T_m (T is the substrate temperature and T_m is the melting point of the coating material in absolute degree) is manifested by different structural morphologies. This is the basis of the zone structure models to characterize film structure. The microstructure and morphology of thick evaporated coating have been extensively studied by Movchan and Demchishin (1969). They concluded that the coatings could be represented as a function of T/T_m in terms of three zones, each with its own characteristic structure and physical properties. Thornton (1974) extended this model to sputtering by adding an additional axis to account for the effect of the sputtering gas. In addition a transition zone (Zone T) was identified between Zone 1 and Zone 2 (see Figure 2-14).

The microstructure of each zone was characterized by Thornton (1982) as following:

- The Zone 1 structure results when adatom diffusion is insufficient to overcome the effect of shadowing. It therefore forms at low T/T_m (<0.3) and is promoted by an elevated working gas pressure. It usually consists of tapered crystal with domed tops which are separated by voided boundaries. The crystal diameter increases with T/T_m .
- The Zone T structure consists of a dense array of poorly defined fibrous grains without grossly voided boundaries.
- The Zone 2 region is defined as that range of T/T_m ($0.3 < T/T_m < 0.5$) where the growth process is dominated by adatom surface diffusion. The structure consists of columnar grains separated by distinct dense intercrystalline boundaries.
- The Zone 3 region is defined as that range of T/T_m (>0.5) where bulk diffusion has a dominant influence on the final structure of the coating.

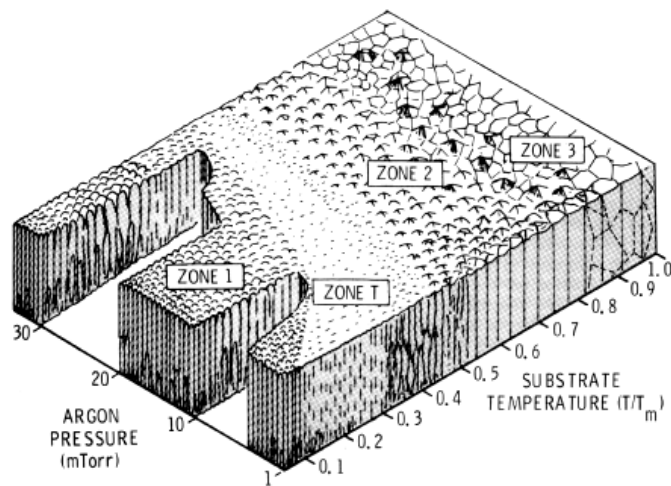


Figure 2-14 Schematic representation of the influence of substrate temperature and argon working pressure on the structure of metal coatings deposited by sputtering (Bunshah et al 1982)

3 Preparation of ITO Thin Films

In this work, the ITO films were deposited by dc and rf magnetron sputtering methods.

3.1 Deposition Equipment

The ITO films were deposited with the von Ardenne Laboratory System LA 500S. The schematic diagram of the construction of this sputtering system is displayed in Figure 3-1. The deposition equipment is composed of a stainless steel cylindrical chamber, high vacuum system, dc and rf sputtering system, power supply, switch cabinet, etc. The equipment is supplied by cooling water. A friendly computer interface (see Figure 3-2) insures the deposition procedures easily to be executed. The command and data fluxes for sputtering are coped with a RS232 processor. Following, the main parts of the deposition system are described more detailed.

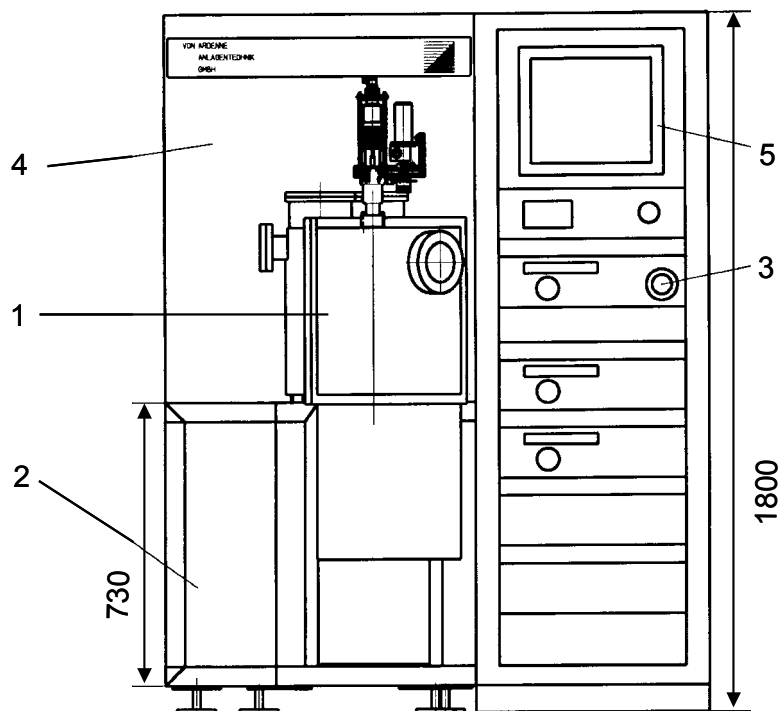


Figure 3-1 Schematic diagram of the construction of the LA 500S system (1 sputter chamber, 2 framework, 3 emergency break, 4 electronic switch cabinet, 5 rack cabinet)

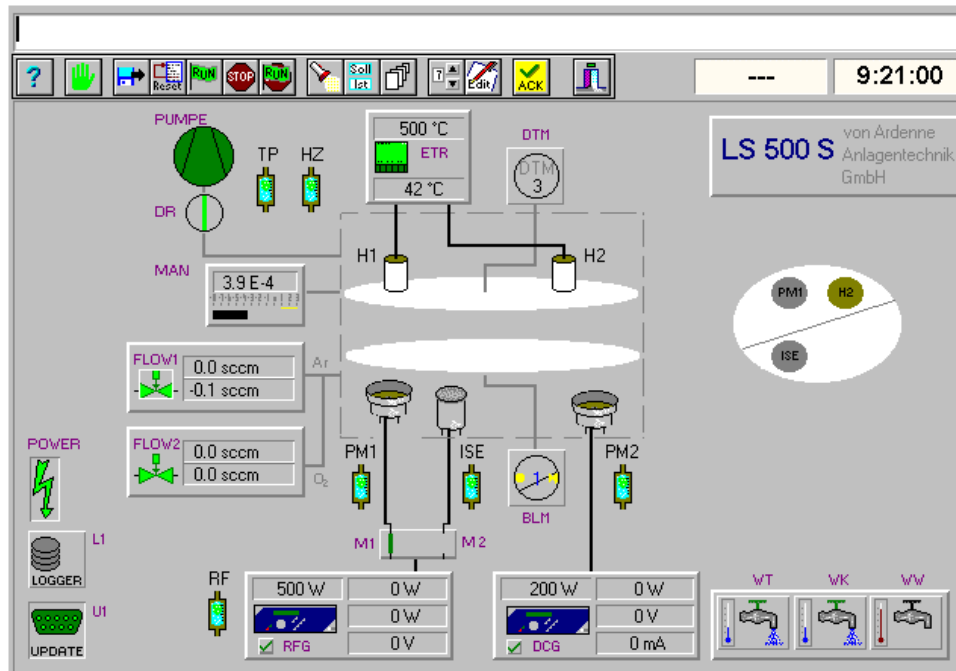


Figure 3-2 Interface of the control software WICON of the system

3.1.1 Process Chamber

Figure 3-4 shows the schematic layout of the sputtering chamber and the associated dc and rf power supply of the LA 500S system. The process chamber is a stainless steel cylinder supplied by cooling water. It is vertical mounted inside, where the sputter-up-mode is available. It consists of three sputter sources, i.e. dc sputtering source, rf sputtering source and inversed sputter etcher, blinds and substrate holder which can rotate around the central axel, and two carbon radiators above the substrate holder.

3.1.2 Vacuum System

A carbon-hydrogen free vacuum is generated by a high vacuum pump system, which is composed of a choke (for reducing the volume flow rate during sputtering), a turbomolecular pump, a membran pump and a full-range compact pressure sensor. A connection with diameter of DN 160 to the high vacuum pump system is found in the rear of the chamber.

3.1.3 DC-Sputtering System

For dc sputtering the ITO target is supplied power by a dc generator (DCG) via a high frequency filter (RFF) and a matchbox (MB3). The output of the dc generator is up to 1.5 kW. The configuration of the ITO sputter source (PPS 90) is displayed

in Figure 3-3. As it is shown the planar round magnetron sputter source consists of source base body, dark field shield, plasma shield and target. The target is an $\text{In}_2\text{O}_3/\text{SnO}_2$ (10 wt%) ceramic with a diameter of 90 mm. It can be sputtered under dc and rf modes. The distance between the target and the substrate is 50 mm.

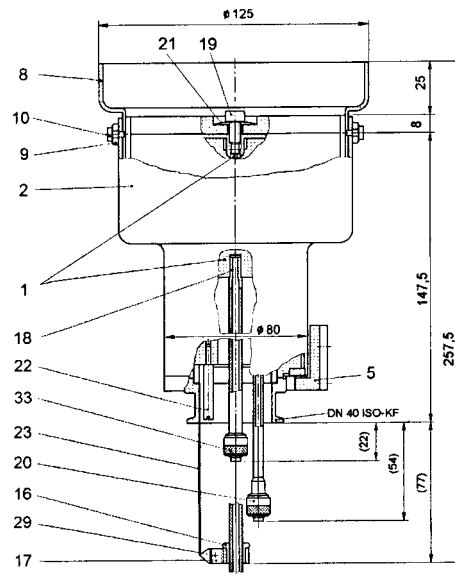


Figure 3-3 The constructure of ITO target (PPS 90) (1 cathode body, 2 dark field shield, 5 bracket, 8 plasma shield, 9 hoop guide, 10 shoulder screw, 16 clamp ring, 17 bracket, 18 connector, 20 cooling water tube connector, 22 bolt, 23 mounting link, 29 bolt, 33 cooling water tube cathode body)

3.1.4 RF-Sputtering System

The electrical system of rf sputtering for ITO deposition involves a rf generator operated at 13.56 MHz, a rf switching control (SWC2), a rf selector switch (SW2) and two matchboxes (MB3, MB4) as shown in Figure 3-4. The output of the rf generator is up to 600 W. Since a plasma process is a variable complex load, whereas the rf generator is designed for 50 Ω loads, a matchbox directly connected to the application is used to transform the complex load of the plasma process to a stable 50 Ω resistive load. The rf selector switch contains one rf input and, depending on the model, two to four rf outputs. It is connected between the rf generator and the matching network. The rf selector switch switches the rf power between the various rf loads. As the result, only one rf load can be supplied with rf power at any one time. A rf switching control PFS 100A is available as an accessory for the rf selector switches. Up to three rf selector switches can be

connected to the rf generator cascaded via the switch control in the fibre optic cable ring.

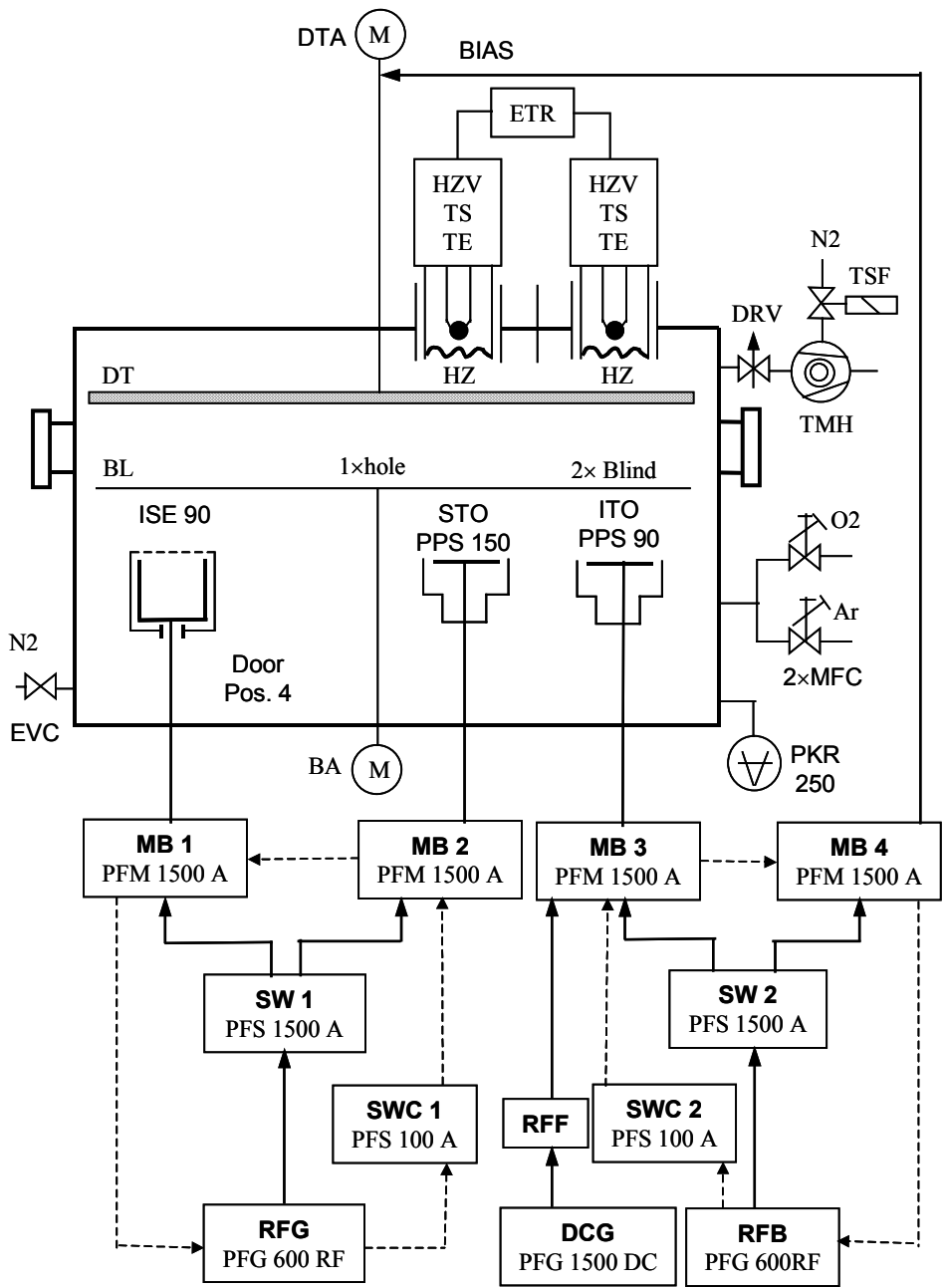


Figure 3-4 Function layout of the sputtering system

3.2 Experiment Method and Procedures

The quartz substrates with diameter 25 mm were degreased ultrasonically in acetone solvents firstly. Then they were cleaned by ethylether furtherly. In order to produce an edge for the thickness measurement by a profilometer, a line was marked on the substrate with a felt pen before coating and removed later together with the material deposited on top of it. The substrates were put into the chamber after they were weighed by a balance. In every run, two substrates that were mounted on a circular table above the target, one in the center (“central sample”) and the other one at the periphery of the table (“peripheral sample”), were coated simultaneously.

The vacuum chamber was evacuated down to a base pressure of 2×10^{-5} mbar prior to the deposition. The argon and oxygen were then introduced into the chamber. The target was presputtered 10 min. in the chosen Ar/O₂ mixture. Then the blind was rotated to a proper position, the deposition was starting.

3.3 Substrate Temperature

The substrate table where the substrates are mounted is illustrated in scale in Figure 3-5. Two quartz substrates with a diameter of 25 mm are separated in 30 mm. Before deposition, the substrates on the holder were heated by carbon radiators to the desired temperature. The goal temperature was set and controlled by the Euro thermal controller. Since the substrate temperature is a key parameter for the film properties, it must be controlled and monitored properly. In practice, a thermoresistor Pt100 is mounted on the backside of the substrate and the temperature (T_{ob}) there is measured during sputtering. However, the temperature on the coated side (T_{sub}) rather than the backside of the substrate is what really to be concerned. Therefore, in advance, the temperature T_{sub} was measured by fixing a Pt100 on the coated side, and the correlation between T_{sub} and T_{ob} was derived. Consequently, the temperature T_{sub} can be obtained by measuring the T_{ob} .

In order to investigate the distribution of the temperature above the substrate holder, the thermometer Pt100 was mounted in the center and at the periphery of the holder both on the backside and coated side, respectively. The experimental results revealed that the temperature (T_{ob}) varying across the backside of the table is less than 5°C. However, the temperature (T_{sub}) difference between the central and peripheral sample on the coated side is about 50°C.

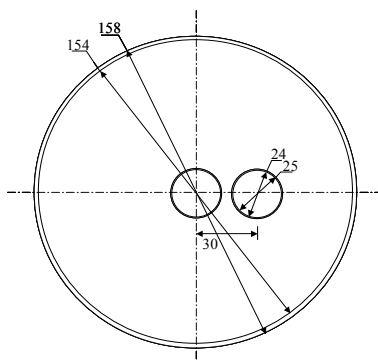


Figure 3-5 Schematic illustration of the substrate holder

4 Characterization of ITO Films

In this work, the mass of the film was measured by a comparator balance Sartorius C50; the geometrical thickness was determined by a Tencor P10 profilometer; optical transmittance and reflectance spectra were measured using a Perkin-Elmer Lambda-9 spectrometer; x-ray diffraction patterns were obtained with a Siemens Me 200 CY2 x-ray diffractometer; the sheet resistance was determined by a four-point probe; the surface morphology was measured by an atomic force microscope (Thermomicroscopes AutoProbe CP Research). Next the working principles of these devices and the corresponding properties of ITO films that can be characterized by them will be briefly described respectively.

4.1 Measurement of the Mass of the Films

The mass of the films was estimated by weighing the substrate before and after deposition with a comparator balance Sartorius C50 (Sartorius AG).

The principle of the balance is to compare the unknown test weight (T) with a known reference weight (R) and read the difference ($D = T - R$) between the two weights. The specifications of the Sartorius C50 are as following:

- Maximum overload capacity: 50.5 g
- Weighing capacity and range levels: 550 mg
- Readability: 0.001 mg

The possible errors and the corresponding actions carried out to reduce the errors are listed in Table 4-1.

Table 4-1 The possible errors and actions for high-precision mass determination

Possible Errors	Action
Repeatability	Repeat the measurements many times and calculate the mean value
Drift of displayed value (temperature)	Repeat the measurements many times, to find out the systematic drift
Span deviation	Adjust span or minimize the difference D by adding small known weights to smaller weight
Different density of weight material (air buoyancy)	Correct the effect according to known equation

4.2 Determination of the Film Thickness

Film thickness is one of the very important attributes of the films to be determined. The reason is that many properties of the films are dependent on the film thickness and other parameters such as mass density can be derived from thickness. There are various methods to measure the film thickness, which can be classified into optical method and mechanical method. In this work, both techniques have been used.

4.2.1 Stylus Method-Profilometer

The geometrical thickness was determined at a film edge by a TENCOR P-10 profilometer in this work. The TENCOR P-10 is a computerized, highly sensitive surface profiler that measures roughness, step height, and other surface characteristics in a variety of applications. During measuring, a diamond-tipped stylus directly contacts the surface and follows height variations as the sample is moved. The height variations are converted into electrical signals, producing a profile. The resulting trace represents a cross-sectional view with high vertical and spatial resolution.

The measurement range spans distance from 200 Å to 65 µm, and the vertical resolution is ~10 Å. Several factors limiting the accuracy of stylus measurements are:

- Stylus penetration and scratching of films. This is sometimes a problem in very soft films.
- Substrate roughness.
- Vibration of the equipment.

In order to produce a step on the films, a line was marked on the substrate with a felt pen before coating and removed later together with the material deposited on the top of it. Film thickness is thus directly read out as the height of the resulting step-contour trace. The mark line is made to about 5 mm long, located at the edge of the substrate along its diameter. The measurements are always carried out on the inner side of the mark. In order to reduce the measuring error, a mean value of four measurements at different positions was taken. Consequently the effective film thickness is derived (see section 5.2.2.2).

4.2.2 Optical Spectrum Simulation

In this work, optical transmittance and reflectance spectra were fitted with a computer model (SCOUT 98) based on dielectric modeling. A general method is described detailed in section 5.1.1.

In the case of layered systems, a very powerful technique to interpret optical spectra is given by a simulation of the experiment and adjustment of the model parameters to fit the measured data (Theiss). Since rather simple models of dielectric functions lead to a realistic simulation of optical spectra, it enables quick parameter fits from which the wanted information including the film thickness can be obtained.

The following five standard steps are required for optical spectra simulation.

1. Define the optical constants of all relevant materials.

Either fixed optical constants (imported from the files or database of the program) or optical constant models can be used to define each material. Optical constant models are composed of susceptibility terms which are enable to adjust optical constants to fix experimental data flexibly.

2. Define the structure of the layer stacks

The relevant materials (films, substrate and the ambient involving) of the sample is listed in sequence to construct a layer stacks. The optical constants defined in step 1 are also distributed to each material here.

3. Define which type of spectra are to be simulated and compared to experiments

Transmittance, reflectance, absorbance, ATR, and ellipsometry can be treated in this program.

4. Select the fit parameters

The parameters of the model that are to be adjusted in order to reach optimal agreement between the simulations and measurements can be selected and listed in this step.

5. Fit of the model (manual, visual, automatic)

The parameters of optical model selected in step 4 can be varied manually (type in new values) or visually (by mouse-driven sliders) or automatically with the method of downhill simplex in this program.

4.3 Measurement of Transmittance and Reflectance Spectra

It is a very effective and common method to characterize the thin films by means of analyzing their optical spectra, e.g. the transmittance and reflectance. In this study, the measured transmittance and reflectance curves were fitted with simulated curves by a computer program-Scout 98 (Theiss). From the optical spectra simulation, film thickness, free carrier density, band gap, and free carrier mobility can be then obtained (Mergel and Qiao 2001). However, an accurate measuring of the optical spectra is imperative for the following studies. In this section, the experimental set-up and its working principle are introduced briefly. Furtherly, the exploring in this work to obtain a good reflectance is described in detail.

4.3.1 Principle

In this work, the transmittance and reflectance spectra were measured with a Perkin Elmer Lambda 9 spectrometer. It is a total reflective double-beam spectrometer. The working spectral range is from 190 nm to 3200 nm (for transmittance), covering the ultra-violet (UV), visible and near-infrared (IR) spectrum. For UV radiation the deuterium lamp is used and halogen lamp gives off visible and IR radiation. The changing of the sources happens at 319.2 nm. Two kinds of detectors are also used for different ranges respectively and they are shifted at 860.8 nm. The working principle is illustrated by a diagram in Figure 4-1.

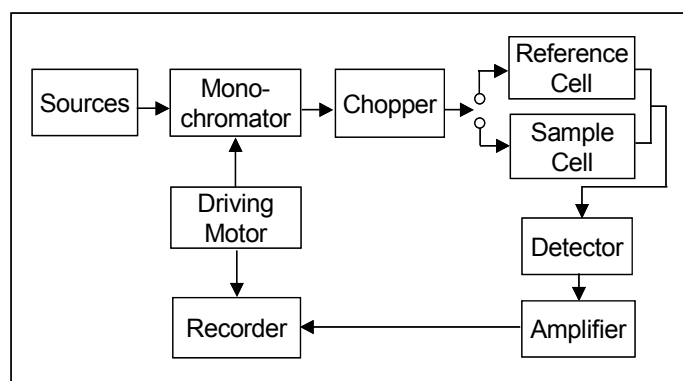


Figure 4-1 The diagram of the principle of the spectrometer.

4.3.2 The Approach to the Spectra Measurement

For transmission measurements the ITO sides of the samples were irradiated under perpendicular angle of incidence. The reference used was air, i.e. the data

presented in this work contain the transmission of ITO including the substrate. The reflection measurements were carried out under an angle of incidence of 7° .

Since this spectrometer is originally equipped for transmission spectrum measuring, it must be modified by attaching two accessories (shown in Figure 4-2) in order to measure the reflectance. For highly accurate measurements, one reflectance accessory containing the reference material is installed in the reference beam of the spectrometer, whereas the second reflectance accessory where the sample is mounted is installed in the sample beam. The reference substance inserted into the reference cell should be such a material that its reflectance is comparable to that of the measured sample, especially in the region of IR detecting. This can ensure the difference of the light intensities coming from the sample cell and the reference cell is not too large.

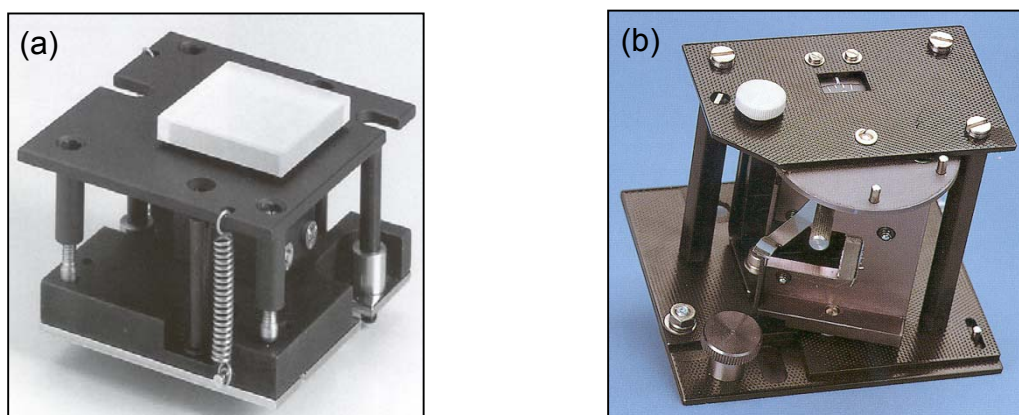


Figure 4-2 Variable-angle reflectance accessories (a) is installed in the sample cell. Its reflective angel is fixed with 6° , (b) is mounted in the reference cell. The reflective angel is variable from 15 degree to 70 degree with $\pm 1^\circ$ accuracy

Figure 4-3 shows the sketch of the optical path for the accessory placed in the sample cell. The sample beam impinges and is reflected by the left flat mirror. And then goes to and is reflected by the sample with 6° angle. Finally the radiation is reflected by the right mirror and thus the original incident direction is kept. In this way, the reflectance of the sample could be measured.

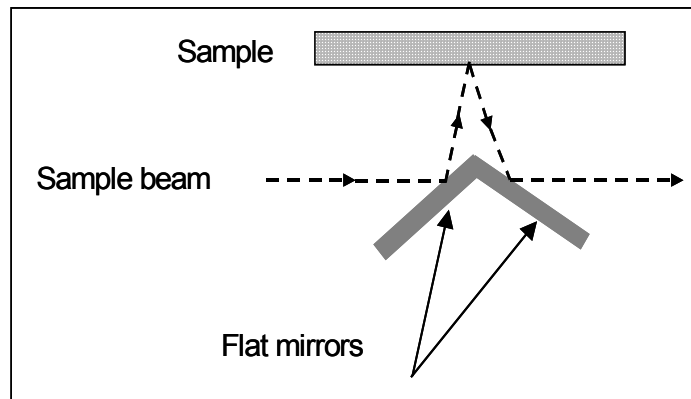


Figure 4-3 Sketch of the optical path of B008-6703, Angel 6°

For the transmittance measurement, the first procedure is to measure the transmittance of a “blank material” (usually is air), which is regarded as the background value with a transmittance of 100%. And then the sample is put into the sample cell and measured. Consequently, the recorded transmittance of the sample is a percent of that of the blank material (air). Since the transmittance of the air is a constant (100%) in the whole spectral range, the transmittance measuring is quite simple and accurate.

In principle, the method of the reflectance measuring is the same as that of transmittance, *i.e.* the quantity measured in specular reflectance is a percent reflection and this is normally compared to a material of which reflectivity is known. Unfortunately there is not a material whose reflectance is simply a constant in the whole spectral range. Therefore, a material whose reflectance has been known as a function of the wavelength must be firstly measured as the background value (R_{blank}), and then the reflectance of the sample is measured (R_p). Consequently, the absolute reflectance (R_a) of the sample is derived by the following equation

$$R_a(\lambda)\% = R_p(\lambda)\% \times R_{\text{blank}}(\lambda) \quad (4.3.1)$$

In this study, the quartz substrate was taken as a “blank material” because its reflectance is almost constant in a large spectral range. In order to get the reflectance of quartz as a function of the wavelength, first, we calculated the reflectance R according to the formula

$$R = (1 - T)/2, \quad (4.3.2)$$

where T is the measured transmittance. The factor of 1/2 in the right side of the formula is account for the backside of the quartz is matted. However, this reflectance is not exactly correct, because there are also scattering and absorption when the incident light passes through the material. Therefore the calculated reflectance of the quartz must be calibrated.

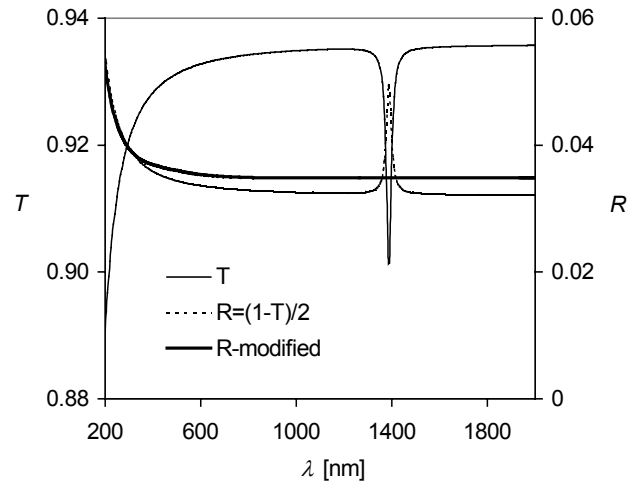


Figure 4-4 The measured transmittance curve and the modified and calculated reflectance curve (derived from the formula $R = (1-T)/2$) of quartz

In order to calibrate the reflectance of the quartz, four high reflected mirrors were selected. Their reflectances are listed in Table 4-2, which were provided by Perkin Elmer Company in Überlingen measured with Lambda 900 Spectrometer and VN-equipment. The modified reflectance of the quartz is shown in Figure 4-4.

Table 4-2 The wavelength (range) and the reflectance of the standard high reflectance mirror (Perkin Elmer AG)

	HR-1	HR-2	HR-3	HR-4
Wavelength (nm)	220	420	370-520	800-850
Reflectance (%)	96	98.2	~ 100	~ 100

4.3.3 Measuring Results

In order to check the accuracy of the modification, an Al mirror and another HR mirror which reflectivity is nearly 100% from 700 – 900 nm were measured and calculated. The experimental results fit the standard values quite good in different ranges.

According to the technical data from the Perkin Elmer, the measuring error for transmittance is 0.1% to 0.3%. Under the best condition that the scanning speed is slow and the interval for sampling is long enough, the smallest error can be achieved. For reflectance, the error would be 3%, since there are more processes. It has been found in this work that the quality of the reflectance spectra is also sensitive to the scanning speed of the spectrometer.

4.4 Determining the Structure of ITO Films by X-ray Diffraction

X-ray diffraction (XRD) is a very important experimental technique in revealing the crystal structure of bulk solid microstructure of thin films. The XRD methods are generally applied to films thicker than several angstroms on account of the strong penetrating power of the x-ray. Many informations related to the crystal structure of the films, including lattice constants, grain size, preferred orientation of polycrystals, defects, stress, etc. can be determined from the x-ray diffraction measurement.

X-rays are electromagnetic waves. The phenomenon of the x-ray diffraction by crystals results from a scattering process in which x-rays are scattered by the electrons of the atoms without change in wavelength. A diffracted beam is produced by such scattering only when certain geometrical conditions are satisfied, which may be expressed in either of two forms, the Bragg law or the Laue equations. The resulting diffraction pattern of a crystal, comprising both the positions and intensities of the diffraction effects, is a fundamental physical property of the substance. Analysis of the positions of the diffraction effect leads immediately to a knowledge of the size, shape and orientation of the unit cell.

The equipment used in this work is a Siemens Me 200 CY2 x-ray diffractometer with $\text{CuK}\alpha$ radiation with wavelength 1.5405 \AA . The XRD spectra were collected in the $15 - 85^\circ$ of 2θ range with a measurement step of 0.01° . Crystallite size and lattice parameters were determined by Scherrer formula and Bragg equation from the main diffraction peaks respectively.

4.4.1 Information Obtained from the X-ray Diffractogram

A typical x-ray diffraction pattern together with the line spectrum of In_2O_3 powder (dashed lines (PDF 1991)) is shown in Figure 4-5. In order to characterize the microstructure of the films, three parameters should be obtained from the diffractograms: the position of the peaks 2θ , the height of the peaks h and the width at the half height of the peaks w .

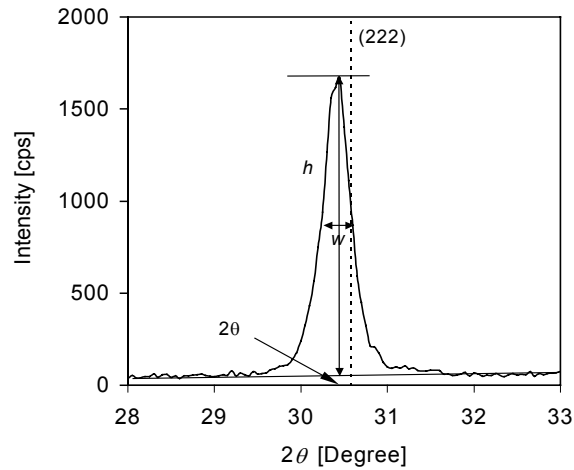


Figure 4-5 The (222)-reflex of XRD for an ITO film (the dot line represent the theoretical position of this peak)

(1) Lattice distortion

The distance between the two adjacent lattice planes is derived from the experimental peak position by means of Bragg formula:

$$d_{\text{exp}} = \lambda_0 / 2 \sin \theta, \quad (4.4.1)$$

whereas its theoretical value d_{hkl} can be calculated from the lattice constant ($a_0 = 1.0118 \text{ nm}$) by:

$$d_{hkl} = \frac{a}{\sqrt{h^2 + k^2 + l^2}}, \quad (4.4.2)$$

where h , k and l are Miller indices of the corresponding lattice planes (Figure 4-6).

A characteristic shift towards lower angle compared to the reflex of ideal crystals is observed for (222)-peak in Figure 4-5. This indicates a lattice expansion. The lattice distortion ($\Delta d/d_0$) is defined as:

$$\Delta d / d_0 = (d_{\text{exp}} - d_{hkl}) / d_{hkl} \quad (4.4.3)$$

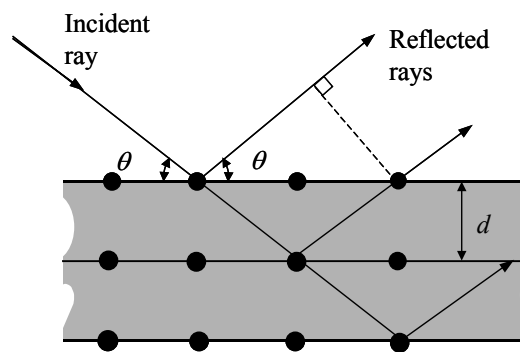


Figure 4-6 Reflection of x-rays from a crystal

(2) Grain size

The coherence length D of the scattering material is determined from the half-width w of the reflexes by means of the Scherrer formula:

$$D = \frac{K\lambda}{w' \cos(\theta)} \quad (4.4.4)$$

$$w' = \sqrt{w^2 - \delta^2} \quad (4.4.5)$$

with δ being the resolution of the spectrometer, here 0.01° , K is a shape factor and assumes a value of 0.9 for spherical particles (Mergel et al 2001).

(3) Texture

Usually, the polycrystalline is such a crystal aggregates whose orientations may deviated widely from complete randomness, which is said to possess *texture*.

In order to compare the reflex intensities of different orientations they are usually normalized with the tabulated peak heights of the powder diffractograms (PDF 1991).

We are looking for a normalization of the x-ray peaks that yield quantities that are proportional to the fraction of the material with the corresponding crystalline orientation. For such a normalization, approximately equal values for the total normalized scattering power are to be expected for crystalline films with the same thickness. In this work, the fraction F_m of the grains with orientation m is obtained by:

$$F_m = \frac{h_m w_m^3 \cos^3(\theta)}{p_m} * K, \quad (4.4.6)$$

where K is independent of the diffraction angel, p_m is the corresponding powder peak height. The detailed and complete elucidation of this calculation can be referred in (Mergel et al 2001).

4.4.2 Evaluating X-ray Diffractograms by Computer Program

The reflexes of the x-ray diffraction were evaluated either manually or by a computer program in this work. The manual method is precise but too much time consuming. Therefore, a computer program was introduced, which was composed by Kovac (2002). The algorithm of the program is based on isotonic and antitonic regression. Four parameters should be input to the program: the threshold, length of smallest interval for multirevolution decomposition, minimum number of the data points of a maximum and minimum number of the data points of a minimum. The smoothed spectrum, baseline, and the position, height and half width of the peaks

are exported automatically after the program is run. The precise of the results are strongly dependent on the four input parameters. According to our experiences, the best results could be obtained with the parameters of 5, 8, 8, and 20. In order to evaluate the program, the results were compared with that derived from the manual method. Ten ITO samples with various thicknesses were selected. Averagely, each film possessed about 10 peaks, therefore nearly 1000 peaks have been evaluated. The average ratios of the manual results to the program results (with the optimal parameters) of the 2θ , h , k for each sample are listed in Table 4-3. The values in the brackets are the standard deviations for the last one or two digitals of the ratios.

Table 4-3 Evaluation of the computer program by comparing it with the manually results (the parameters input to the program is 5; 8; 8; 20)

Sample	2θ	h	w
mi-0.05 μm	0.9983 (12)	1.06 (2)	0.89 (11)
mi-0.1 μm	1.0010 (21)	1.07 (1)	1.05 (8)
mi-0.3 μm	0.9991 (11)	0.91 (24)	0.92 (34)
mi-0.4 μm	0.9996 (7)	0.96 (11)	0.99 (9)
mi-0.5 μm	0.9999 (8)	0.98 (12)	1.09 (17)
mi-0.65 μm	1.0001 (9)	0.99 (9)	1.05 (8)
mi-0.8 μm	1.0001 (7)	0.93 (11)	1.06 (16)
mi-1.0 μm	1.0003 (8)	0.94 (13)	1.05 (15)
mi-1.35 μm	1.0005 (6)	0.99 (8)	1.02 (19)
mi-1.75 μm	1.0005 (6)	0.99 (4)	1.04 (12)

It can be observed from the table that the precision of the peak position is rather high. And generally, the reliabilities of the height and half width are also satisfied. But in some special cases, such as when the peak locates on the broaden background peak resulting from the substrate, the results from the program will be completely wrong. Therefore, the program method is suggested to be used under the visual detection.

4.5 Determining the Electrical Resistivity of the Films

The four-point probe is a very versatile device used widely for the investigation of electrical phenomena. The effect of the contact resistance could be eliminated with the use of such configuration. The most common in-line configuration has been adopted in this work (see Figure 4-7).

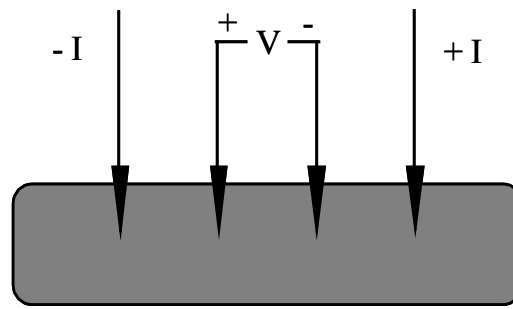


Figure 4-7 Schematic of in-line four-point probe configuration

In the measurement, the four metal tips have been attached to the test sample. A high impedance current source of $I = 30$ mA has been used to supply current through the outer two probes; a voltmeter measured the voltage V across the inner two probes. The probe spacing was 1 mm. Consequently, the sheet resistance of the film is derived from the formula:

$$R_s = \frac{\pi}{\ln 2} * \frac{V}{I}, \quad (4.5.1)$$

where the factor of $\pi/\ln 2$ is on account of the effect of the current extending. If the film thickness is known, the resistivity is readily obtained from

$$\rho = R_s d, \quad (4.5.2)$$

where d is the film thickness. The mean value of three measurements has been taken in order to reduce the measuring error.

4.6 Measuring the Surface Morphology by AFM

The surface morphology and roughness of the films were measured by an atomic force microscopy (Thermomicroscopes AutoProbe CP Research).

The atomic force microscope (AFM) is a recently developed advanced microscopy and surface analysis instrument, which was invented by Binnig, Quate and Gerber (1986). The importance of its invention was marked by the award of a Nobel Prize to its inventor in 1986. The AFM is a powerful addition to microscopy, surpassing light and electron microscopy through its ability to generate high-resolution 3D images at nanometer resolution with no sample pre-treatment and working in air or liquid environments. Both conducting and dielectric materials can be detected by AFM.

Working principle

Like all other scanning probe microscopes, the AFM utilizes a sharp probe moving over the surface of a sample in a raster scan. In the case of the AFM, the probe is

a tip on the end of a cantilever which bends in response to the interaction force, usually of the order of nano-newtons, between the tip and the sample.

The principle of an AFM is illustrated in Figure 4-8. During the probe is raster scanning across the surface, a constant force between the tip and the sample is maintained. As the cantilever deflects, which are caused by changes in surface stiffness or topography, the light from the laser is reflected onto the split photodiode. By measuring the difference signal (A-B), changes in the bending of the cantilever can be measured and used to generate a topographical image of the surface.

The movement of the tip or sample is performed by an extremely precise positioning device made from piezo-electric ceramics, most often in the form of a tube scanner. The scanner is capable of sub-angstrom resolution in x-, y- and z-directions. The z-axis is conventionally perpendicular to the sample.

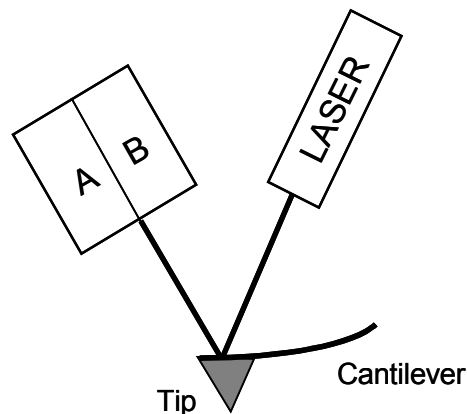


Figure 4-8 Working principle of the AFM

To optimize the study of different surfaces, the AFM can be operated under several modes. The most frequently used modes are contact mode and non-contact mode.

Contact mode is the most common method of operation of the AFM, in which the tip is held a few angstroms above the surface. The surface and the tip interact by repulsive forces. In contact mode, the resolution is very high, but there exist large lateral forces on the sample as the tip is "dragged" over the specimen. Hence it is not suitable for soft materials.

The alternative method for measuring the soft surface, such as biological and certain polymeric specimens, is known as the non-contact mode. In such measurements, the tip is held some tens of angstroms above the surface and is oscillated near its resonant frequency. However, the disadvantage of this method is a loss in lateral resolution as compared to the contact mode.

Surface roughness

A major goal of characterizing the surface roughness is able to understand the relationship between the microstructure and the properties of the films. The surface roughness determined by the AFM is the root mean square (rms) roughness, R_q , which is defined as (Amaral et al 2000):

$$R_q = \sqrt{\sum_i (z_i - \bar{z})^2 / N}, \quad (4.6.1)$$

where \bar{z} is the average height of the scanned area, z_i is the height value of each point and N is the number of the points including in the scanned area.

5 Results and Discussions

5.1 Dielectric Modeling of Optical Spectra

The main results of Section 5.1.1 and 5.1.2 have been published (Mergel and Qiao 2002).

5.1.1 General Method

The principal task of optical spectroscopy is to determine the microscopic structure or quantities, impurity concentrations or thin film thickness from the macroscopic measurements of optical spectra. This is realized by formulating the dielectric function, which is the “response function” of the material under the electric fields of the probing radiation. The dielectric function, $\varepsilon(\omega) = \varepsilon_1(\omega) + i\varepsilon_2(\omega)$, fully describes the optical properties of any homogeneous medium at all photon energies $\hbar\omega$ (Martinez 1992; Kim et al 1992).

5.1.1.1 Fundamental principles

The theoretical exposition in this and the following section is based on the Refs. (Hamberg and Granqvist 1986; Weijtens and van Loon 1991; Stenzel 1996). According to electromagnetic theory, the susceptibility χ of an isotropic medium is defined by

$$P = \varepsilon_0 \chi E \quad (5.1.1)$$

where P is the polarization of the medium and E is the external electric field. χ is taken as sum of individual susceptibilities χ_i arising from various physical mechanisms of polarization. The complex dielectric constant ε relative to vacuum is given as:

$$\varepsilon = \varepsilon_{re} + i\varepsilon_{im} = 1 + \sum_i \chi_i \quad (5.1.2)$$

The complex refractive index \tilde{n} is the square root of ε :

$$\tilde{n} = n + ik = \sqrt{\varepsilon_{re} + i\varepsilon_{im}} \quad (5.1.3)$$

where n is the refractive index and k is the extinction coefficient. Reflectance and transmittance spectra of thin films, $R(\lambda)$ and $T(\lambda)$, respectively, can be calculated when the optical functions $n(\lambda)$ and $k(\lambda)$ in the spectral region of interest and the film thickness d are known.

Dielectric modeling of optical spectra comprises several steps: (1) Formulae for the χ_i with free parameters are set up. (2) Initial values of the free parameters and of d are assumed. (3) Optical spectra are calculated and compared with their experimental counterparts. The parameters of χ_i and d are then varied so that the simulated spectra approach the experimental ones. We use the commercial computer program SCOUT 98 (Theiss) which applies a downhill simplex method to find the optimal fit parameters.

5.1.1.2 Standard model for doped semiconductors (ITO)

The optical properties of doped semiconductors in the spectral range of interest, 200 nm to 3 μm , are controlled by three types of electronic excitations: band gap transitions, interband transitions from the bulk of the valence band into the bulk of the conduction band, and intraband transitions of the electrons in the conduction band. They are, in a first approximation, modeled with standard formula available in the fit program as following.

(1) OJL model

For the band gap transitions, the OJL model (O'Leary, Johnson and Lim 1997) that has been proposed to model the band gap of amorphous silicon is used. It is based on parabolic densities of states below and above the mobility gap E_g and on exponential tails that are characterized by damping constants for the valence and conduction bands, γ_v and γ_c , respectively (see Figure 5-1).

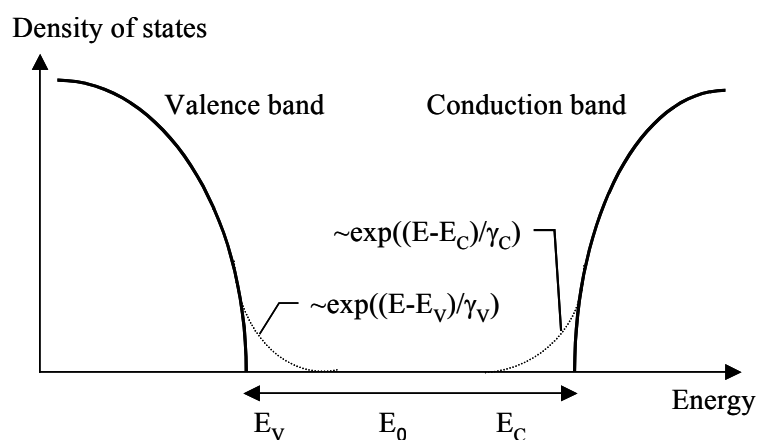


Figure 5-1 Band gap assumed by OJL model (Theiss)

The imaginary part of the dielectric function, ε_2 , is derived from the joint density of states $\Phi(\omega)$. Then, the real part, ε_1 , is obtained by a Kramers-Kronig transformation (KKR) of the imaginary part (see Eq. (5.1.4a) and Eq. (5.1.4b)). This procedure is implemented in the SCOUT 98 program.

$$\varepsilon_2(\omega) = \frac{4\eta^2 e^2}{\pi m^2 \omega^2} \Phi(\omega) \quad (5.1.4a)$$

$$\varepsilon_1(\omega) = 1 + \frac{2}{\pi} \int_0^\infty \frac{\omega' \varepsilon_2(\omega')}{\omega'^2 - \omega^2} d\omega' \quad (5.1.4b)$$

To account for the smooth onset of absorption at the band edge, an Urbach tail (Hamberg and Granqvist 1986) or indirect transitions (Weijtens and van Loon 1991; Sczyrbowski, Dietrich, and Hoffmann 1983) were introduced, in addition to a direct band gap.

(2) Harmonic oscillator

The interband transitions into the upper half of the conduction band are represented by a harmonic oscillator. This is a simplification because the UV dielectric spectrum of semiconductors usually exhibits a variety of critical points and lines. Nevertheless, the model is sufficient because only the low-energy tail of the corresponding susceptibility is relevant for the transitions in the spectral range below 40000 cm^{-1} (5 eV). The formula for the susceptibility of a harmonic oscillator reads:

$$\chi_{HO}(\omega) = \frac{O_{HO}^2}{a - ib} = \frac{O_{HO}^2 a}{a^2 + b^2} + i \frac{O_{HO}^2 b}{a^2 + b^2} \quad (5.1.5)$$

$$a = \Omega_{HO}^2 - \omega^2 \quad (5.1.5a)$$

$$b = \omega \Gamma_{HO} \quad (5.1.5b)$$

with the parameters: resonance frequency Ω_{HO} , damping constant Γ_{HO} and oscillator strength O_{HO} . At $\omega = 0$ we get:

$$\chi_{HO}(0) = \frac{O_{HO}^2}{\Omega_{HO}^4} \quad (5.1.6)$$

This means that the harmonic oscillator used to model interband transitions in the UV range contributes to ε_{re} and, consequently, to the refractive index n in the visible range although its absorption is nearly zero there.

The variables and parameters used in these and other formulae referred to later are listed in Table 5-1.

Table 5-1 Nomenclature

Variable or parameter	Description	Equation No.
<i>Angular frequencies [s⁻¹, eV or cm⁻¹]</i>		
Ω_{Dr}	Drude frequency	5.1.7; 5.1.8; 5.1.9
Ω_p	Plasma frequency, $\epsilon_{re}(\Omega_p) := 0$	5.1.9
Ω_{HO}	Harmonic oscillator, resonance frequency	5.1.5a
O_{HO}	Harmonic oscillator, strength	5.1.5
Γ_{HO}	Damping of Harmonic oscillator	5.1.5b
Γ_{Dr}	Damping of Drude oscillators	5.1.7; 5.1.9; 5.1.10
<i>Densities [cm⁻³]</i>		
N_{Dr}	Carrier density from Ω_{Dr}	5.1.8
n_{dc}	Direct current carrier density from Hall effect	5.1.12
<i>Mobilities [cm²V⁻¹s⁻¹]</i>		
M_{Dr}	Mobility of Drude oscillators derived from Γ_{Dr}	5.1.11
μ_{dc}	Direct current mobility	5.1.12

(3) Drude model

The Drude model is used to describe the free electrons contribution to the dielectric function for metals. In the case of doped semiconductors, this model can be used also because free carriers introduced into semiconductors by doping behave in many ways like those in simple metals.

The classical Drude formula used for the susceptibility of free electrons is:

$$\chi_{Dr}(\omega) = -\left[\frac{\Omega_{Dr}^2}{\omega^2 + \Gamma_{Dr}^2} \right] + i \left(\frac{\Gamma_{Dr}}{\omega} \right) \left[\frac{\Omega_{Dr}^2}{\omega^2 + \Gamma_{Dr}^2} \right] \quad (5.1.7)$$

with the Drude frequency Ω_{Dr} defined as:

$$\Omega_{Dr}^2 = \frac{e^2 N_{Dr}}{\epsilon_0 m_{eff}} \quad (5.1.8)$$

Here, N_{Dr} is the free electron density and m_{eff} is the effective mass at the bottom of the conduction band. Γ_{Dr} is a damping constant. The response of the free carriers to an optical excitation corresponds to a high pass filter.

Eq. (5.1.8) can be used to obtain the free carrier density from optical spectra when the effective mass is known. We designate the electron density thus obtained by

N_{Dr} , whereas the carrier density derived from direct current Hall effect measurements is called N_{dc} . The effective mass m_{eff} can be determined when the Drude frequency and the carrier density are known from optical and Hall effect measurements, respectively, provided that the density of optically active carriers is the same as that of the electrically active carriers.

The longitudinal plasma frequency Ω_p is obtained by setting $\varepsilon_{re} = 0$, yielding:

$$\Omega_p = \sqrt{\frac{\Omega_{Dr}^2}{\varepsilon_\infty} - \Gamma_{Dr}^2} \quad (5.1.9)$$

where ε_∞ is the dielectric number in the relevant spectral region around Ω_p arising from all transitions except the Drude oscillations. Sometimes, Ω_{Dr} is also called plasma frequency. This may, however, cause confusion, so that we prefer the name ‘‘Drude frequency’’. The strong increase of absorption and reflection in the spectrum at the plasma frequency Ω_p is called plasma edge.

The mobility of the free carriers is derived from the damping constant via the average collision time $\langle \tau \rangle$:

$$\langle \tau \rangle = \frac{1}{\Gamma_{Dr}} \quad (5.1.10)$$

$$M_{Dr} = \frac{e \langle \tau \rangle}{m_{eff}} \quad (5.1.11)$$

The mobility thus obtained is designated by M_{Dr} whereas μ_{dc} (direct current mobility) is used for the mobility obtained by means of direct current Hall effect and conductivity measurements.

$$\sigma = n_{dc} e \mu_{dc} \quad (5.1.12)$$

Within the framework of the Drude theory, the density of free electrons determines the position of the plasma edge. The mobility is related to the damping of the electron oscillations which in turn determines the width of the plasma edge. Only few authors checked this relationship experimentally.

5.1.2 Results for ITO Films

$\text{In}_2\text{O}_3:\text{Sn}$ (ITO) is an n -type heavy doped semiconductor. In order to optimize the dielectric models for ITO films, a series ITO films with the carrier density varying from 3×10^{19} to $1.5 \times 10^{21} \text{ cm}^{-3}$ were selected to be simulated.

5.1.2.1 Sample preparation and characterization

The ITO films were prepared by radio-frequency diode sputtering of an oxidic target by a Perkin-Elmer 2400 system (Ehl 1997). The substrate temperature was 380°C. The Ar-flux was 20 sccm with an O₂-admixture of 0 to 10% in order to get various carrier densities. The glass substrates (Schott, BK7) measured 26 mm x 26 mm. The density and the direct-current mobility of the free electrons were determined by Hall Effect and conductivity measurements in van der Pauw geometry (van der Pauw 1958). Transmittance spectra in the range 180 nm to 3 μm were measured in a Perkin-Elmer Lambda-19 spectrometer.

The deposition process and its influence on structural and electrical properties were described elsewhere (Mergel et al 2001).

5.1.2.2 Modification of standard model

(1) Standard model

A spectrum for a sample with $n_{dc} = 4.25 \times 10^{20} \text{ cm}^{-3}$ is shown in Figure 5-2 together with simulated spectra, where the fitting with the standard model is shown by the dotted line. It is shown that the average experimental spectrum is well represented but its specific features are reproduced badly. The fit misses the positions and amplitudes of the interference extreme and also the correct curvature of the plasma edge. The deviations arise because the optimal fit of the Drude model predicts too strong an absorption in the visible region. If, in a suboptimal fit, the parameters are tuned to yield a better fit in the visible region, the curvature at the plasma edge becomes too steep. There are also some deviations in the band gap region indicating that the OJL model cannot cope for the smooth onset of absorption at the band edge.

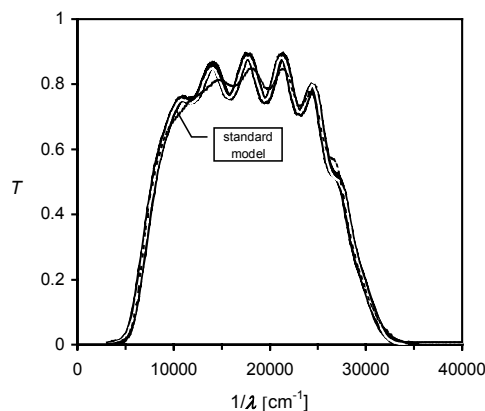


Figure 5-2 Experimental transmittance spectrum and its simulation with the standard (- - -) and the modified (white line on the experimental curve) dielectric model

The frequency-dependent susceptibilities resulting from a fit of the three aforementioned transitions to the spectrum of ITO film (its transmittance is displayed in Figure 5-2) are shown in Figure 5-3, designate by "stand.". The region where T is detectably bigger than 0 is indicated by vertical dashed lines. The imaginary part, indicated by the shaded area, looks like a band pass limited to lower energies by the free carrier excitations and to higher energies by the interband transitions. The real part, ε_{re} , ("stand., re") satisfies the Kramers-Kronig relation (KKR) and exhibits a negative and a positive divergence when the frequency approaches 0 or Ω_{HIO} (here 45800 cm^{-1}), respectively. The contribution of the free electrons to ε_{re} is shown in the lower part of Figure 5-3. It is always negative because the free electrons move out of phase with the driving electric field due to their mass inertia and the absence of a restoring force.

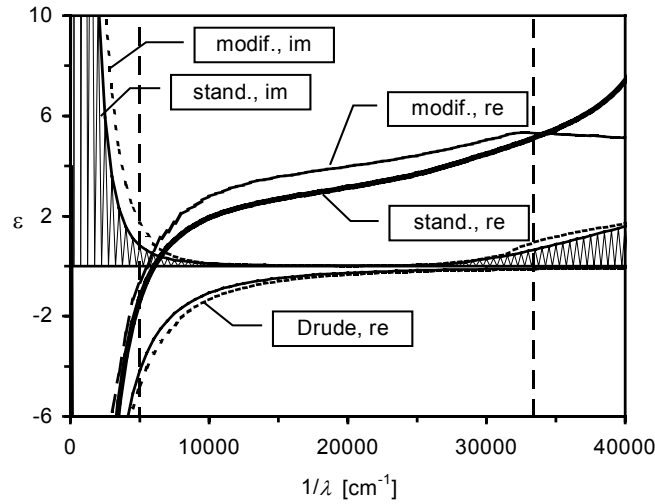


Figure 5-3 *Dielectric function (real and imaginary part) used to simulate the spectrum shown in Figure 5-2, calculated with the standard and the modified model*

In order to improve the fitting, a refined Drude model and a different band gap model that allows for direct and indirect transitions were applied. This yields a visually satisfying fit to the experimental spectrum (see the white line within the experimental curve in Figure 5-2), with a standard deviation of 0.003 instead of 0.017 before. The details of the refined models are discussed in the following sections.

(2) Refined Drude model with frequency-dependent damping.

In order to get a better fit to the curvature of the plasma edge, a frequency-dependent damping factor with four fit parameters is introduced:

$$\Gamma_{Dr}(\omega) = \Gamma_L - \frac{\Gamma_L - \Gamma_H}{\pi} \left[\arctan\left(\frac{\omega - \Omega_{\Gamma Dr}}{\Gamma_{\Gamma\omega}}\right) + \frac{\pi}{2} \right] \quad (5.1.13)$$

where Γ_L is the low-frequency damping, Γ_H is the high-frequency damping, $\Gamma_{\Gamma\omega}$ is the changeover width, $\Omega_{\Gamma Dr}$ is the changeover frequency. The resulting optimal $\Gamma_{Dr}(1/\lambda)$ curves are shown in Figure 5-4 for four samples with different q_{o2} . The Drude frequencies are indicated by vertical bars. The vertical dot lines in the left and right indicate the measuring range of the optical spectra. The changeover frequency is proportional to the plasma frequency, $\Omega_{\Gamma Dr} \sim 0.75\Omega_{Dr}$, also for the samples not represented in Figure 5-4.

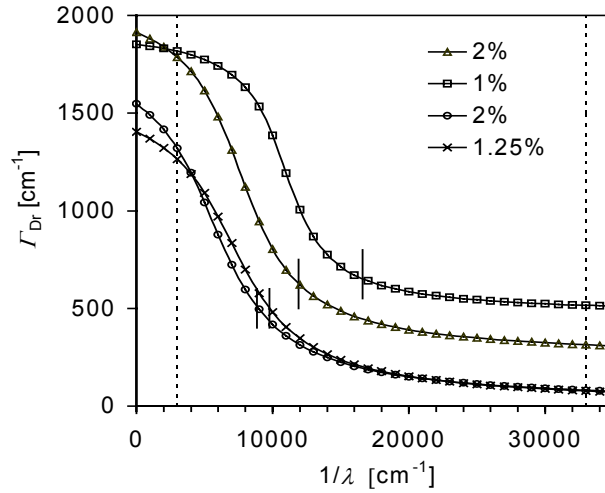


Figure 5-4 *Frequency dependent damping factor $\Gamma_{Dr}(1/\lambda)$ for four representative samples. The region between the left and right dash lines is covered by the optical spectra. The middle dash line shows the average value of the plasma frequencies derived by standard Drude model*

For the samples with $\Omega_{Dr} > 8000 \text{ cm}^{-1}$, the low-frequency damping factor scatters around 1800 cm^{-1} (0.22 eV) whereas the high-frequency damping factor is at least one order of magnitude lower and sometimes nearly reduced to zero on this scale. This is consistent with literature. Values of 0.2 eV (1600 cm^{-1}) below and 0.05 eV (400 cm^{-1}) above Ω_{Dr} are reported for a film with $n_e = 1.3 \times 10^{21} \text{ cm}^{-3}$ ($\Omega_{Dr} = 1.4 \text{ eV}$, 11300 cm^{-1}) (Hamberg and Granqvist 1986). The corresponding values for Ref. (Köstlin, Jost and Lems 1975) are 0.24 eV (1900 cm^{-1}) and 0.1 eV (800 cm^{-1}) as can be evaluated from the detailed data given in that reference.

Eq. (5.1.13) has been introduced formally and is successful primarily, because more fitting parameters are introduced. As an alternative, we modeled the plasma edge with the standard Drude model plus a harmonic oscillator (Monterrat, Boy and Marcel 1998). This approach yields also a good fit to the experimental curves with an oscillator frequency of about 0.6 of the Drude frequency.

The success of the modified models proves that the fit of the classical Drude formula yields too strong an absorption for frequencies above the Drude frequency.

(3) Band gap with direct and indirect transitions

For direct transitions, a square root dependence of the joint density of states above the direct band gap E_{d0} is tried:

$$\Phi_{dir} = D\sqrt{(\eta\omega - E_{d0})}[1 - \text{step}(E_{d1})] \quad (5.1.14)$$

The step function limits the square root dependence to energies below E_{d1} . Indirect transitions are modeled according to:

$$\Phi_{ind} = I(\eta\omega - E_{ind})^2 \quad (5.1.15)$$

The interband transitions into the upper half of the conduction band are represented by a harmonic oscillator above E_{d1} as described by Eq. (5.1.5).

Heavily doped ITO is a degenerate semiconductor. The Fermi level lies inside the conduction band so that band gap transitions are shifted towards higher energies with increasing conduction electron density. This effect, known as Burstein-Moss (BM) shift, is introduced in Section 2.4.2.1. It has to be taken into account when band gap transitions are modeled.

When the transitions lead to that minimum in the conduction band that experiences the BM shift, the formulae have to be multiplied by a step function that suppresses transitions into states below the Fermi level. Depending on the assumed band model, only the direct, only the indirect or both transitions experience the BM shift. We tried several models but obtained basically the same result: all characteristic energies increase with increasing carrier density, not only those related to the Fermi level. For the direct transitions, the energy of transitions to the Fermi level was termed E_{Fd} .

The parameters E_{OJL} , E_{ind} , E_{d0} , and E_{Fd} are displayed in Figure 5-5 as a function of $N_{Dr}^{2/3}$. All follow the same trend. From fitting a straight line to $E_{Fd}(N_{Dr}^{2/3})$, we obtain, via Eq. (2.4.3), a combined effective mass $m_{vc}^* = 0.58m_e$. This compares to values $0.54m_e$ (O'Leary, Johnson and Lim 1997) and 0.525 (Hamberg and Granqvist 1986) in the literature.

In the literature, band gaps of $E_{ind} = 2.40 - 3.65$ eV ($19000 - 29500$ cm^{-1}) and $E_{dir} = 3.5 - 3.85$ eV ($28000 - 31000$ cm^{-1}) for zero electron density are reported; for an overview see (Weijtens and van Loon 1991). Our values for $N_{Dr} = 0$ are close to the lower limits of the reported ranges.

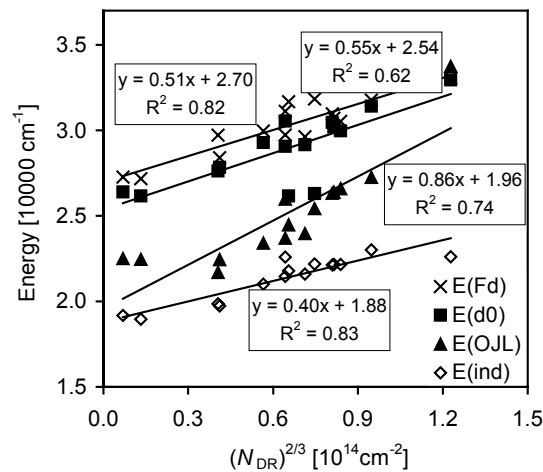


Figure 5-5 Band gap energies as a function of $N_{Dr}^{2/3}$, with N_{Dr} being the optically determined carrier density. $E(Fd)$: Fermi level; $E(d_0)$: direct band gap; $E(ind)$: indirect band gap; $E(OJL)$: band gap of the OJL model

5.1.2.3 Evaluation of the quality of the simulation

(1) Contributions to ε and n at 550 nm

Figure 5-6 shows the contributions of the considered three electronic excitations to ε at $\lambda = 550$ nm as a function of the carrier density N_{Dr} .

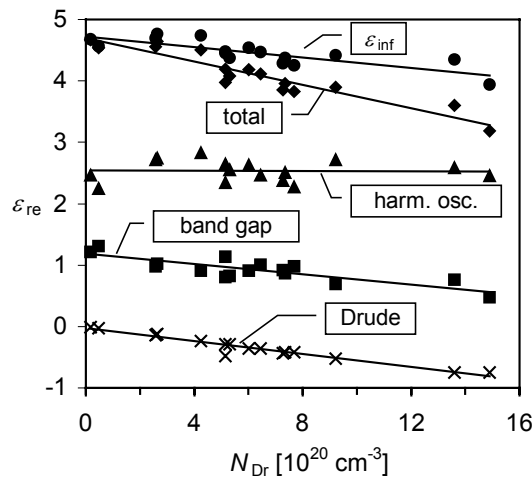


Figure 5-6 Value of the dielectric function at 550 nm and its contributions from free carriers (Drude term), ε_{Dr} , band gap transition, ε_{BG} , and bulk interband transition, ε_{HO} , modeled by a harmonic oscillator. ε_{inf} designates all contribution except the Drude term

It is shown in Figure 5-6 that the relationships are approximately linear. The Drude term is always negative. This is to be expected because the plasma wavelength is always bigger than 550 nm and approaches this value with increasing N_{Dr} . This

leads to an increasing value of ε_{re} due to the Kramers-Kronig relation (KKR). The maximum absolute value is $\varepsilon_{Dr} = 0.84$ for $N_{Dr} = 1.5 \times 10^{21} \text{cm}^{-3}$. The terms of the band edge due to direct and indirect transitions decrease with increasing N_{Dr} . This is explained by the Burstein-Moss shift of the transitions to higher energies, away from 550 nm and its influence on ε_{re} via the KKR. The contribution of the harmonic oscillator, representing transitions into the upper half of the conduction band is nearly independent of N_{Dr} , as to be expected.

The total dielectric constant changes from 4.6 for $N_{Dr} = 0$ to 3.1 for $N_{Dr} = 1.5 \times 10^{21} \text{cm}^{-3}$. This decrease is equally due to stronger free carrier absorption and the shift of the band edge. The contribution of the interband transitions plus vacuum ($\varepsilon = 1$) is 4.45 ± 0.2 . This is referred to as ε_{inf} in the literature where values between 3.7 and 4.6 were reported, see Ref. (Weijtens and van Loon 1991) for a review. A dependency of ε_{inf} on the free electron concentration was not explicitly stated so far. However, sometimes data are reported that show such a relationship. For radio-frequency sputtered films, it was found that ε_{inf} decreases from 4 for an electron density of $0.2 \times 10^{20} \text{cm}^{-3}$ to 3 for $5 \times 10^{20} \text{cm}^{-3}$ (Ohhata, Shinoki and Yoshida 1979). Our results are very close to those of Ref. (Weijtens and van Loon 1991) where $\varepsilon_{inf} = 4.48 \pm 0.15$ was obtained by ellipsometry with the tendency to decrease with increasing N_{Dr} . For our data we obtain:

$$\varepsilon_{inf} = 4.7 - 0.4 \times 10^{-21} [\text{cm}^3] N_{Dr} \quad (5.1.16)$$

When taking the OJL model instead of the direct and indirect transitions, the band gap contribution to ε (550 nm) is nearly zero. However, the variation of the harmonic oscillator term is larger such that within $\pm 1\%$ the same values for ε_{inf} as above are obtained.

The refractive index n decreases with the free electron density according to:

$$n = 2.17 - 0.24 \times 10^{-21} [\text{cm}^3] N_{Dr} \quad (5.1.17)$$

For radio-frequency magnetron sputtered films, a variation of the refractive index between 1.83 and 2.15 was reported with n being smaller for annealed films (Wu and Chiou 1993). The maximum carrier concentration was 1.5×10^{21} . This is in agreement with Eq. (5.1.17).

(2) Electronic properties

Eq. (5.1.8) predicts the square of the Drude frequency to be proportional to the free electron density. Therefore, in Figure 5-7, Ω_{Dr}^2 from the various models is plotted versus n_{dc} obtained from the Hall Effect. The diagonal represents Ω_{Dr}^2 calculated from n_{dc} with an effective electron mass of $0.35m_e$, the value reported in Ref. (Hamberg and Granqvist 1986). It is showed that N_{Dr} and n_{dc} are

approximately linearly correlated and N_{Dr} is bigger than n_{dc} , in the majority of cases. This means that there are optically active carriers that do not contribute to the direct current. This may be explained by isolated regions of the film that do not contribute to the direct current. Indications for such a microstructure were indeed found in an investigation of the structural properties of thin ITO films prepared in the same sputter apparatus (Mergel et al 2001). The experimental results presented there were explained by oxygen incorporation into the lattice at the surface of the growing film and segregation of oxygen and tin to grain boundaries in the subsurface region. Our films contain about 10 at.% Sn. In films with more than 5 at.% Sn an intergranular amorphous phase was revealed by transmission electron microscopy (Rauf and Yuan 1995). This may lead to badly conducting grain boundaries and electrically isolated grains.

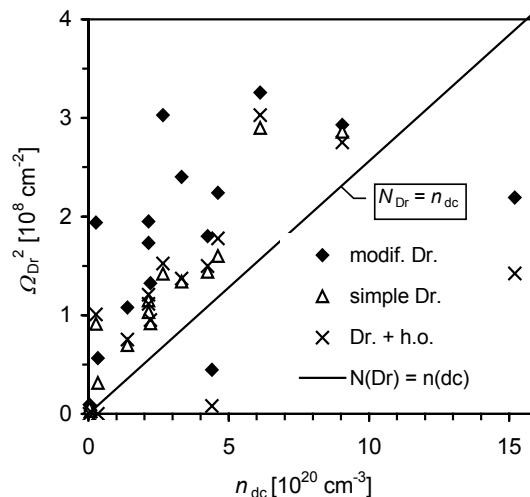


Figure 5-7 *Square of the Drude frequency Ω_{Dr}^2 for various models of the plasma edge as a function of the electrically determined electron density n_{dc} . The diagonal line represents Ω_{Dr}^2 calculated from n_{dc} with an effective electron mass of $0.35m_e$*

The mobilities derived from the original and the refined Drude models are compared in Figure 5-8 with the electrically determined values of μ_{dc} . It is evident that the optical mobility M_{Dr} is independent of and in most cases higher than the direct current mobility μ_{dc} . This may be due to an inhomogeneous microstructure with phases of different mobilities, e.g. crystalline and amorphous regions as discussed above. For direct current measurements, the current passes through the whole sample. The film acts like a network of conductors in series. The reciprocal of mobilities $1/\mu_{dc}$ has to be averaged and the lower mobility determines the average μ_{dc} . The optically excited electrons move only a short distance and do not leave the grains or the grain boundaries. They oscillate in parallel and the

mobilities M_{Dr} have to be averaged. As the grains occupy a much larger volume than the boundaries, M_{Dr} represents the mobility within the grains.

The mobilities at the Drude frequency reach a maximum of about $100 \text{ cm}^2/\text{Vs}$. This is the maximum value of the mobility found in flux-grown single crystals (Wen et al 1992) or in zone-confined thin films (Rauf 1993). The upper limit for degenerate ITO is determined by scattering at ionized donors (Bellingham, Philips and Adkins 1992). Generally, the mobilities reported in the literatures range from 10 to $70 \text{ cm}^2/\text{Vs}$, similar to the variation of our μ_{dc} values. Therefore, microstructural inhomogeneities of the discussed type are a general hindrance to obtain optimal resistivities.

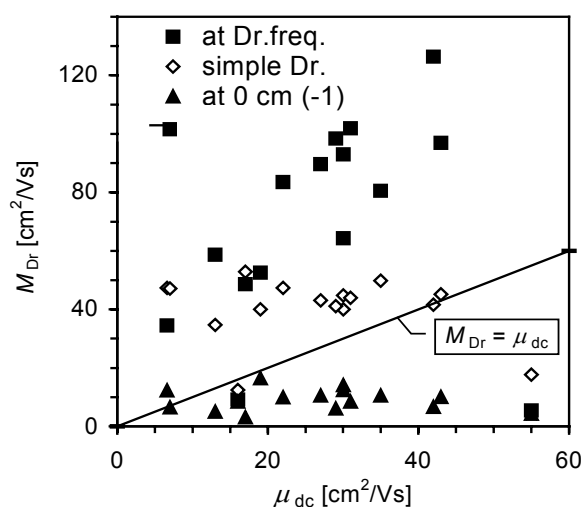


Figure 5-8 *Optically determined mobilities M_{Dr} vs. direct current mobility μ_{dc} . For the frequency-dependent damping the values at the Drude frequency Ω_{Dr} and at $1/\lambda = 0 \text{ cm}^{-1}$ are displayed*

(3) Band gap

In the literatures, several models were used to model the band gap transitions in In_2O_3 or in ITO (see Section 2.4.2). We tried several models but cannot decide clearly for a specific variant. All characteristic band gap energies shift to higher values with increasing electron densities in the same way indicating that all transitions experience the BM shift. This indicates that all band gap transitions go to the same conduction band minimum where the electrons are located. This result fits well to a recent band structure calculation (Odaka et al 2001). There, the conduction band was found to be electron-like with a minimum at the Γ point. The valence band consisted of many narrow and overlapping subbands. No indirect band gap was found. On the basis of this model, the details of the band gap transitions should be related to the details of the valence band structure.

(4) Film thickness

Film thickness is one of the most important parameters to evaluate the reliability of the simulation. The optically determined thickness was compared with that obtained from stylus measurements. The ratio of $d_{\text{opt}}/d_{\text{stylus}} = 1.00(10)$ and $0.95(3)$ for the standard and the $\Gamma_{\text{Dr}}(\omega)$ models were obtained, respectively. The number in brackets is the standard deviation of the last digit(s). The lowest standard deviation, namely 2%, is obtained from the Drude plus oscillator model: $d_{\text{opt}}/d_{\text{stylus}} = 0.98(2)$. Ratios smaller than 1 are physically meaningful because the stylus measures the top height, whereas the optical interferences average over the roughness of the film surface. We have no third method to determine the thickness of the films and use the standard deviation of the ratio to check the quality of the fit models.

5.1.2.4 Evaluation of the fit procedure

We tried many models and variants to improve the fit to the experimental spectra. An improvement in the iterative fit procedure is only obtained with good initial values of the parameters. The main features of the spectrum have to be reproduced from the beginning. There is no automatism to get these initial values but some experience and physical intuition are needed.

Generally, the fit becomes better with more fit parameters. One must, however, be careful to assure that these parameters are physically meaningful. A reliable determination of model parameters is only possible if the spectra exhibit model-relevant features. If e.g. the plasma edge lies outside the experimental spectral range, untypical values for the damping constant are obtained and the determination of the position of the plasma edge is unreliable.

5.1.3 Results for SrTiO₃ Films

5.1.3.1 Physical properties of SrTiO₃

Strontium titanate (SrTiO₃) is an insulator. It has cubic perovskite structure at room temperature. SrTiO₃ films are very attractive to be used as insulating films in ultra large-scale integrated (ULSI) circuits, because of its high dielectric constant and small temperature coefficient of capacitance (Nam and Kim 1992; Lesaicherre et al 1995). It can be also used as ferroelectric thin films for microwave tunable devices, such as tunable filters and array radar systems (Hong, Kwak and Kim 2000). Some important physical properties concerning with this work are listed in Table 5-2.

Table 5-2 Physical properties of SrTiO₃ (Bürger 2000)

Density	Lattice constant	Refractive index	Melt temperature
5.12 g/cm ³	0.3905 nm (cubic)	2.41 (at 550 nm)	2100°C

5.1.3.2 Sample preparation

The series SrTiO₃ films under different substrate temperature were prepared by Bürger (2000) in his diploma work. The films have been deposited in a von Ardenne Laboratory System LA 500 S by rf magnetron sputtering from a SrTiO₃ target. The rf power is 500 W (2.83 W/cm²). The quartz substrate temperature was in the range from 400°C to 700°C. The sputtering gas was a mixture of Ar and O₂. The Ar flux was always 15 sccm and the q_{O_2} for each substrate temperature was varied from 0% to 4% systematically. The deposition time was 60 min. leading to about 0.5 μm film thicknesses.

The series SrTiO₃ films under different power were prepared by Gersdorff (1999) in his diploma work. The films have been deposited in a Perkin-Elmer 2400 chamber by rf diode-sputtering. The power was varied from 100 W to 600 W with an interval of 100 W in sequence. The substrate temperature was kept at 400°C. The Ar flux was 15 sccm and the q_{O_2} was always 4% for all samples.

For the more detailed information about the film deposition and characterization, the reader is referred to Ref. (Bürger 2000) and Ref. (Gersdorff 1999).

5.1.3.3 Simulation results

The standard dielectric model for SrTiO₃ films is composed of three terms: a constant and real dielectric background (a unity), an OJL model and a harmonic oscillator which account for the band gap transitions and interband transitions. In order to evaluate and optimizing the standard model, two series STO films mentioned above were simulated.

(1) Samples prepared at different substrate temperature

The samples were first simulated with the standard model. The simulated curves together with the experimental curves and corresponding dielectric function as a function of wavenumber for two representative samples of STO-A and STO-B (named STO-1a 24. 07 and STO-5a 04. 09 in Bürger (2000)) are shown in Figure 5-9 and Figure 5-10, respectively. The main deposition conditions and fitting results are displayed in Table 5-3.

Table 5-3 Fitting parameters for sample STO-A and STO-B simulated with standard and modified (in shadowing) dielectric models

No.	T_s (°C)	OJL (cm ⁻¹)			Harm osc.(cm ⁻¹)			Add. harm osc.(cm ⁻¹)			Thickness (μm)		
		E_0	gamma	mass	Ω_{HO}	α_{HO}	Γ_{HO}	Ω_{HO}	α_{HO}	Γ_{HO}	optical	a-step	Ratio
STO-A	400	28962	1057	1.2	93887	124160	6008				0.3563	0.3712	0.960
STO-B	650	27422	47	2	48327	74144	81				0.3285	0.3597	0.913
		27694	19	1.9	51731	71984	768	11119	1360	2654	0.3653		1.016
		26614			56026	78202	884	11119	1357	2663	0.3649		1.014
		(Tauc band gap)						5217	1089	1310			

STO-A and STO-B were peripheral samples deposited under 400°C and 650°C, respectively ($q_{O_2} = 0\%$). According to the detection of XRD (Bürger 2000), it is known that STO-A is an amorphous film, whereas STO-B is a polycrystalline film. It is observed that the fitting for STO-A is much better than that for STO-B, indicating that the standard model has encountered difficulties to cope with crystalline SrTiO₃ films. Therefore, the standard models must be modified in order to achieve a better fitting for sample STO-B.

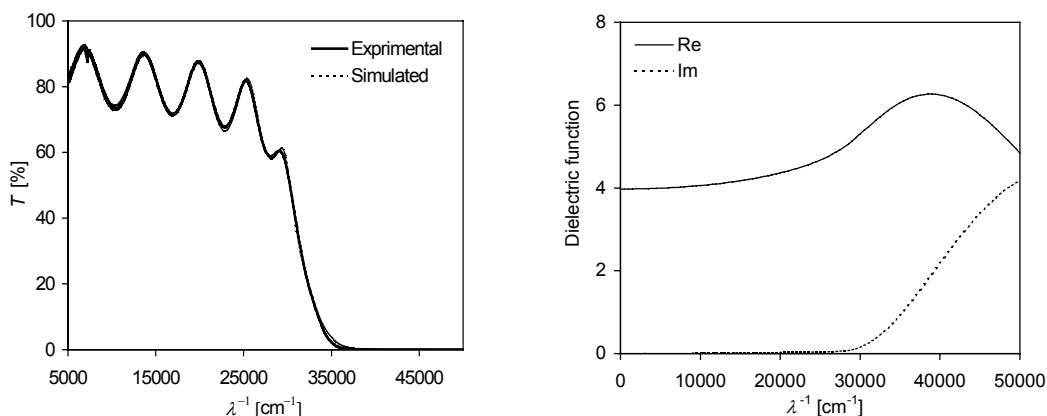


Figure 5-9 Fitting results for STO-A with standard dielectric model

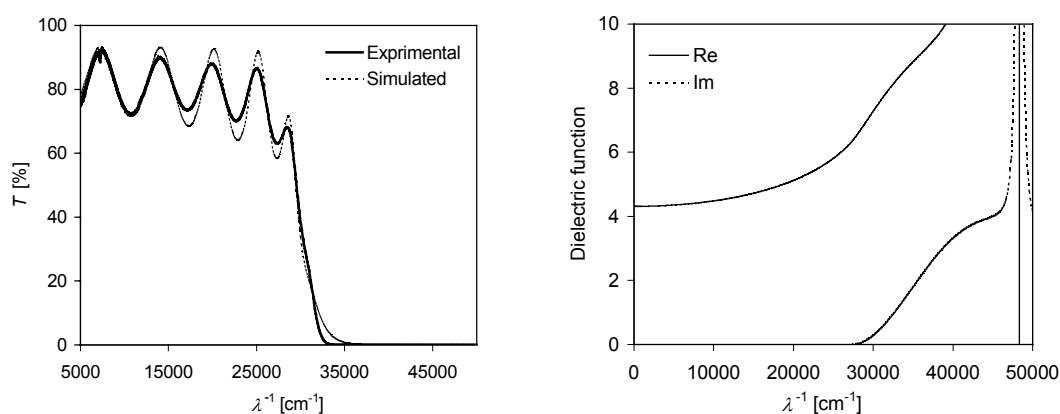


Figure 5-10 Fitting result for STO-B with standard dielectric model

Considering that the OJL model is for amorphous silicon and the treated film STO-B is crystalline, as well as the problem for the fitting close to the band gap is observed, the OJL model is replaced by Tauc-Lorentz model (Jellison 1998) which is characterized by an exactly zero imaginary part of the dielectric function below the band gap, i.e. there is no absorption. The new band transition model has resulted in an improved fitting at the band edge. However, the fitting in the visible and near infrared spectral range is still bad. Therefore, two additional harmonic oscillators were introduced to account for more absorption in these regions. They resonate at 11119 cm^{-1} (900 nm) and 5217 cm^{-1} (1900 nm). From the dielectric function displayed in Figure 5-18 it is observed that the two oscillators introduce two small and broad peaks, i.e. resulting in two absorptions in the spectral range of visible and near infrared. Consequently, the fitting has been improved there. The relevant energies of the two electron transitions are 1.37 eV and 0.64 eV which are far more less than the band gap (3.34 eV). The physical meanings of the additional harmonic oscillators are not quite clear. One possibility is that there are some localized states in the band gap. The film thickness obtained from the modified model is much closer to the stylus thickness comparing with the case of

standard model. The fitting parameters of the improved models for STO-B are listed as well as in Table 5-3 in shadowing.

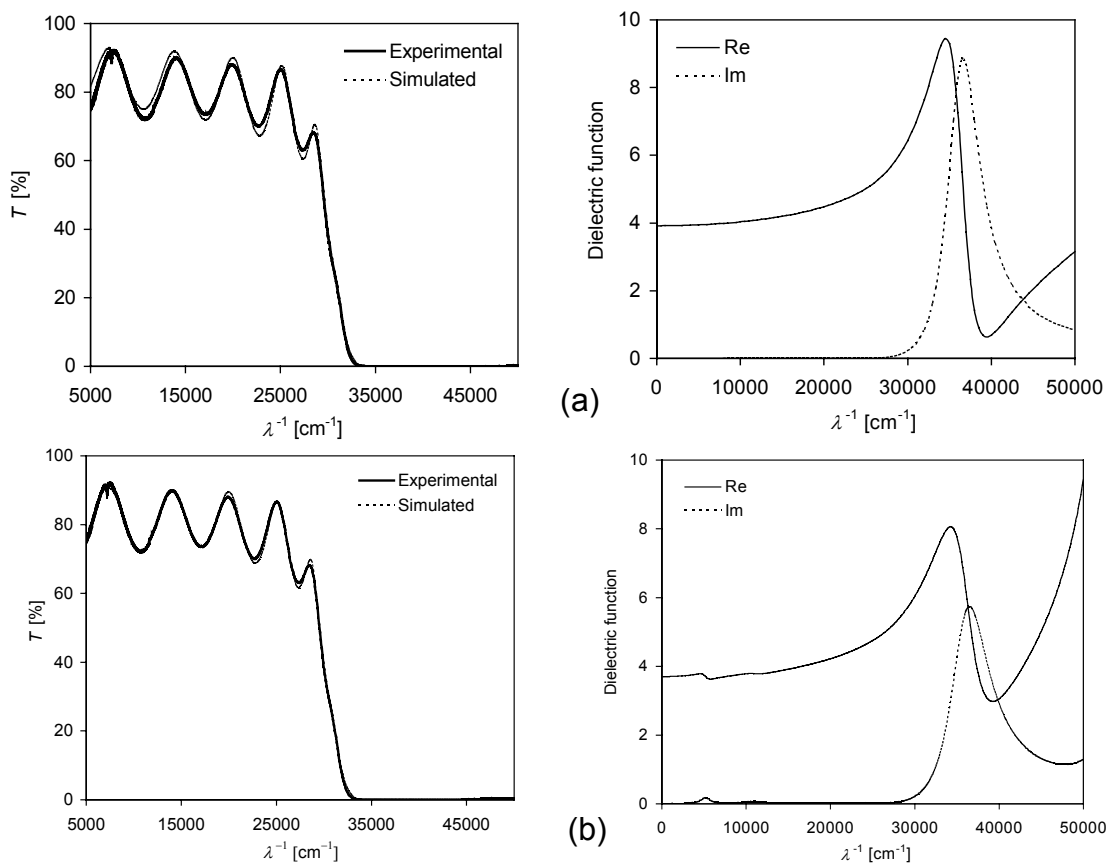


Figure 5-11 Fitting results for STO-B with modified models: (a) Tauc-Lorentz model instead of OJL model, (b) Tauc-Lorentz model, harmonic oscillator and two additional harmonic oscillators

(2) Samples prepared at different power

In order to investigate the effectiveness of the standard dielectric modeling on SrTiO₃ films furtherly, samples sputtered at different rf power and thus existing different extent of crystallinity were simulated. Among these samples, Sr2b and Sr6b were sputtered with 200 W and 600 W rf power, respectively. XRD patterns show that the crystallization of Sr6b is much better than that of Sr2b (Gersdorff 1999). Inversely, the fitting for Sr6b is much worse than that for Sr2b in the case of standard models as shown in Figure 5-12. In order to improve the simulation, an additional harmonic oscillator whose resonance frequency equals 4584 cm $^{-1}$ (2182 nm or 0.57 eV) was added to the standard model. This leads to a significant improvement of the fitting visually.

Table 5-4 Fitting parameters for Sr2b and Sr6b with standard and modified (in shadowing) dielectric model

No.	Power (W)	OJL (cm ⁻¹)			Harm osc.(cm ⁻¹)			Add. harm osc.			Thickness (μm)		
		E0	gamma	mass	Ω_{HO}	O_{HO}	Γ_{HO}	Ω_{HO}	O_{HO}	Γ_{HO}	optical	a-step	Ratio
Sr2b	200	30719	2006	2.3	87108	136905	3812				0.1860	0.170	1.094
Sr6b	600	30005	1766	2.8	87098	111044	3768				0.3195	0.300	1.065
		29646	1617	2.2	89599	106267	7758	4584	1445	2726	0.3494		1.165

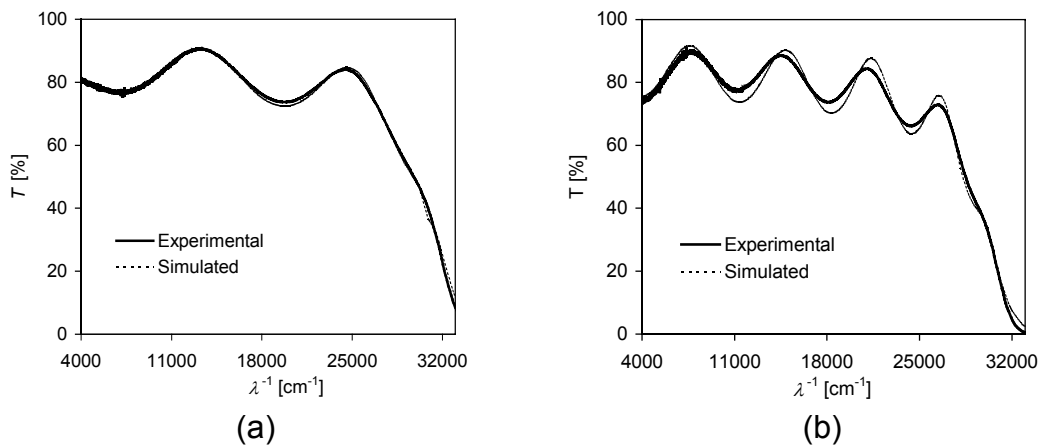


Figure 5-12 Experimental and simulated spectra with standard model for STO films: (a) Sr2b, (b) Sr6b

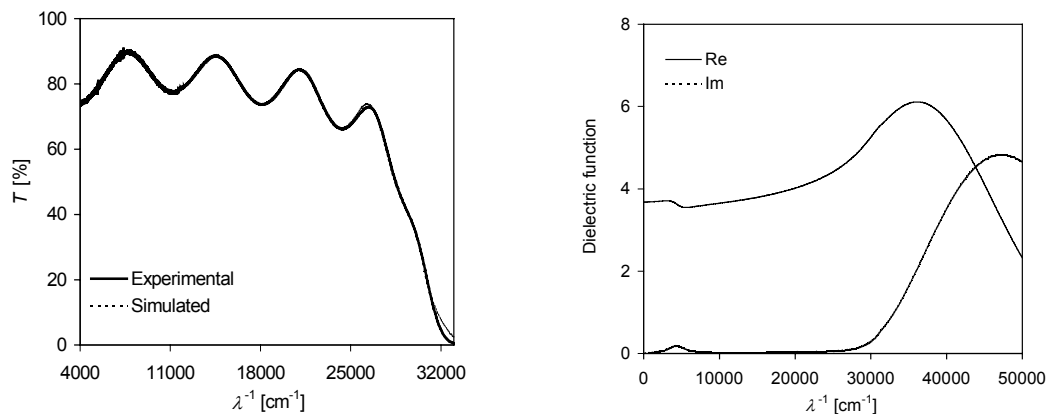


Figure 5-13 Fitting results for Sr6b with improved models (adding an additional harmonic oscillator to the standard model)

It is observed that the optical thickness of modified model is thicker than that of standard model. Moreover, the film thickness derived from the simulation is always larger than that measured by profilometer. This can be explained in terms of the thickness profile of SrTiO₃ films. It has been observed by Bürger (2000) that there was a strong shadowing effect from the substrate holder at the STO films' boundaries. The thickness differences between the center of the substrate and two

edge positions located at 20 nm and 23.5 nm (x-axis) were 13.7 nm and 78 nm, respectively. Since the stylus measurements locate most probably in the range from 20 nm to 23.5 nm, it can be concluded that the modified dielectric model leads to more reliable film thickness.

5.1.3.4 Differences between the amorphous and crystalline SrTiO₃ films

According to above simulation results, it can be concluded that the fitting depends on the extent of crystallinity of the films. For amorphous and low crystallized films, the fittings with the standard model are already quite satisfied. However, for highly crystallized films, the standard dielectric model seems to be too simple and the OJL model does not fit to the band edge.

In order to improve the fitting, one or two additional harmonic oscillators have to be added up to the standard model. The function of them is introducing additional absorption at certain wavelength. Moreover, the OJL model can be replaced by Tauc-Lorentz model, leading to a better fitting in the band edge. Generally, the modified dielectric model can strongly improve the fitting visually and give more reliable film thickness.

In OJL model, the band gap and gamma for crystalline films are smaller than that for amorphous films, indicating there are more tail states in the band gap for amorphous films.

5.1.4 Results for TiO₂ Films

5.1.4.1 Physical properties of TiO₂

The TiO₂ being classified as transition metal oxide is a kind of dielectric. It is known that the valence band is composed mainly of oxygen 2p-like states and the conduction band is made up of titanium 3d-like states. TiO₂ films are widely used in optics because of their high refractive index and their stability (Löbl, Huppertz and Mergel 1994). The films can be prepared by many deposition techniques such as evaporation, various sputtering methods, CVD techniques, etc. It has been observed that TiO₂ films can exist in amorphous state or crystalline phases of anatase and/or rutile. The microstructure and optical properties of TiO₂ films are strongly dependent on the deposition conditions. Generally, films of high density and thus high refractive index are obtained by all methods where the growing film is bombarded with particles of high energy, as is the case for sputtering processes (Löbl, Huppertz and Mergel 1994). And amorphous TiO₂ films are often observed

when the substrate temperature during deposition is low. Some physical properties of TiO₂ are listed in Table 5-5.

Table 5-5 Physical properties of TiO₂ (Mergel et al 2000; Schenkel 1998)

	Rutil	Anatas	Amorphous
Mass density	4.23 g/cm ³	3.84 g/cm ³	3.2 – 3.65 g/cm ³
Refractive index at 550 nm	2.7	2.4	1.9
Band gap	3.6 – 4 eV		

5.1.4.2 Sample preparation

In order to evaluate the dielectric modeling for TiO₂ with different microstructure, the transmittance spectra of TiO₂ films prepared by evaporation and rf sputtering methods were simulated.

The evaporated Titania films were prepared by Jerman (Uni-Essen). The films were deposited by electron beam (EB) evaporation of granular TiO₂ (purity 99.5%) in a BAK640 high vacuum chamber. The base pressure before deposition was 8×10^{-5} mbar. The substrate temperature was 300°C. The oxygen flux was 1.5×10^{-4} mbar. The samples were deposited on normal glass and quartz substrates. All the films were amorphous. The detail description of the experimental setup is referred to as Ref. (Mergel et al 2000a).

The sputtered Titania films were prepared by Schenkel (1999). The films have been deposited in a Perkin-Elmer 2400 chamber by rf diode-sputtering from an 8 inch (20.3 cm) ceramic target. The target-substrate distance was 4.6 cm. The vacuum chamber was pumped down to 1×10^{-5} mbar before deposition. The sample R9 and R1 (named R9 18.05-Nr.2 and R1 09.05-Nr.2 in Schenkel's work) were deposited on BK7 glass and quartz substrates, respectively. The oxygen partial pressure was 5%, and the substrate temperature was 380°C.

5.1.4.3 Simulation results

The standard dielectric model used for TiO₂ is the same as for SrTiO₃, namely, the OJL model and a harmonic oscillator which account for the band gap transitions and interband transitions, respectively.

(1) Evaporated TiO₂ films

Generally, the evaporated amorphous TiO₂ can be fitted very well with the standard model. Even in the band edge, the OJL model also works very well. As

an example, the experimental spectrum of the film TiQ (named tio2-q2 24.1.00 in Jerman's work) deposited on quartz substrate is shown in Figure 5-14 (a), together with its simulated curve derived from the standard model. However, sometimes problems occur in the long wavelength range, i.e. the standard model failed to achieve some absorption there, which is shown in Figure 5-14 (b) for the film TiG (named TiG 04.10.2001 in Jerman's work) deposited on glass substrate. It has been proven that an introducing of a Drude term to the standard dielectric model resulted in a significant improvement (see Figure 5-15). The Drude term is used to account for the transitions of free electrons in the conduction band. Although TiO_2 is an insulator, there will be some free electrons in the conduction band when Ti atoms have not been oxidized stoichiometrically in an oxygen-deficient ambient. Such situation could take place probably for the sample TiG because the oxygen pressure during the evaporation was quite low (1.5×10^{-4} mbar). The fitting parameters for above two samples are listed in Table 5-6.

Table 5-6 Fitting parameters for TiQ and TiG with standard and modified (in shadowing) dielectric model

Sample	OJL (cm^{-1})			Harm osc. (cm^{-1})			Drude (cm^{-1})		Thickness (μm)			n (550nm)
	E_0	gamma	mass	Ω_{HO}	ω_{HO}	Γ_{HO}	Ω_{p}	Γ_{Dr}	optical	a-step	Ratio	
TiQ	26630	538	3.9	73507	91613	813			0.5026	0.489	1.028	2.31
TiG	27137	715	4.4	91515	110836	1360			0.7238	0.739	0.979	2.34
	27233	813	4.1	80152	94078	0.002	3180	86228	0.7406		1.002	2.28

The dielectric functions of standard and improved model for sample TiG are shown in (a) and (b), respectively. In the improved model, the plasma frequency of the Drude term is 3180 cm^{-1} (3145 nm), which indicates a free carrier density of $5.48 \times 10^{19} \text{ cm}^{-3}$. It is also observed that the film thickness derived from the modified model is much closer to the stylus thickness.

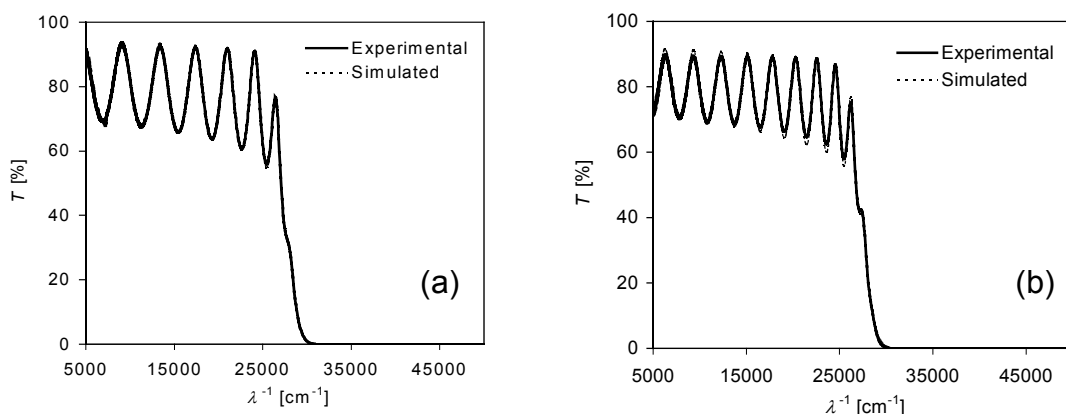


Figure 5-14 Experimental and simulated spectrum with standard models for evaporated TiO_2 film: (a) TiQ, (b) TiG

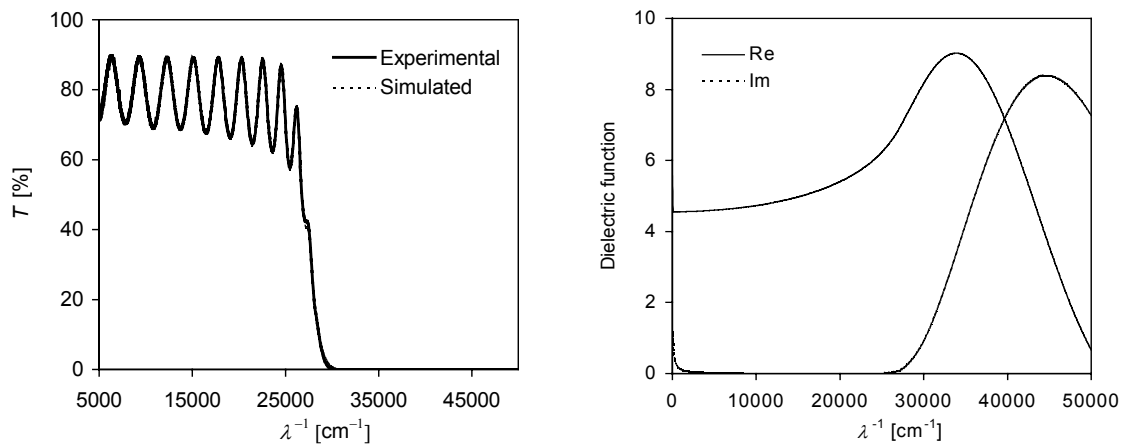


Figure 5-15 Simulation results for TiG with modified model (introducing a Drude term to the standard model)

(b) Sputtered TiO₂ films

The transmittance spectra together with the corresponding simulated curves of two sputtered TiO₂ films R9 and R1 are shown in Figure 5-16. The deposition time of the sample R9 and R1 were 60 and 120 min, respectively, leading to the corresponding thickness of 0.18 μm and 0.34 μm, respectively. According to the XRD measurement, both two samples are polycrystalline films with the phases of anatase and rutile. There are more reflex peaks and the intensity of the peaks is also stronger for sample R1 due to its bigger thickness.

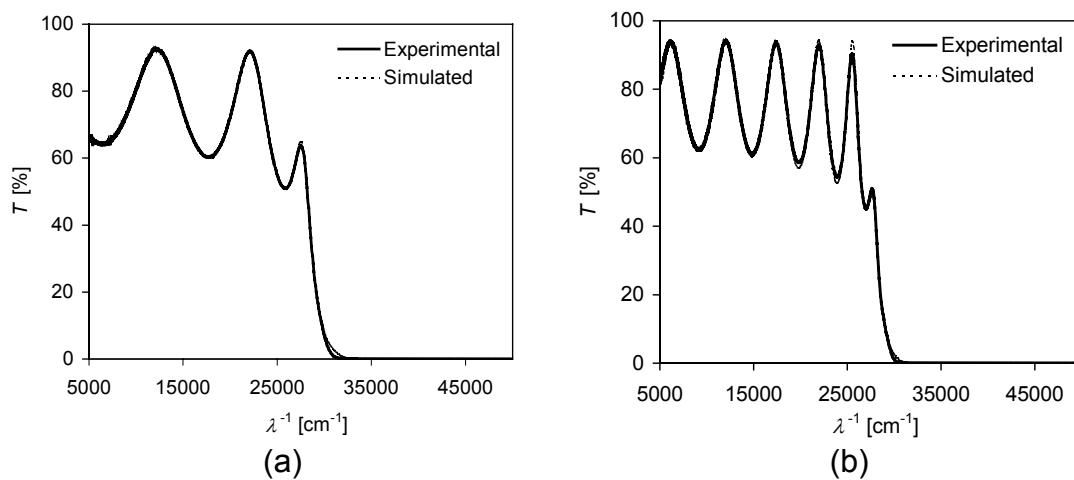


Figure 5-16 Experimental and simulated spectra with standard models for sputtered TiO₂ films: (a) R9, (b) R1

The parameters for the simulations are listed in Table 5-7. It is observed in Figure 5-16 that the fitting of sample R9 is better than that of R1 with standard dielectric model. But the fitting in the band edge is not perfect for both films. This can be improved by using Tauc-Lorentz model instead of the OJL model.

Table 5-7 Fitting parameters for R9 and R1 with standard and modified (in shadowing) dielectric model

No.	OJL (cm ⁻¹)			Harm osc.(cm ⁻¹)			Add. harm osc.			Thickness (μm)			n (550nm)
	E ₀	gama	mass	Ω _{HO}	O _{HO}	Γ _{HO}	Ω _{HO}	O _{HO}	Γ _{HO}	optical	a-step	Ratio	
R9	26548	24	8.3	81482	111378	3.2				0.1673	0.178	0.940	2.55
	26525	28	6.4	102795	115538	119				0.3438		1.011	2.53
R1	26556	31	6.4	93417	97847	1543	8596	881	2079	0.3493	0.340	1.027	2.49

5.1.4.4 Differences between the amorphous and crystalline TiO₂ films

By comparison of the simulation results of sputtered and evaporated films with standard model, it can be concluded that the crystalline films and amorphous films have a similar band gap but the former one has a much small gamma indicating that there are almost no tail localized states in the band gap. The OJL model works very well for amorphous films, while for crystalline films the Tauc-Lorentz model is better.

It is the same as STO that the modified dielectric model leads to more reliable film thickness.

The biggest band gap derived from the simulation is about 3.4 eV, approaching to the lower limitation of the band gap of 3.6 eV in the literature. The refractive index of the polycrystalline films at 550 nm fits the average value of anatase and rutile listed in Table 5-5 very well.

5.2 DC Magnetron Sputtered ITO Films

5.2.1 Effect of Lattice Distortion on the Properties of ITO Films

In this section, the films grown at substrate temperature between 140°C and 400°C, various oxygen partial pressures and two sputter geometries are investigated. The aim of the study is to correlate the structural (lattice distortion, grain size), optical (refractive index) and electric (electron density and mobility) parameters.

5.2.1.1 Experimental results

The lattice distortion $\Delta d/d_0$ for all investigated samples is displayed in Figure 5-17. The values are homogeneously distributed in the range from 0 to 2%. The (543)-orientation exhibits negative values of $\Delta d/d_0 = -0.4$ to -0.2% . The lattice expansion decreases with increasing temperature and is stronger for the samples in peripheral position, consistent with our other results (see Section 5.2.2). The distortion of $\langle 100 \rangle$ -oriented grains, obtained from the (400)-peak, is always the smallest. At low temperature, $\Delta d/d_0$ is higher for the higher q_{O_2} .

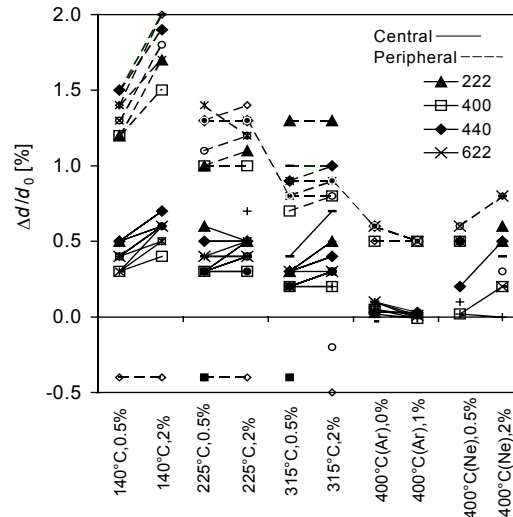


Figure 5-17 Lattice distortion $\Delta d/d_0$ for the various deposition parameters. Different symbols correspond to different XRD peaks

The grain size derived from the XRD measurement by means of Scherrer formula is more precisely the coherence length for x-ray diffraction perpendicular to the film plane, and called “vertical grain diameter D_g ” in this work. This quantity, averaged over all crystalline orientations, is plotted in Figure 5-18 against $\Delta d/d_0$. It

ranges from 15 to 55 nm for the central and from 5 to 35 nm for the peripheral films and is the maximum for films sputtered at 400 °C in Ar. The films sputtered with Ne at the same substrate temperature exhibit grains of only half that size. The effect of more oxygen admixture to the sputter gas is not unique: grains become generally smaller, but for peripheral samples which are at 400°C, sometimes the opposite is observed. Analyzing the data in more detail shows that the grain size depends on the crystalline orientation: grains with orientation (211), (400), or (411) are always largest.

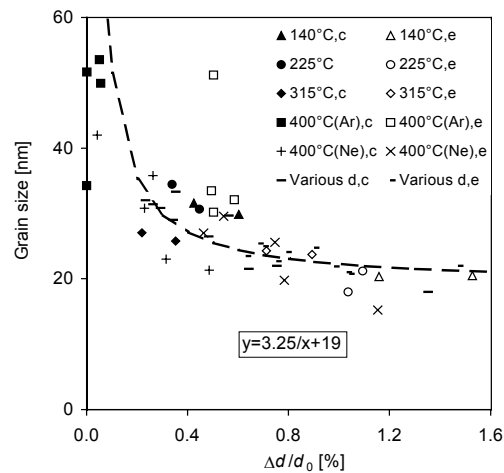


Figure 5-18 Grain size D_g (“vertical grain diameter”) against $\Delta d/d_0$

The transmittance and reflectance curves of two films are shown in Figure 5-19 together with the simulated curves. The simulated curves are shown as grey line inside the recorded spectra, because the calculated curve matches the experimental one. Differences in the position of the band gap ($\lambda = 310$ and 330 nm) and the plasma edge (1200 and 1500 nm, respectively) are evident. It is also clearly seen that the steepness of the plasma edge, controlled by the damping constant in the Drude formula, is different.

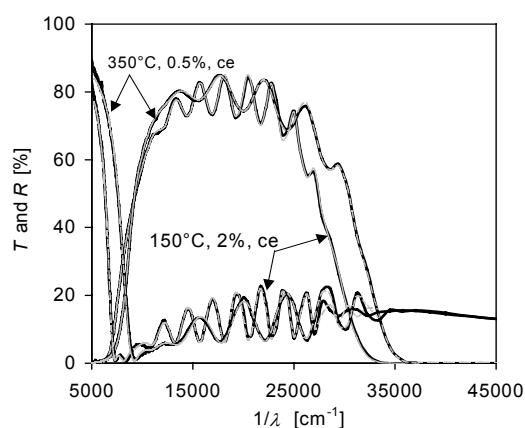


Figure 5-19 Transmittance and reflectance of ITO films together with their simulation curves (the white lines)

The evaluation of the plasma edge by means of the Drude theory yields the carrier density N_{Dr} and mobility M_{Dr} as shown in section 5.1.1.2.

For these sets of samples, the free carrier density N_{Dr} increases with increasing temperature and is lower for the higher q_{O_2} (see Figure 5-20 (a)). These effects are well known in the literatures and attributed to various degrees of incorporation of interstitial oxygen (Mergel et al 2000). Interstitial oxygen, O_i , captures electrons and can form neutral defect complexes with Sn ion (Frank and Köstlin 1982). N_{Dr} is shown in Figure 5-20 (b) as a function of $\Delta d/d_0$. The straight line represents the relationship:

$$\frac{N_{Dr}}{[cm^{-3}]} = 1.5 \times 10^{21} - 10^{21} \frac{\Delta d / d_0}{1\%} \quad (5.2.1)$$

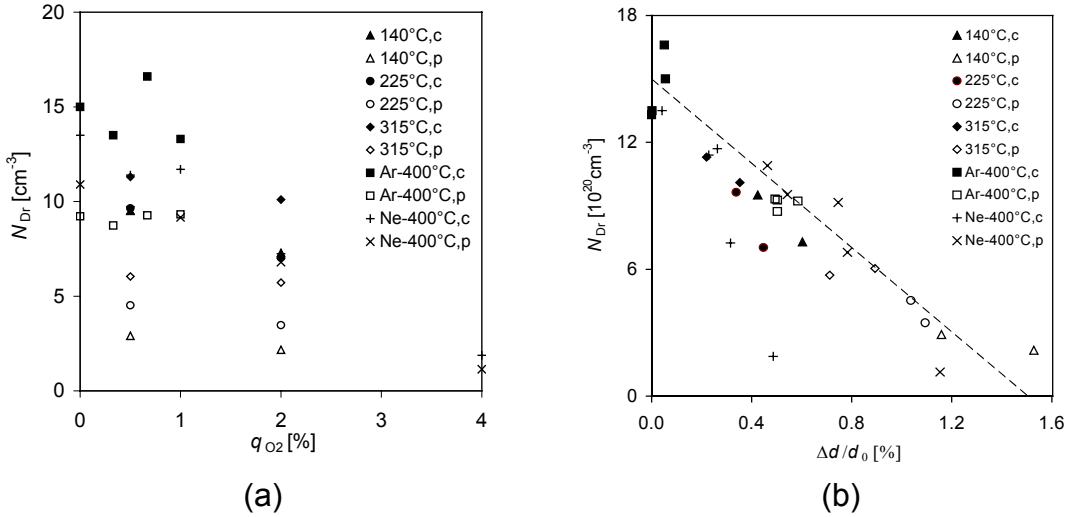


Figure 5-20 Electron density N_{Dr} , evaluated from the plasma edge, against (a) q_{O_2} (b) $\Delta d/d_0$

The mobility M_{Dr} is expected to decrease with increasing free carrier density N_{Dr} as shown by the dash line in Figure 5-21 (a) when scattering at ionized donors is the main friction mechanism and the free electron density is equal to the concentration of ionized donors (Mergel et al 2001; Bellingham, Philips and Adkins 1992). For these sample series, the experimentally observed trend is opposite to the theory (see Figure 5-21). Therefore, scattering at other defects, probably interstitial oxygen, must also play an important role. In order to discuss this point later in more detail, the data are represented as well as in Figure 5-21 (b) as a plot of the reciprocal value of M_{Dr} against $\Delta d/d_0$, consistent with Mathiessen's rule of additive resistivities.

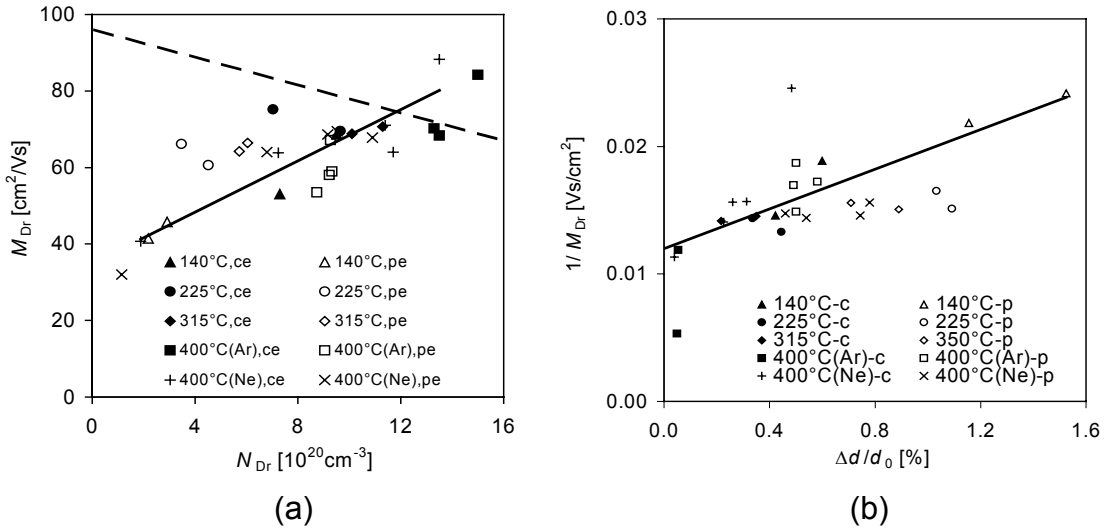


Figure 5-21 Electron mobility and its reciprocal ($1/M_{Dr}$), as evaluated from the plasma edge, against (a) N_{Dr} and (b) $\Delta d/d_0$

The optical transmittance T at 550 nm, obtained by interpolation between interference maxima, is plotted in Figure 5-22 as a function of the carrier density N_{Dr} . With increasing N_{Dr} , T initially remains constant at about 90%, decreases to 80% for $N_{Dr} = 10^{21} \text{cm}^{-3}$ and then drops rapidly to 55% for $N_{Dr} = 1.5 \times 10^{21} \text{cm}^{-3}$. The absorption coefficient of the samples is described by:

$$\frac{a}{[\mu\text{m}^{-1}]} = 0.115 \frac{N_{Dr}}{[10^{21} \text{cm}^{-3}]} + 0.028 \quad (5.2.2)$$

The reliability of the fit is $r^2 = 0.61$. The scatter of the data looks similar to that in Figure 5-20.

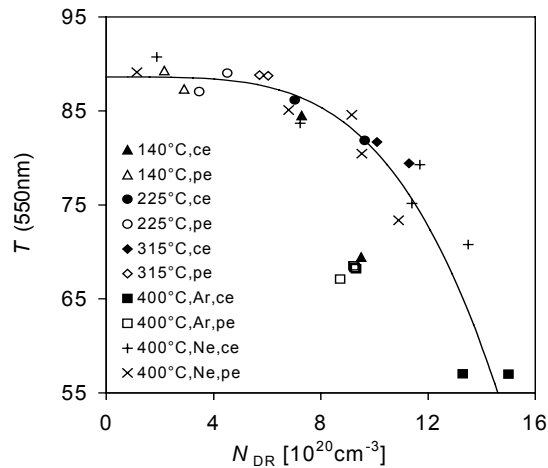


Figure 5-22 Optical transmittance ($\lambda = 550 \text{ nm}$) against the electron density N_{Dr} . The curve serves as a guide to the eye

The surface roughness of the ITO films derived from the AFM measurement by means of root mean square (rms) as a function of lattice distortion is displayed in

Figure 5-23. It is observed that the surface roughness decreases with increasing lattice distortion. It has known from the former result that the grain size decreases with increasing lattice distortion. Hence it is concluded obviously that the surface roughness increasing with the grain size.

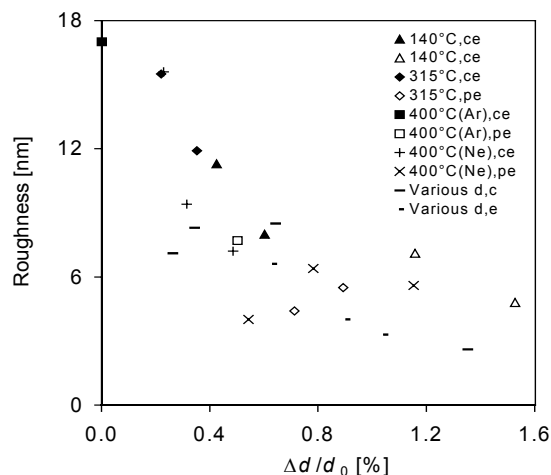


Figure 5-23 Surface roughness derived from the AFM measurement against $\Delta d/d_0$

5.2.1.2 Discussion

(1) Oxygen content

In heavily doped ITO, the carrier concentration is determined by the concentration of the donor tin and of interstitial oxygen that acts as an electron acceptor and thus compensates for the donor action of the tin atoms. Defect complexes such as $(\text{Sn}_2^*\text{O}_i^-)$ are formed (Frank and Köstlin 1982). The lattice distortion is a measure of the concentration of interstitial atoms, mainly oxygen. This explains the linear relationship between lattice distortion and carrier concentration, Figure 5-20 (b). Assuming that every O_i captures two electrons, Eq. (5.2.3) gives a linear relationship between the concentration of interstitial oxygen $[\text{O}_i]$ and the lattice distortion ($\Delta d/d_0$):

$$[\text{O}_i] = 0.5 \times 10^{21} \text{ cm}^{-3} \frac{(\Delta d / d_0)}{1\%} \quad (5.2.3)$$

(2) Electrical conductivity

The optically determined electrical conductivity σ_{Dr} ($\sigma_{\text{Dr}} = N_{\text{Dr}} e M_{\text{Dr}}$) is compared in Figure 5-24 with the direct current conductivity σ_{dc} determined with a four-point probe. All data points lie above the line for $\sigma_{\text{Dr}} = \sigma_{\text{dc}}$. This is in agreement with previous results where the parameters resulting from the optical were compared with those from Hall Effect and conductivity measurements (Mergel and Qiao

2002): both the “optical” mobility and carrier density were found to be higher than the respective electrical parameters. These discrepancies were attributed to a pronounced microstructure with badly conducting grain boundaries that reduces the direct current conductivity but does not hamper the oscillatory motion of the optically excited carriers.

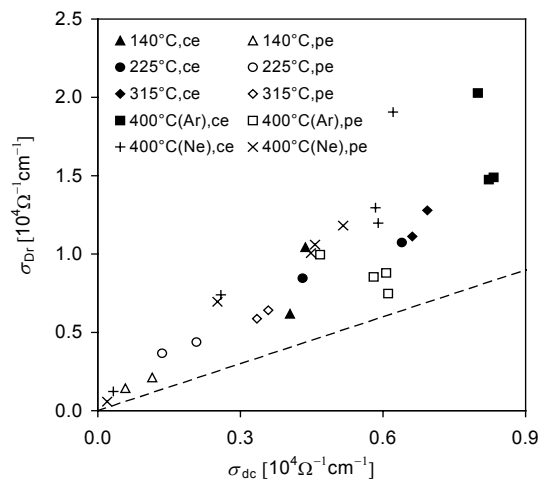


Figure 5-24 Conductivity σ_{Dr} , as calculated from N_{Dr} and M_{Dr} , against direct current conductivity σ_{dc}

Evaporated films with an average strain of 0.4% exhibit a higher resistivity ($200 \mu\Omega\text{cm}$) than films with more strain (0.85%) prepared by evaporation using an arc plasma generator ($135 \mu\Omega\text{cm}$) (Shigesato, Takaki and Haranoh 1992). Consistent with the arguments presented above, this may be explained by the generally more pronounced columnar microstructure of evaporated films.

The electron mobility within a grain is determined by scattering at grain boundaries, ionized donors, and defects related to interstitial oxygen. Grain boundary scattering is not relevant for these sample series because there is no correlation between the mobility and the grain size. A linear fit for these two parameters yields a reliability coefficient $r^2 = 0.00$. Scattering at ionized donors is not the only friction mechanism active in these sample series because the theoretical trend does not fit the experimental data. Therefore, the hypothesis that scattering takes place at ionized donors and at interstitial oxygen is examined. In agreement with Mathiessen’s rule, a linear fit to $1/M_{Dr} = f(\Delta d/d_0)$ is tried and got in Figure 5-21, with a reliability $r^2 = 0.58$:

$$\frac{1}{M_{Dr}} \left[\frac{Vs}{\text{cm}^2} \right] = 0.0056 \frac{\Delta d}{d_0} [\%] + 0.0125 \quad (5.2.4)$$

The intercept corresponds to the scattering at ionized donors with a density of $1.5 \times 10^{21} \text{ cm}^{-3}$ ($M_{Dr} = 80 \text{ cm}^3/Vs$). The increase with $(\Delta d/d_0)$ describes the effect of

the transformation of ionized donors into the neutral defect complex Sn^*O_i due to oxygen incorporation.

In the literatures, a low resistivity was related to: (i) optimal substrate or annealing temperature (Joshi, Singh and McClure 1995), (ii) optimal oxygen partial pressure (Fan, Bachner and Foley 1977), (iii) low sputter voltage (Shigesato, Takaki and Haranoh 1992), (iv) big grain size (Higuchi et al 1993), (v) big ratio of x-ray diffraction intensities, $I(222)/I(400)$ (Meng and dos Santos 1996).

We suggest relating all effects to the density of interstitial oxygen. The first two effects can be attributed to better film growth yielding stoichiometric ITO with high electron concentration and mobility. A low sputter voltage leads to less oxygen implantation. The fourth effect was attributed to less scattering at grain boundaries. On the basis of our results, this mechanism can be ruled out. The effect may be related to the concentration of oxygen interstitials that is inversely correlated with the grain size or may be due to a microstructure with badly conducting grain boundaries. The increase of the intensity of the (222)-reflex, effect (v), was obtained by annealing the films. The related decrease in resistivity is probably due to a decrease in the concentration of the oxygen surplus in the lattice.

(3) Grain size and statistic lattice distortion (inhomogeneous microstrain)

The vertical grain size generally decreases with increasing lattice distortion and seems not to be influenced directly by the growth temperature. This indicates that the formation of grain boundaries is driven by the stress in the films and is not just a consequence of the superstoichiometric concentration of interstitial oxygen as supposed earlier (Mergel et al 2001).

Sputtered ITO films often exhibit a domain-subgrain structure where all subgrains in a domain (of about 500 nm diam) have the same crystallographic orientation (Kamei, Shigesato and Takaki 1995). The altitude of the domains depends on the orientation of their subgrains: for (400) it is bigger than for (222) which was explained by orientation dependent resputtering. In previous work, we observed the (400)-grains exhibit less lattice distortion than (222)-grains in the same film and concluded that the (400)-surface is more resistant against implantation (Mergel et al 2001). In this work, we observed that, for the same lattice distortion, (400)-grains are larger than (222)-grains, or more precisely formulated, the coherence length perpendicular to the surface, as calculated from the Scherrer formula, is bigger. This point needs further investigation.

So far, we have always correlated the width of a diffraction peak to the mean grain size D_g perpendicular to the film surface by means of Scherrer formula as

mentioned in section 4.4.1. However, according to Segmüller and Murakami (Klabunde 1985) and Mader (1970), imperfections of the crystal structure, such as microstrains (nonuniform strains), will cause an additional broadening of the linewidth. The line broadenings $\Delta(2\theta)$ due to the crystalline size C and microstrains (inhomogeneous strains) $\varepsilon = \Delta d/d$ are given by (Mader 1970):

$$\Delta(2\theta) = \frac{K\lambda}{C \cos(\theta)} \quad (5.2.5)$$

$$\Delta(2\theta) = 2 \tan(\theta)\varepsilon \quad (5.2.6)$$

where K , λ and θ have the same meanings as in Eq. (4.4.4). According to Segmüller and Murakami, it is possible to judge where the broadening comes from: if the values of C , measured for two or more orders of one reflection along the same direction of the film, agree reasonably well, the finite grain size is indicated as primary cause of the line broadening; otherwise, the presence of microstrains is strongly indicated.

In order to investigate if there also exist microstrains in our films, the linewidth of some samples which possess two orders for the same reflex, such as 200 – 400, 222 – 444 and 211 – 422, is plotted against $\tan\theta$ in Figure 5-25. As it is shown, there exists a clear linear function between these two quantities just as expected by Eq. (5.2.6). This indicates that the line broadening comes from the microstrains in the films. And the slope of the trendline should represent the microstrain.

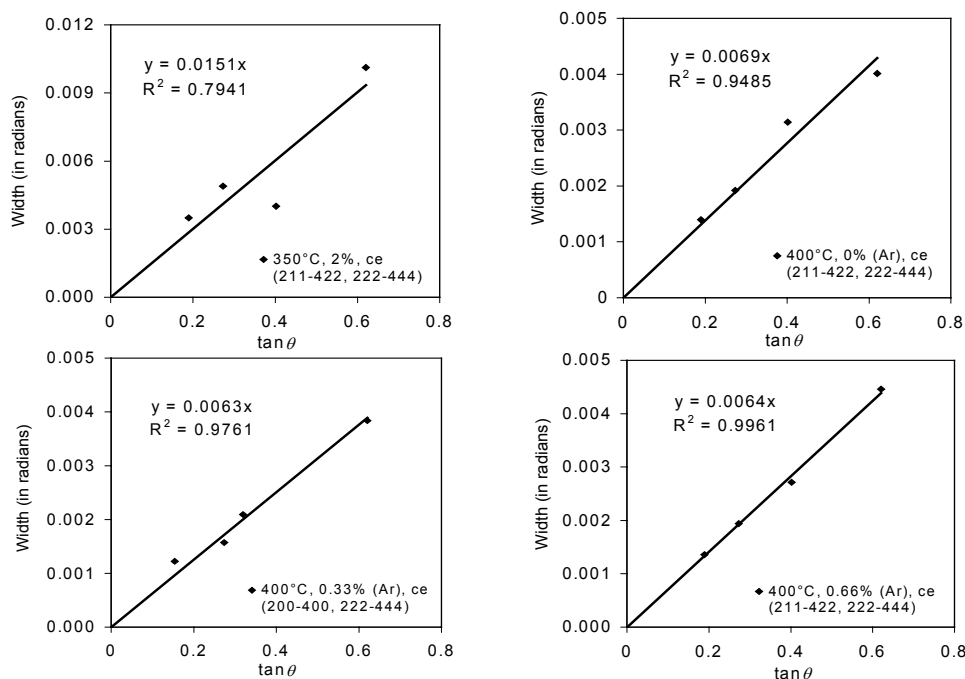


Figure 5-25 XRD peak width against the corresponding reflex tangent angle (the orientation is shown in brackets)

In Figure 5-26, the microstrains against the lattice distortion (also called macrostrain or homogeneous strains) is plotted in order to investigate the correlation between them. It is observed that the microstrain increases with average lattice distortion increasing. This is physically reasonable because the larger the lattice distortion, the more oxygen interstitials incorporated into the crystal lattice, while the rms microstrains, which stand for the statistical fluctuation of the distance of the Bragg planes, are possible more larger. And there still exist a certain microstrains even when the average lattice distortion is nearly zero.

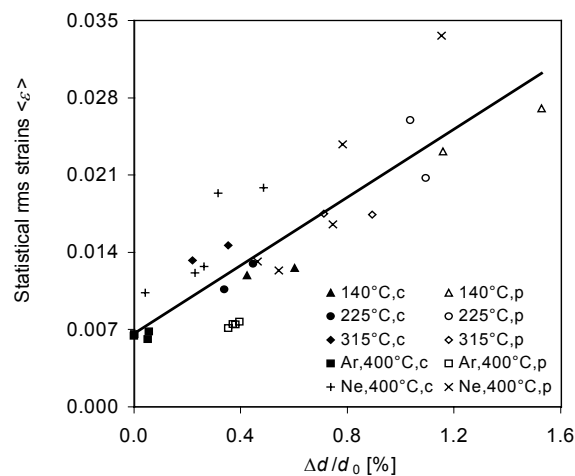


Figure 5-26 Statistical rms strains against average lattice distortion

Eq. (5.2.5) and Eq. (5.2.6) can be used to evaluate the effects of grain size and inhomogeneous strains, respectively, if they occur separately. However, in a real material, there are simultaneous contributions to the line width from both sources as well as from lattice defects, and they superimpose in a complicated fashion (Mader 1970). Therefore it is difficult to distinguish these two sources.

Vook and Witt (1965) determined effective grain size and microstrains in a less rigorous approximation by measuring half widths of line profiles directly. The observed broadening $\Delta(2\theta)$ was treated as a sum of Eq. (5.2.5) and (5.2.6). A plot of $\Delta(2\theta)$ vs. $\sin\theta$ for several reflections gave the effective grain size from the intercept at $\sin\theta = 0$ and the average nonuniform strain from the slope. This method is also used for the four samples in Figure 5-25 and the results are shown in Figure 5-27. It is observed that the trend line slopes which stand for the average inhomogeneous microstrains are comparable to that derived in Figure 5-25. The intercepts are nearly zero for all these four samples. This indicates that it is the microstrains that give rise to the line broadening in these samples.

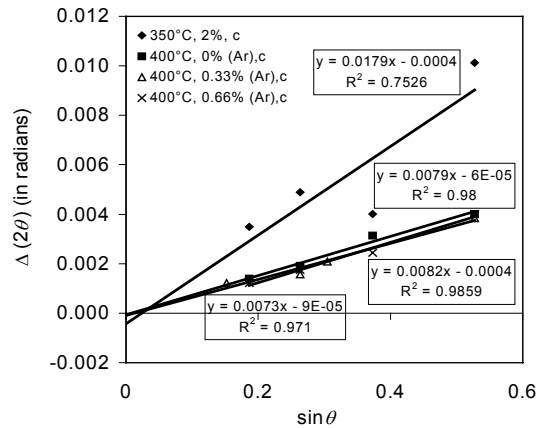


Figure 5-27 Line width as a function of $\sin\theta$

(4) Refractive index

In Figure 5-28, the refractive index n at 550 nm is plotted against N_{Dr} . The trend, represented by the straight line, is given by ($r^2 = 0.50$):

$$n(550\text{nm}) = 2.10 - 0.24 \times 10^{-21} [\text{cm}^3] N_{Dr} \quad (5.2.7)$$

This corresponds to the relationship found for radio-frequency sputtered ITO films, where, however, an initial value of 2.17 instead of 2.10 fitted the experimental data best (Mergel and Qiao 2002). The decrease in $n(550\text{nm})$ with increasing electron concentration is due to both the Burstein-Moss shift of the band gap to higher energies, away from 550 nm, and the shift of the plasma edge to higher energies, towards 550 nm.

A shift of the absorption edge and a decrease in the refractive index upon annealing was reported and interpreted as a direct effect of the relaxation of the lattice constant (Dietrich et al 1984). We suggest as an alternative explanation that the primary effect is the reduction in the concentration of interstitials leading to both the lattice relaxation and in the refractive index due to an increase in the electron density.

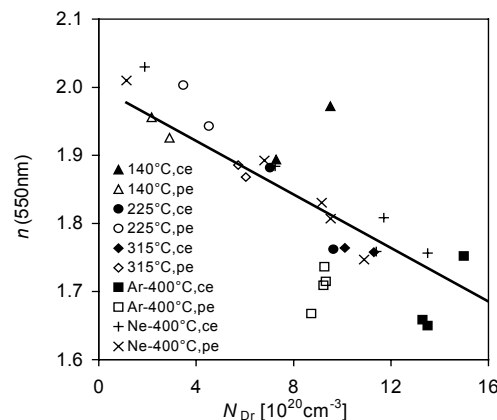


Figure 5-28 Refractive index (550 nm) as a function of N_{Dr}

5.2.2 Effect of Sputter Geometry and Plasma Distribution on the Structural and Electrical Properties of ITO Films

In this section, the effects of the lateral position of the substrate relative to the target center and the distribution of dc plasma on the structural and electrical properties of ITO films deposited at various oxygen partial pressures are investigated. In order to produce ITO films by sputtering for a wide variety of applications we try to control the film density by varying the process parameters. The results are discussed on the basis of oxygen incorporation into the crystal lattice of the bixbyite structure resulting from the direct effect of plasma and columnar structure.

5.2.2.1 Experimental details

In fact, all magnetron targets are inherently nonuniform sources. The planar magnetron behaves essentially as a ring source owing to the shape of the confined plasma (Klabunde 1985), which causes an eroded region on the target. The schematic diagram of the sputter geometry is displayed in Figure 5-29 (to scale). The target-substrate distance is 5 cm. Two quartz substrates in 25 mm diameter were mounted centrally and peripherally on a table (diameter 30 cm) above the cathode. And the peripheral one is just above the erosion track on the target (plasma region). The difference of the substrate temperature between the central and peripheral samples is about 50°C (see section 3.3).

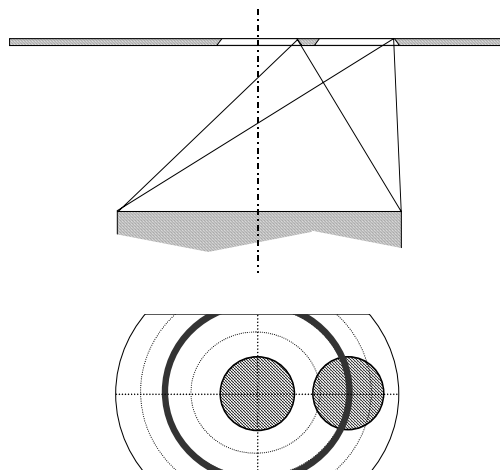


Figure 5-29 Sketch of the deposition geometry (to scale). Top: cross section; Bottom: top view (concentric rings indicate the sputter symmetry, the thick ring denotes the race track)

The vacuum chamber was pumped down to $\sim 10^{-5}$ mbar before deposition. The oxygen partial pressure, p_{O_2} , was varied systematically. The deposition series

were sequenced from the lowest to higher oxygen pressure. The main deposition conditions are listed in Table 5-8.

Table 5-8 The main deposition conditions

Deposition Parameter	Ar sputtered	Ne sputtered
Sputter power (W)	200	200
Sputt. gas flux (sccm)	15	30
Sputter press. (mbar)	6.3×10^{-3}	1.2×10^{-2}
Substrate temp. ($^{\circ}\text{C}$)	400	400
q_{O_2} (%)	0 ~ 4	0 ~ 4
Discharge volt. (V)	341 ($q_{\text{O}_2} = 4\%$)	318 ($q_{\text{O}_2} = 4\%$)
Depos. rate (nm/s)	2.25 (central, $q_{\text{O}_2} = 4\%$)	1.35 (central, $q_{\text{O}_2} = 4\%$)

5.2.2.2 Experimental results and direct conclusions

(1) Thickness profiles

Profiles for centrally and peripherally positioned samples are shown in Figure 5-30. For the sample in central position, the film thickness is constant over the diameter, except for a certain rounding at the boundaries due to shadowing effects from the blind. For the peripheral sample, located 32.5 mm off the target center, the thickness is constant up to 4 mm and then decreases linearly, by up to ~30%. The thickness for the peripheral sample is measured at the position 21 mm (x-axis in Figure 5-30). The effective film thickness is calculated from the profile assuming that the film thickness is the same in concentric rings around the target center (see Figure 5-29). Values of the film thickness range from $0.77 \mu\text{m}$ (peripheral sample, $q_{\text{O}_2} = 4\%$) to $2.6 \mu\text{m}$ (central sample, $q_{\text{O}_2} = 1\%$).

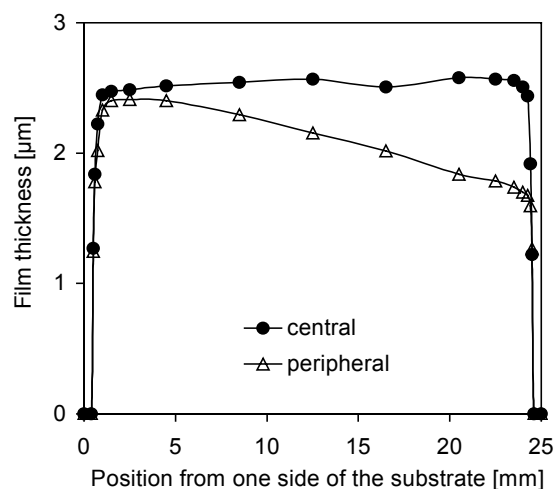


Figure 5-30 Thickness profiles of a centrally and a peripherally positioned film

For every sample of the deposition series, the film thickness in the center and at the edge of the film is determined. D_{stylus} is determined on a mark at the edge by profilometry. D_{opt} is obtained from evaluating optical transmittance spectra by means of dielectric modeling (Mergel and Qiao 2002).

The profiles are independent of the various sputter conditions. This is proven by the ratio of the optically determined thickness in the center of the sample and the thickness at the sample edge obtained from profilometry. This ratio is independent of the sputter conditions. Therefore, the profilometry thickness can be extrapolated to the center. Ratio $d_{\text{opt}}/d_{\text{stylus}} = 1.08 \pm 0.02$ and 1.0 ± 0.05 were obtained for the peripheral samples sputtered with Ar and Ne, respectively. The values for the central samples are 1.0 ± 0.05 (Ar) and 1.025 ± 0.015 (Ne). The standard deviation is in every case less than 5%.

(2) Deposition rate and packing density

The deposition rate is usually given in units of nm/s. We use the mass of the films instead because the thickness of the peripheral films varies over the diameter. In order to get the usual physical units we calculate a mass equivalent rate r_d . From the mass m per area A and time t , a mass equivalent deposition rate r_d [$\text{g}\cdot\text{cm}^{-2}\cdot\text{s}^{-1}$] is calculated by means of the crystalline density, $\rho_c = 7.12 \text{ g/cm}^3$:

$$r_d = \frac{m}{A \cdot t \cdot \rho_c} \quad (5.2.8)$$

The results are shown in Figure 5-31. The deposition rate is lower for the peripheral sample as to be expected from the profile. It decreases with increasing oxygen flux. This is often observed (Rohde et al 1997; Buchanan, Webb, and Williams 1981) and can be explained by increasing target oxidation.

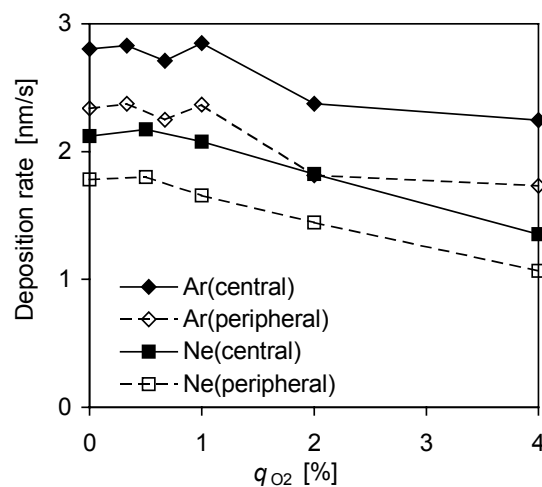


Figure 5-31 Deposition rate, defined as mass equivalent thickness d_m , as a function of the oxygen partial pressure q_{O_2}

It is also shown that the deposition rate for samples sputtered with Ne is less than that sputtered with Ar. This could be attributed to the smaller discharge voltage for sputtering with Ne (see Table 5-8) but mainly to the smaller atomic mass of Ne compared with Ar leading to lower sputter efficiency (see section 2.5.4.1).

The packing density ρ_p of the samples was determined from the mass per area and the film thickness. The results are displayed in Figure 5-32. A strong effect of the sputter geometry is observed. The density of the central samples increases with increasing q_{O_2} and comes close to the crystalline value for $q_{O_2} \geq 1\%$. Contrary, the density of the peripheral samples decreases by more than 10% in the both cases of sputtering with Ar and Ne. The error bars in Figure 5-32 show the 3% statistical error of the packing density which is resulted from the determination of the film thickness according to Mergel et al (2000a).

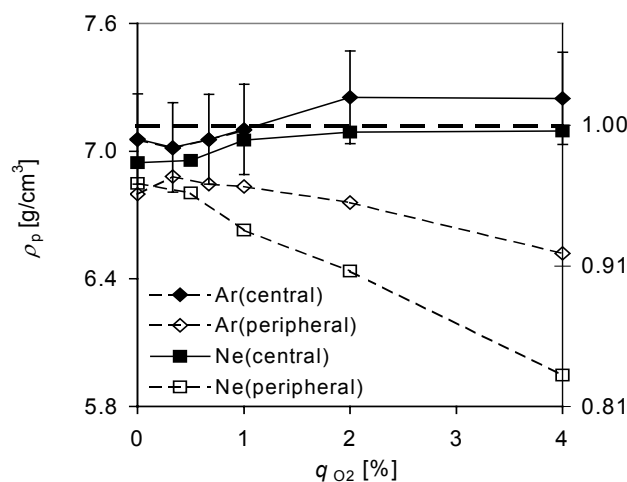


Figure 5-32 Packing density ρ_p of the films as a function of the oxygen admixture q_{O_2} to the sputter gas

(3) Microstructure

X-ray spectrograms of films sputtered with Ar are shown in Figure 5-33. The films sputtered with Ar at $q_{O_2} = 0\%$ exhibit very low crystallinity (see Figure 5-33). A small admixture of oxygen to the sputter gas is necessary to assure films of good crystalline quality. The texture of the peripheral samples differs from that of the central samples: grains with (222)-orientation are absent or very small and broad and the (622) peak is more pronounced. Corresponding spectra of Ne-sputtered films are displayed in Figure 5-34. At $q_{O_2} = 0\%$, the (222) peak is missing in the peripheral samples, similar to the samples sputtered with Ar. The (400) peak is prominent at low q_{O_2} but disappears for $q_{O_2} > 1\%$. Broad (222) peaks dominate for higher q_{O_2} . A shift from (400) to (222) with increasing oxygen admixture to the sputter gas has also been reported in the literatures (Tominaga et al 1996; Choi et al 1995).

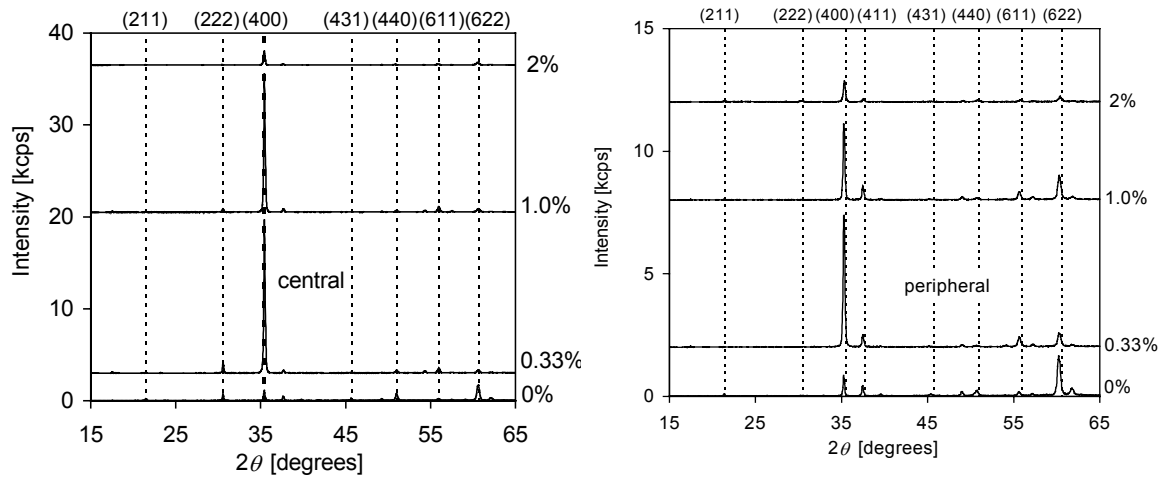


Figure 5-33 XRD patterns for films sputtered with Ar

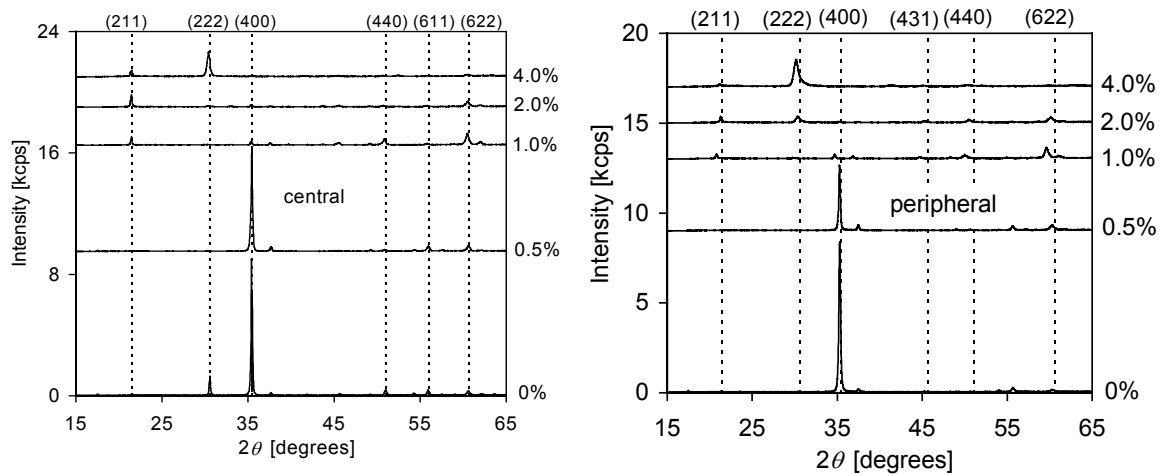


Figure 5-34 XRD patterns for films sputtered with Ne

The diffraction peaks are not always exactly at the positions of ideal crystals indicating lattice distortions. This effect is more pronounced for the peripheral samples. The main findings concerning the lattice distortion $\Delta d/d_0$ are summarized in Table 5-9. The lattice distortion $\Delta d/d_0$ is smaller than for rf diodes sputtered samples whose values up to 3.5% were observed (Mergel et al 2000) and whose values were still between 0.9 and 1.6% for an optimized process (Mergel et al 2001).

Table 5-9 Lattice distortion, at $q_{O_2} = 1$ if not stated otherwise

Orientation	Ar, central ($q_{O_2}=0$)	Ar, peripheral	Ne, central	Ne, peripheral
(222)	-0.002	0.8 (at 0.66)	0.5	0.6
(400)	-0.01%	0.5%	0.2%	0.7%
(440)	0.03%	0.5%	0.4%	0.5% (at 0.5%)
(622)	0.01%	0.5%	0.2% (at 2%)	0.7%

The lattice expansion increases with increasing q_{O_2} , see Figure 5-35. A possible reason is the incorporation of superstoichiometric oxygen in constitutional vacancies of the bixbyite lattice (Mergel et al 2000). The deposition rate decreases with increasing q_{O_2} so that the oxygen flux to the growing film becomes relatively bigger. The distortion is biggest for (440) and smallest for (400) and (622). In rf sputtered films, the lowest values were also observed for (400) and (622) (Mergel et al 2000). The lattice distortion for the peripheral samples is always bigger (0.4% to 1%) than for the central samples (0 to 0.8%). For (Ar, central) samples, it is nearly zero.

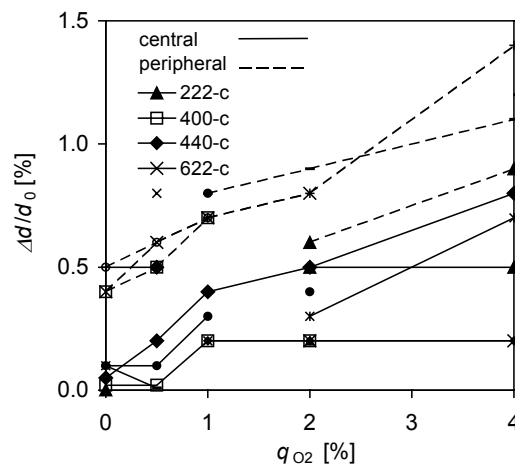


Figure 5-35 Lattice distortion $\Delta d/d_0$ as a function of the oxygen admixture q_{O_2} to the sputter gas

The grain size determined from the peak width decreases with increasing q_{O_2} generally. Representative values for the various sputter processes are summarized in Table 5-10. Grains with (440) orientation are much smaller than those with (400)-orientation. On the contrary, the random strain $\langle \varepsilon \rangle$ of (440)-oriented grains is larger than that of (400)-oriented. The biggest grains are those with (222) orientation obtained in the process (Ar, central). This is different from our results for rf-sputtered films where (222)-grains were found to be always smaller than (400)-grains (Mergel et al 2001). However, the line broadening of (222)-reflex is more possible due to the random microstrains (see section 5.2.1.2).

Table 5-10 Grain size at $q_{O_2} = 1\%$ if not stated otherwise

Orientation	Ar, central	Ar, peripheral	Ne, central	Ne, Peripheral
(222)	83	-	15 (at 2%)	-
(400)	70	64	44	40
(440)	42	31	21	17
(622)	44	37	18 (at 2%)	18

The small size of (222)-grains in rf-diode sputtered films was attributed to more oxygen incorporation in (222)-oriented grains. For the current process, grains with this orientation exhibit zero lattice distortion indicating the absence of interstitial atoms. This may explain their big size. The smallest grain size is observed for the process (Ne, edge) that yields the biggest lattice distortion. The grain size generally decreases with increasing lattice distortion. Large grains (> 50 nm) occur only in samples with zero or negative lattice distortion. For $\Delta d/d_0 = 1\%$, d_g is below 20 nm.

AFM micrographs of a central and peripheral film are shown in Figure 5-36(a) and (b), respectively. The domains in the central film tend to have a hexagonal form whereas those in the peripheral film look like scales. A “scale” profile for the peripheral sample shown in Figure 5-36(b) is given in Figure 5-36(c), revealing a strong shadowing effect. The profile of a film with low packing density (0.82), see Figure 5-37, shows that the film consists of isolated columns.

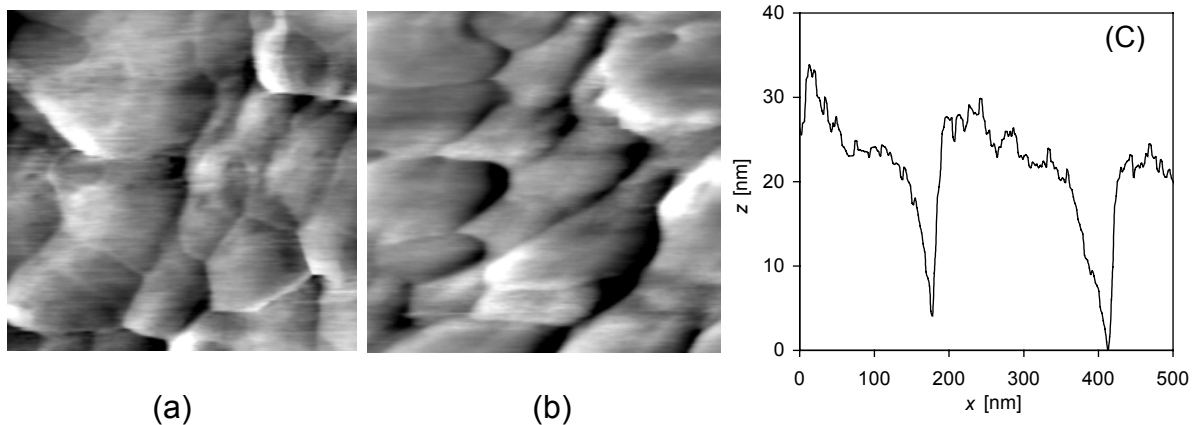


Figure 5-36 AFM micrographs (500×500 nm) of the (a) central and (b) peripheral sample prepared in the same run (Ar , $q_{O_2} = 0.33\%$, $400^\circ C$), and (c) the profile of the sample shown in (b) along the horizontal direction

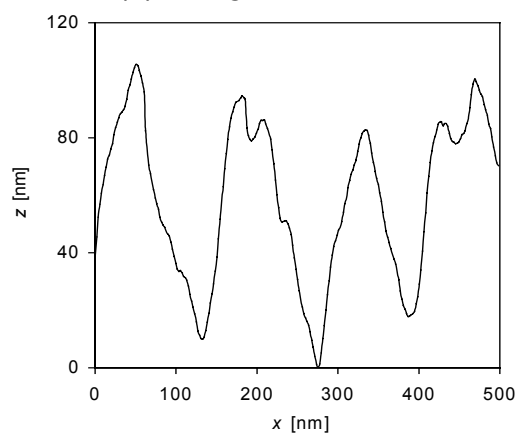


Figure 5-37 Profile of the peripheral sample (Ne , $q_{O_2} = 4\%$) with low packing density of 0.82

(4) Electrical properties

The electrical resistivity ρ_e was determined from the sheet resistance and the film thickness. It increases with increasing q_{O_2} and is bigger for peripheral samples, see Figure 5-38. It is also shown that the electrical resistivity for films sputtered with Ne increases strongly when q_{O_2} is larger than 2%.

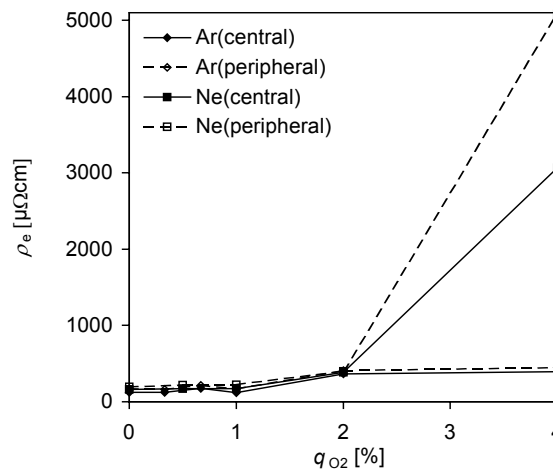


Figure 5-38 Electrical resistivity ρ_e as a function of q_{O_2}

5.2.2.3 Discussion

(1) Lattice distortion

Under certain conditions (low pressure, optimal oxygen flux, low temperature), rf sputtered $\text{In}_2\text{O}_3:\text{Sn}$ films are overdense, superoxidic and have a strongly expanded lattice (up to 3.5%) (Mergel et al 2000). These findings were explained with a model of oxygen incorporation into the bixbyite structure due to subplantation during deposition (see section 5.2.1). The current samples have been dc sputtered at relatively high temperature. Their lattice distortion is less than 1%.

The lattice distortion is a measure of the concentration of interstitial atoms. Its increase with increasing q_{O_2} indicates that these interstitials are oxygen atoms. Interstitial oxygen captures electrons and forms scattering centers (Frank and Köstlin 1982). Both effects increase the electrical resistivity (see Figure 5-39).

The grain size decreases with increasing lattice distortion, i.e. with increasing concentration of interstitial oxygen. This is explained by segregation of superstoichiometric oxygen during deposition or post-annealing into grain boundaries. More grain boundaries are formed when the initial concentration of interstitials is higher.

On the other hand, the nonuniform strains, which could also contribute to the line broadening of XRD peaks, increase with increasing lattice distortion. The reason has been explained in section 5.2.1.2.

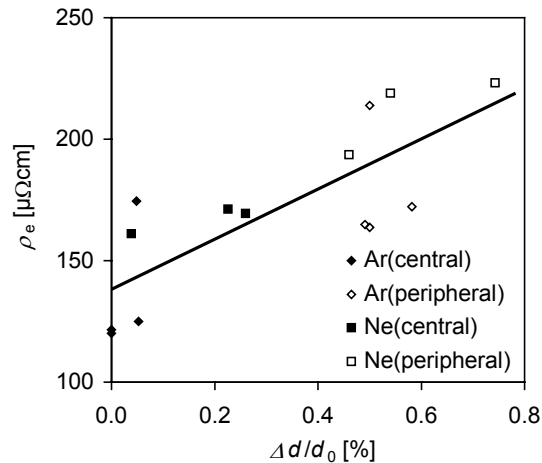


Figure 5-39 Electrical resistivity ρ_e as a function of the average lattice distortion $\Delta d/d_0$

In central films, (400)-oriented grains are larger than (440)-oriented grains. This is similar to our results for rf sputtered films and is explained by a higher resistance of the (100) surface against subplantation (Mergel et al 2001). New in the current investigation are the big grain size and minimum lattice distortion of (222) for the (Ar, central) process. This may be explained by generally less bombardment with energetic particles in the central position due to the localized dc plasma compared to the rf sputtering process. Bombardment with energetic particles suppresses the (222) orientation as was shown for microwave assisted sputtering: At low discharge voltage where only a low energetic bombardment occurs, the (222) orientation is much more pronounced than at higher discharge voltage (Latz et al 1997).

Film deposition in the peripheral position differs from that in the central position in several respects. The deposition rate is lower. The particle incidence is oblique. The exposure to the plasma is stronger because the substrate is mounted above the erosion track.

In peripheral samples, the lattice is generally more distorted. This may arise from more oxygen subplantation because the peripheral sample was exposed above the erosion track where the plasma is denser and contains more active oxygen.

(2) Packing density

The packing density of the peripheral samples is smaller than that of the corresponding central samples, by 4% and 2% for the Ar- and Ne-sputtered films,

respectively. The functional dependence of the density of evaporated Ge films on the incident angle has been investigated both experimentally and theoretically (Tait, Smy and Brett 1990). A reduction of about 5% is found for an angle of 35° and was attributed to shadowing effect. In our geometry, the angle of the line from the center of the peripheral film to the center of the target to the film normal is roughly 35°. Therefore, we explain the lower density at the periphery by oblique particle incidence leading to the columnar microstructure demonstrated in Figure 5-37.

The functional dependence of the packing density ρ_p on increasing oxygen flux q_{O_2} is different for center and peripheral samples. At the periphery, ρ_p decreases due to the formation of a porous columnar microstructure. In the center, the density increases and approaches the crystalline value for $q_{O_2} > 0.5\%$. The isotropic particle flux prevents pores.

(3) Texture of crystalline orientations

For $q_{O_2} < 1\%$, the (222)-peak is very broad or absent in peripheral samples. At the periphery, the deposition rate is lower and the effect could be a consequence of the relatively bigger oxygen flux to the growing films. However, with increasing oxygen admixture to the sputter gas a shift from (400) to (222) generally occurs. This is observed in our experiments, Figure 5-34, for $q_{O_2} > 1\%$ and has been reported in the literature for facing-target sputtering (Tominaga et al 1996), for dc magnetron sputtering (Choi et al 1995) and for microwave assisted sputtering (Latz et al 1997). Therefore, we suppose that the suppression of the (222)-peak described above results from a geometric effect due to oblique particle incidence and/or stronger bombardment out of the plasma because the peripheral substrate is mounted above the erosion track.

(222)-oriented grains are less resistant against resputtering than (400)-grains (Kamei, Shigesato and Takaki 1995). Based on this finding, the relatively smaller size of (222)-grains in rf-sputtered films was explained by more oxygen incorporation (Mergel et al 2001). RF-sputtered films generally experience a bombardment with particles of high energy. The same model may be applied here to explain the relatively smaller grain size in peripheral samples because the oxygen incorporation is more pronounced there as is proven by the bigger lattice distortion.

5.2.3 Effect of the Film Thickness on the Properties of ITO Films

The properties of ITO films are strongly dependent on the deposition conditions, most significantly on substrate temperature, oxygen partial pressure, and the distance between the target and the substrate. There have been a lot of reports on related work. Some researchers have also studied the effect of film thickness on the properties of ITO films, e.g. Kim et al (2000) reported on the properties of ITO thin films (40 – 870 nm) grown by pulsed laser deposition and Guittoum et al (1999) studied the influence of film thickness on the physical properties of ITO films prepared by dc diode sputtering at low substrate temperature (80°C).

In this section, an extensive study of the effect of film thickness on the growth and the microstructural, electrical, and optical properties of ITO films is reported. The results are interpreted in terms of the change of film structure occurring at the critical film thickness (~0.5 μm).

5.2.3.1 Experimental details

The films were deposited by dc magnetron sputtering with a von Ardenne Laboratory System LA 500S as described in section 3. The vacuum chamber was evacuated down to a base pressure of 2×10^{-5} mbar prior to the deposition. The Ar and O₂ were then introduced into the chamber yielding a sputtering pressure of about 6×10^{-3} mbar. The sputter power was 200 W. For all experiments, the substrates were kept at a temperature of 300°C and the oxygen partial pressure q_{O_2} was maintained at 0.5%, which had been proven to yield a good compromise between high conductivity and high transparency in this system. The target was presputtered 10 min. in the chosen Ar/O₂ mixture. Film thicknesses from 45 nm to 1.74 μm and 15 nm to 1.37 μm were obtained for central and peripheral samples, respectively, by varying the deposition time from 17 sec to 10 min.

5.2.3.2 Experimental results and direct conclusions

(1) Deposition rate

The deposition rate as a function of the mass-equivalent film thickness (d_m) is shown in Figure 5-40. The mass-equivalent thickness was derived from the mass per area of the film divided by the crystalline density of ITO ($\rho = 7.12 \text{ g/cm}^3$). The deposition rate increases with increasing film thickness and is constant above 0.5 μm . The low deposition rate at the initial growth of the film may be due to the small sticking coefficient of the coated material on the substrate. The deposition rate for peripheral samples (about 2.3 nm/s) is smaller than that for the central

samples (about 2.9 nm/s). This can be attributed to the effect of sputter geometry (see section 5.2.2).

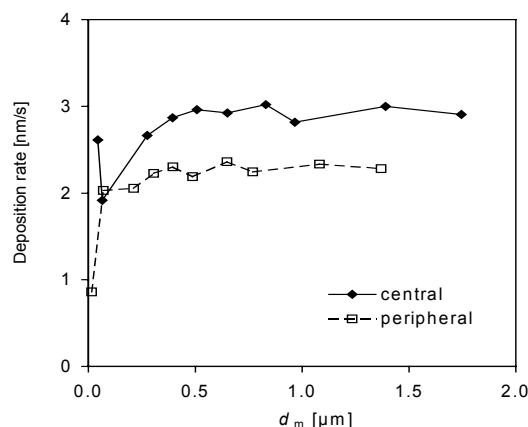


Figure 5-40 Deposition rate as a function of d_m

The intensity of XRD peaks for the quartz substrates on which the ITO films were coated is plotted in Figure 5-41 as a function of d_m . The peak position of quartz is about $2\theta = 21.67^\circ$. It is observed that both the central and peripheral samples fit an exponential function well, indicating that the intensity of the quartz reflexes decreases with increasing film thickness. This is because all reflexes yielding from the underlayer are absorbed partly when they pass through the upper films and the absorption is correlated with the film thickness by means of an exponential function. The good fitting provides a strong evidence for the reliability of the mass weighing because the d_m is derived from the mass of the films.

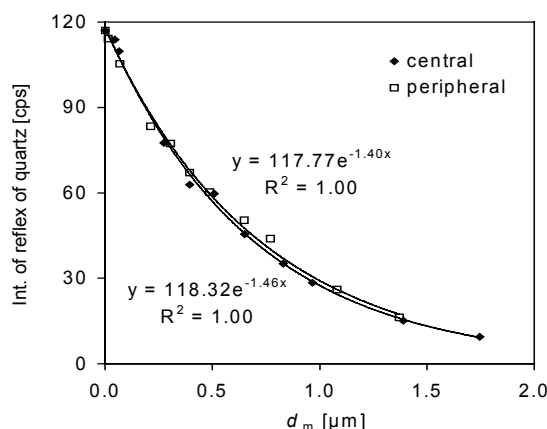


Figure 5-41 The intensity of XRD peak from the quartz substrate as a function of the film thickness coated on it

(2) Structural properties

Figure 5-42 shows the mass density of the films as a function of d_m . A density close to the crystalline value of 7.12 g/cm^3 is observed for films with thickness between 0.5 and $1.4 \mu\text{m}$. The values for the peripheral samples are higher. They are, however, less reliable due to the inhomogeneous thickness profile across the

diameter. Below 0.4 μm , the density decreases with decreasing film thickness. The smaller density for the thin films could be attributed to the incompletely covered surface.

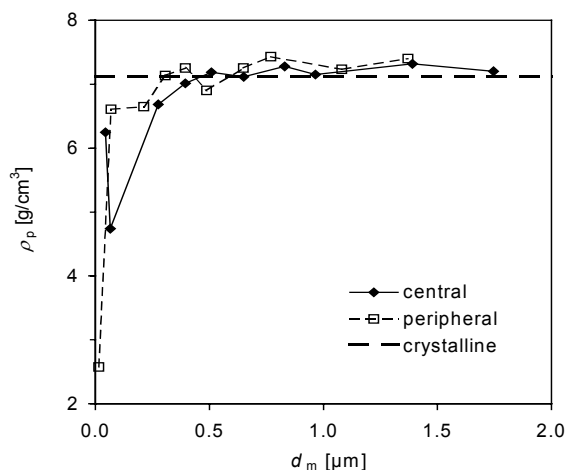


Figure 5-42 Mass density as a function of d_m

X-ray diffraction patterns of films with thickness of 0.1, 0.3, 0.5, 1.0 and 1.75 μm at central and peripheral position are displayed in Figure 5-43. All the films show polycrystalline structure regardless of the thickness. A characteristic shift towards lower angle compared to reflexes of ideal crystals is always observed for all peaks. This indicates a systematic lattice expansion. Samples in the peripheral position exhibit generally broader peaks, indicating a smaller grain size, and less pronounced (222) and (440) reflexes. These results are similar to previous results on ITO films deposited under different conditions (see section 5.2.2).

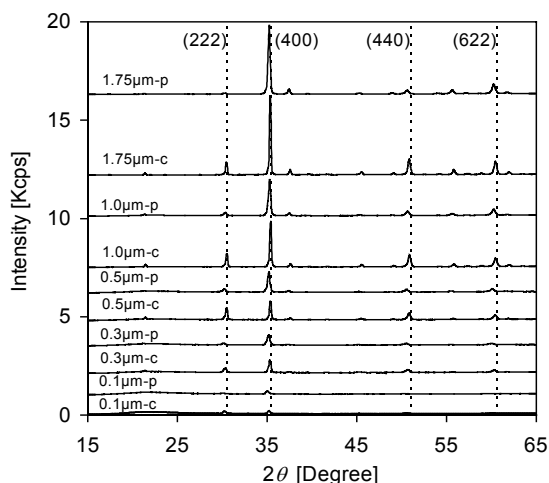


Figure 5-43 X-ray spectra of samples with different thickness

Generally, the lattice distortion decreases with increasing d_m (Figure 5-44). It is higher for peripheral samples: on the average 0.7% at 1 μm as compared to 0.3% for central samples. The lattice distortion of (400)-oriented grains is always smaller than that of (222) oriented grains. Shigesato, Takaki and Haranou (1991) have

also reported that the lattice distortion decreases with increasing film thickness for their sputtered ITO samples. However, the lattice distortion of our central samples is smaller compared with their results: 0.87% (114 nm) and 0.54% (762 nm) for (400) orientation.

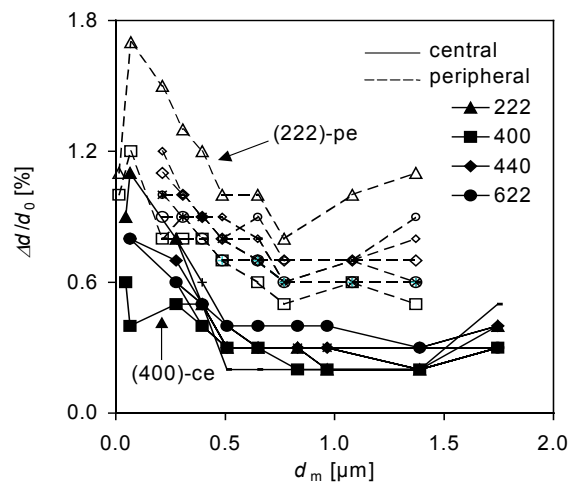


Figure 5-44 Lattice distortion as a function of d_m

The grain size for four representative orientations in ITO films is plotted as a function of d_m in Figure 5-45. It is observed that the grain size generally increases with increasing film thickness and there is a step between 0.3 and 0.4 μm . It can also be concluded that the grain size is inversely correlated with the lattice distortion. Akkad, Punnoose and Prabu (2000) have reported that the grain size for the ITO films prepared in pure Ar atmosphere by rf magnetron sputtering increases from 9 nm to 28 nm when the film thickness increased from 90 nm to 880 nm. However, they have not observed a step as the film thickness increased and the lattice distortion is nearly independent of film thickness.

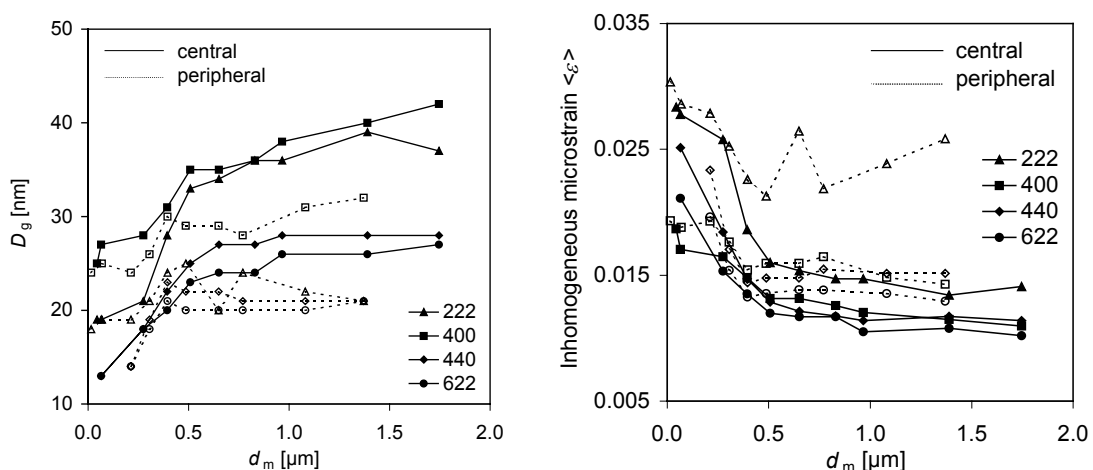


Figure 5-45 Grain size (left) and inhomogeneous microstrain (right) as a function of d_m

Alternatively, the inhomogeneous strain for the same four orientations is also plotted as a function of d_m in Figure 5-54. Similar to the lattice distortion, the microstrain decreases with increasing film thickness as well.

Figure 5-46 shows the texture of the films as a function of the film thickness d_m . The total scattering power was calculated by means of hw as well as hw^3 . And it is shown that the tendency of the texture in both cases is similar. For $d_m > 0.5 \mu\text{m}$ the texture is independent of the layer thickness. An equidistribution of many orientations is observed with (400), (622) and (611) being the more prominent ones. While for thin films, only (400) and (222) orientations are observed.

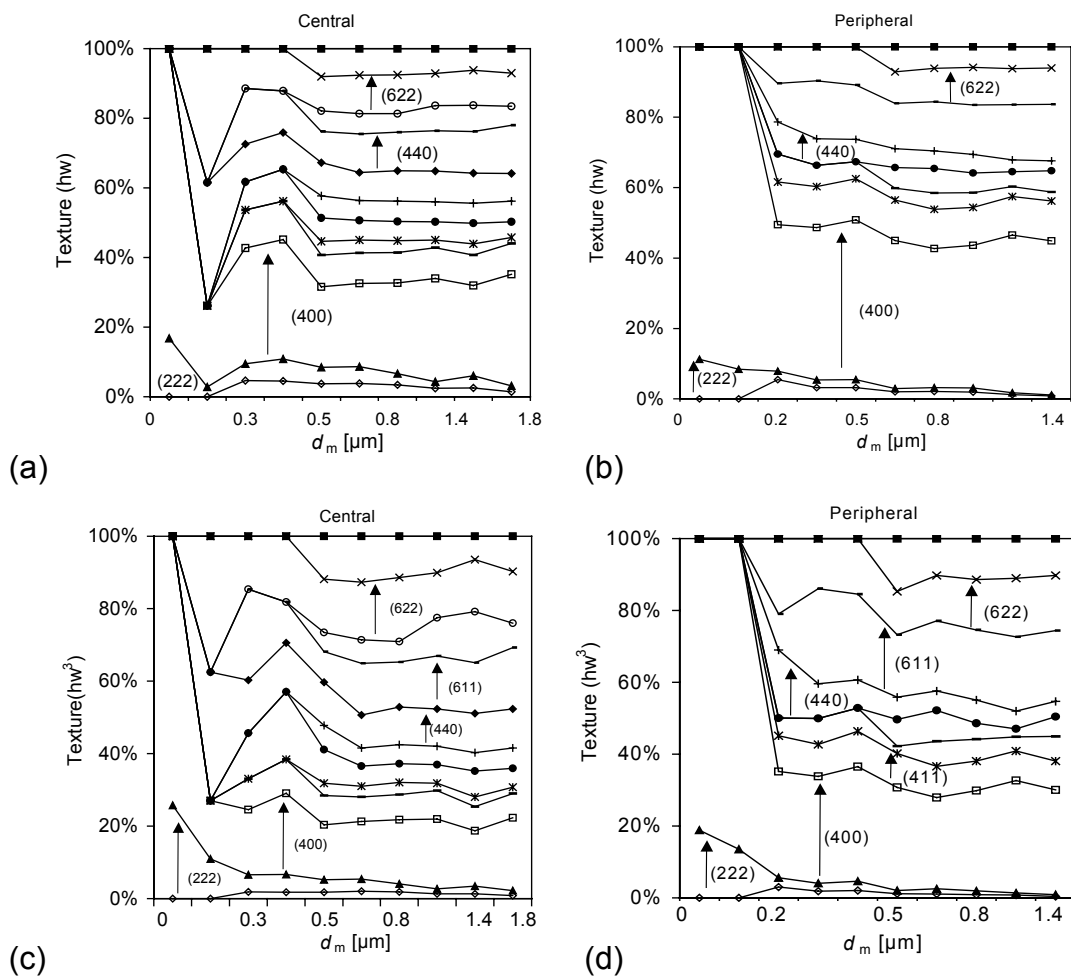


Figure 5-46 Texture as a function of d_m for (a) central (hw) (b) peripheral (hw) (c) central (hw^3) (d) peripheral (hw^3) samples

From the texture of the films another conclusion can be obtained, i.e. the peak intensity ratio of $I(222)/I(400)$ decreases with increasing film thickness. This case is more prominent when the intensity is derived from hw^3 (see Figure 5-47). It is also observed that the intensity ratio of $I(222)/I(400)$ is much smaller in peripheral samples.

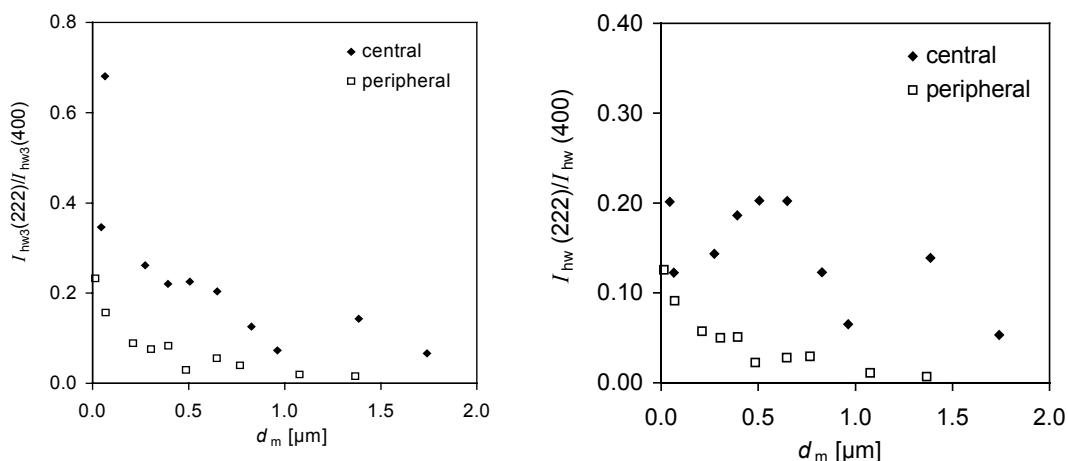


Figure 5-47 Intensity ratio of $I(222)/I(400)$ as a function of d_m (the intensity is derived from $h\nu^3$ (left) and $h\nu$ (right))

(3) Optical properties

The transmittance and reflectance spectra of films with thickness $d_m = 0.2, 1.0$ and $1.75 \mu\text{m}$ together with the simulated curves are shown in Figure 5-48. The simulated curves are shown as grey lines inside the experimental spectra. The transmittance decreases from 89% to 68% for central samples (65 nm - $1.74 \mu\text{m}$) and from 90% to 77% for peripheral samples (70 nm - $1.37 \mu\text{m}$).

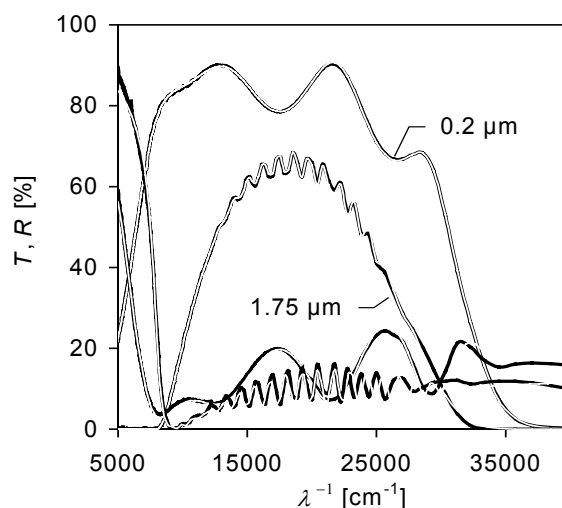


Figure 5-48 Transmittance and reflectance of films with $d_m = 0.2, 1,$ and $1.75 \mu\text{m}$ together with simulated curves which is shown as a white line inside the experimental curves

Simulation of the spectra was performed with a dielectric model (see section 5.1.2). A one-layer model fits the experimental data very well. The ratio of optically and mechanically determined film thickness $d_{\text{opt}}/d_{\text{stylus}}$ is 1.020(15) and

1.050(25) for central and peripheral samples, respectively. The number in the brackets describes the standard deviation of the last two digits.

The optically derived free carrier density N_{Dr} in the films is depicted in Figure 5-49 as a function of d_m . For central samples and $d_m > 0.5 \mu\text{m}$, N_{Dr} is close to $1.4 \times 10^{21} \text{cm}^{-3}$. The Sn concentration is $6.49 \times 10^{21} \text{cm}^{-3}$ in the target, i.e. the doping efficiency is 18% supposing all free electrons are contributed by Sn dopants. In samples with $d_m = 0.1$ and $0.3 \mu\text{m}$, N_{Dr} is less than $1.2 \times 10^{21} \text{cm}^{-3}$. The carrier density in the peripheral samples is 50% lower. The fact that our carrier density is larger than that of the others (Shigesato, Takaki and Haranou 1991) coincides with the result that the optically determined carrier density is larger than that of electrically derived by Hall Effect measurement (Mergel and Qiao 2002).

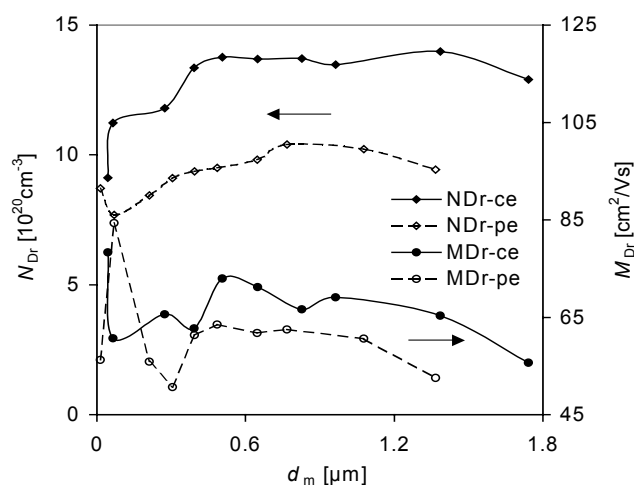


Figure 5-49 Carrier density and Drude mobility as a function of d_m

The Drude mobility M_{Dr} is obtained from the damping Γ_{Dr} of the Drude term (see section 5.1.1). For samples with $d_m = 0.5$ to $1 \mu\text{m}$ it is about $75 \text{cm}^2/\text{Vs}$ (central) and $70 \text{cm}^2/\text{Vs}$ (peripheral). This is close to the maximally observed mobility for single crystals of $95 \text{cm}^2/\text{Vs}$ (Wen et al 1992). However, the factor that the optically determined free carrier mobility is larger than that of electrically determined by Hall Effect should be also taken into account (Mergel and Qiao 2002).

The OJL band gap and the refractive index at 550nm are displayed in Figure 5-50 as a function of d_m . The band gap is about 4.1eV for central samples with the thickness of $0.3 - 1.4 \mu\text{m}$. This is higher than the literature values for the direct band gap of $3.52 - 3.85 \text{eV}$ (Hamberg and Granqvist 1986; Weijtens and van Loon 1991) and the value 3.53eV reported in the literature for similar carrier densities (Weijtens 1990). The band gap is found to be smaller for peripheral films by about 0.12eV . It decreases below $0.4 \mu\text{m}$. The values at $1.75 \mu\text{m}$ are extraordinarily high. This might be an artifact of the simulation, because the transmittance of thick samples is relatively low and exhibits no pronounced interference pattern. It is

shown that the band gap increases with increasing film thickness. This can be explained by BM shift, because the free carrier density increases with increasing film thickness and the band gap increases with increasing carrier density. In contrast, the refractive index of peripheral samples (1.95 - 1.78) is always larger than that of central samples (1.83 - 1.77) and it decreases with increasing film thickness (Figure 5-50).

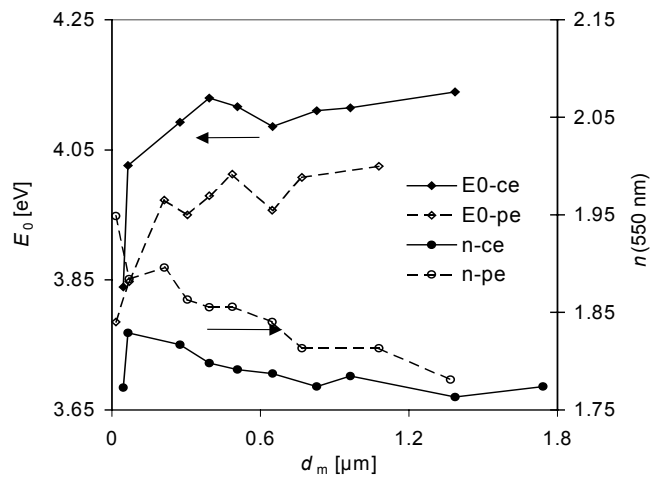


Figure 5-50 Band gap and refractive index (at 550 nm) as a function of d_m

(4) Electrical properties

Figure 5-51 shows that the electrical resistivity ρ_e decreases when the thickness d_m increases from 40 nm to 0.4 μm , and reaches a constant value of 150 $\mu\Omega\text{cm}$ for central samples in the range from 0.5 to 1.75 μm . The resistivity of peripheral samples is approximately 40 $\mu\Omega\text{cm}$ larger than that of central samples. These phenomena can be attributed to different carrier densities in the films. It is also displayed (Figure 5-51) that the optically derived ρ_e is lower than the electrically determined ρ_e , which results from the higher optically determined carrier density and mobility that has already been observed previously (section 5.1.2).

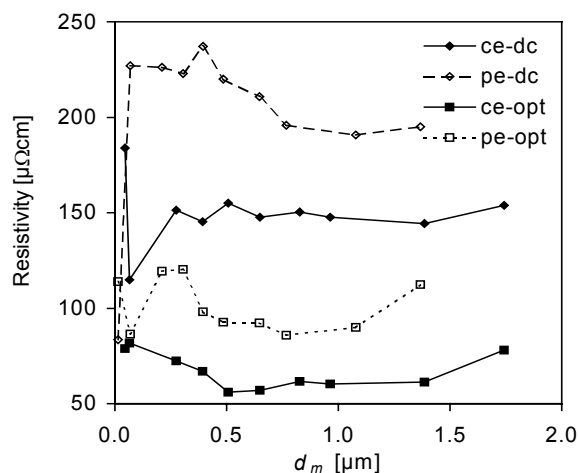


Figure 5-51 Electrically and optically derived electrical resistivity as a function of d_m

(5) Surface morphology

Figure 5-52 shows the surface roughness (rms) as a function of film thickness. It is observed that the roughness of the central samples increases from 1.7 nm to 8.5 nm monotonously as the thickness increases from 40 nm to 0.3 μm , whereas that of the peripheral films remains low. The roughness of thick films decreases with increasing thickness but the variation is not much.

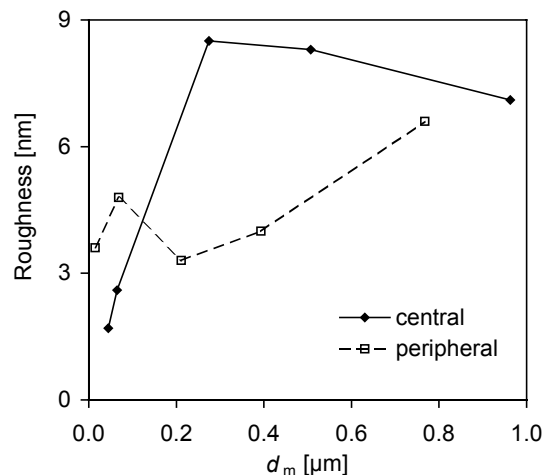


Figure 5-52 Surface roughness as a function of d_m

Figure 5-53 (a), (b) and (c) display the AFM images ($2 \mu\text{m} \times 2 \mu\text{m}$) of the central film with thickness of 0.3 μm and films with thickness of 1.0 μm at central and peripheral position, respectively. Comparing these three images it is found that the grain size parallel to the film surface (“lateral grain size”) increases with the film growth. The lateral grain size of the central films is also larger than that of peripheral films.

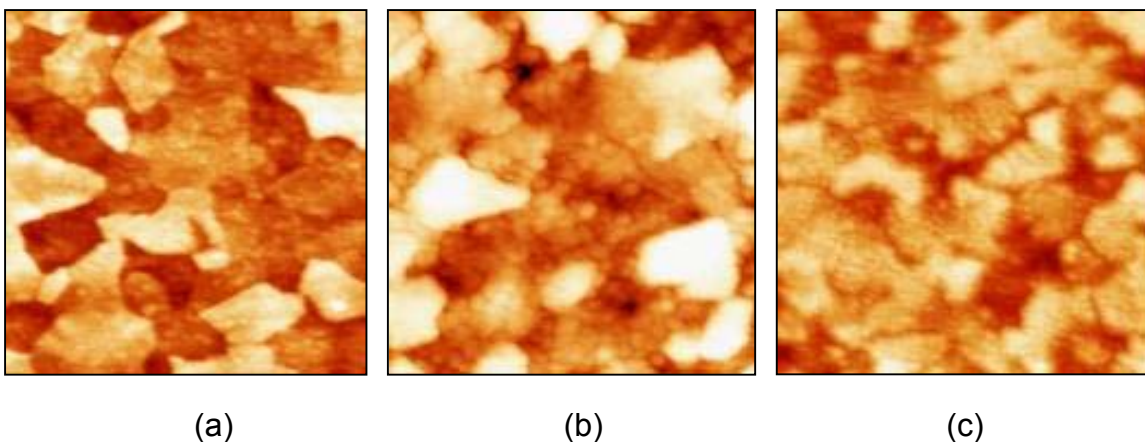


Figure 5-53 AFM images ($2 \times 2 \mu\text{m}$) of film surface morphology.
(a) 0.3 μm , ce; (b) 1 μm , ce; (c) 1 μm , pe

5.2.3.3 Discussion

So far, it is clear that the central films are characterized by smaller lattice distortion and random strain, bigger grain size and higher surface roughness, compared to the peripheral films. These results are attributed to the less bombardment by the energetic particles on the central position (see section 5.2.2). Moreover, in the beginning of the film formation, the deposition rate is lower and the films with smaller density, higher lattice distortion and smaller carrier density, while the thick films ($> 0.5 \mu\text{m}$) are more equilibrium.

(1) Film growth

From the above detailed analyses on the films microstructure based on x-ray diffraction studies, it is inferred that there exists a critical thickness at about $0.5 \mu\text{m}$. The microstructures for films below and above the critical thickness are significant different. It is also observed that the difference between the thin and thick films also happened to the deposition rate and the electrical and optical properties of the ITO films in the same thickness range. Obviously there must be some correlations between the films microstructure and their properties.

It is shown in Figure 5-47 that the peak intensity ratio of $I(222)/I(400)$ increases drastically when $d_m < 0.5 \mu\text{m}$, indicating that the (222)-oriented grains are favoured in the thin films. Meanwhile the deposition rate is very low for the thin films. This can be explained as follows. According to the report of Thilakan and Kumar (1997) on the change of preferred orientation of ITO films, the predominant orientation changes from (222) to (400) as deposition rate increases. It has also been revealed (Terzini 2000) that if the film contains sufficient oxygen the crystal growth is preferentially with (222)-oriented grains, otherwise, the crystal growth is much faster, with (400) orientation. Based on these findings, we infer when the deposition rate is low the film surface is exposed to the Ar/O₂ sputter atmosphere more time, which helps to accumulate more oxygen in the structure, leading to the favor growth of (222)-grains. As the deposition rate increases the film has the preferred orientation along the (400) direction. In return, the change in orientation from (222) to (400) also influences the deposition rate because (222)-oriented grains are less resistant against resputtering than (400)-grains (Kamei, Shigesato and Takaki 1995). The more (400)-grains, the less resputtering would be, which also resulted in the higher deposition rate.

There is another evidence to prove that the growth of (222)-grains is suppressed with increasing thickness. In this work, we estimate the fraction of grains with a certain orientation by the product of hw and hw^3 of the corresponding x-ray peak. In Figure 5-54, the scattering power of four representative peaks as a function of

d_m is shown by means of hw and hw^3 . It has been confirmed that the evaluation with hw^3 yields approximately the same total x-ray scattering intensity for all films with comparable thickness (Mergel et al 2001). Therefore it is expected that the scattering power of each peak should be proportional to the film thickness if this orientation grows in the through-thickness direction. Actually, such result is observed for most orientations except (222) (see Figure 5-54), considering the absorption effect leading to a deviation from the linear function which is confirmed by the quartz reflex (Figure 5-41). Furthermore, it is worth noting that the intensity of (222) orientation does not increase any more when $d_m > 0.5 \mu\text{m}$ and decreases as the thickness increases. Based on the above analysis we suppose that the growth of the (222)-grains is suppressed with the increasing thickness.

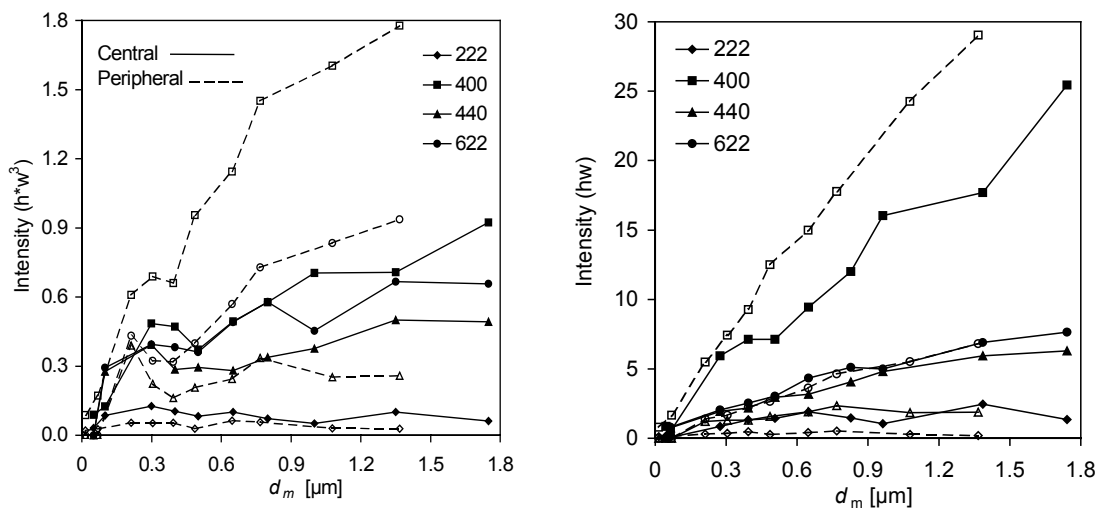


Figure 5-54 The scattering power of four representative peaks in ITO films as a function of d_m by means of hw^3 (left) and hw (right)

In order to investigate the difference of the microstructure between the thin and thick films, the cross-sectional microstructure of the ITO films has been detected by scanning electron microscopy (SEM), and the micrographs of the films with the thickness of 0.65 and 1.35 μm are shown in Figure 5-55. From Figure 5-55 (a) it is observed that some grains grew in the through-thickness direction, but others did not. And it can be seen in Figure 5-55 (b) that there is a very clear columnar structure in the underlayer of the film, while the upper layer looks denser and the columnar structure is not so obvious.

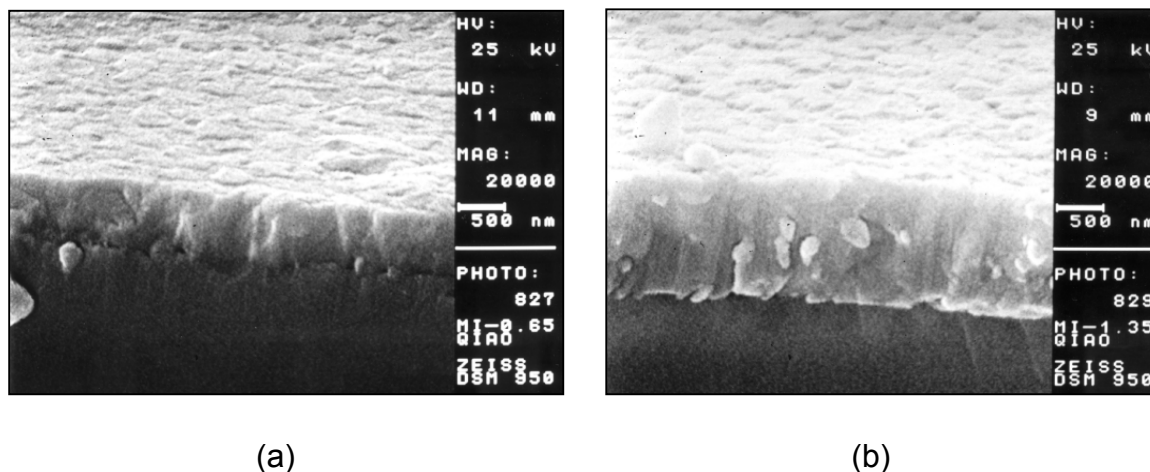


Figure 5-55 SEM micrographs of the cross section of ITO films with the thickness of 0.65 μm (a) and 1.35 μm (b)

For the thin films ($d_m < 0.4 \mu\text{m}$), the mass density is much lower than that of the thicker films which is close to the crystalline value. Considering the above experimental results and analyses on the film growth and microstructure, we suggest that the thicker films consist of two layers, where the underlayer is looser due to the poor crystallization while the equilibrium top-layer is denser. Although this model can explain the experimental result, we do not have definite evidence yet. However, it has been confirmed that the films consisted of two different strained (lattice distortion) layers for ITO film deposited by dc magnetron sputtering at low substrate temperature (185°C) (Hoon Yi et al 1995).

The optical transmittances of thick films have also been simulated based on the dielectric modeling with two-layer model. The simulations are successful and the thickness of the underlayer of the films is about $0.2 \sim 0.3 \mu\text{m}$. However, the two-layer model can not improve the simulation much because the one-layer model has already been very satisfied.

(2) Film Structure and properties

The correlation of the lattice distortion and the grain size with the film thickness can be explained with the model of oxygen incorporation into the bixbyite structure due to subplantation during deposition and segregation to grain boundaries (Mergel et al 2000). According to this model, more oxygen incorporation leads to a larger lattice distortion and a smaller grain size. Based on the above analysis on the film growth, it is known that on the initial of the film growth, there is more oxygen incorporating into the structure leading to the (222) preferential orientation. With the film growing, the oxygen incorporation becomes less and the structure changes. This is demonstrated by the result that the lattice distortion of (222) orientation is always bigger than most of the others. Consequently, the lattice

distortion decreases and grain size increases with increasing film thickness. In peripheral samples, the lattice is more distorted. This may arise from more active oxygen in the plasma because the peripheral samples are above the erosion track as mentioned in section 5.2.2.

From AFM study it is observed that the surface roughness increases with increasing thickness. The increase of the roughness is due to the grain size increasing with the film thickness. This effect has also been reported by Meng and Dos Santos (1997). And it is worth to note that the surface roughness for central samples is larger than that for peripheral samples. This may be because the grain size of central samples is larger than that of peripheral samples. Additionally, the different ratio of the (222)- to (400)-oriented grains in a thin film could also lead to the varying of the surface roughness because the thicknesses for these two oriented grains are different (Kamei, Shigesato and Takaki 1995) (also see section 5.3.2).

Since the incorporated oxygen behaves as an electron trap, the carrier density decreases with increasing lattice distortion. So it is observed that the carrier density increases with increasing thickness up to $d_m > 0.5 \mu\text{m}$ and then becomes more or less constant. Such tendency is also observed for the band gap. The widening of the band gap can be attributed to the increase of the carrier concentration in ITO films, which is known as Burstein-Moss shift.

The Drude mobility in our various thickness films scatters in a large range. But generally, the mobilities of central and thicker samples are larger than those of peripheral and thinner samples. Interstitial oxygen captures electrons and forms scattering centers. Both effects increase the electrical resistivity.

Due to the increase of the carrier density with increasing film thickness, the real part of the complex dielectric function also moves towards higher frequencies, which results in the decrease of the refractive index at the wavelength of 550 nm.

(3) Possibility to improve the properties of the films

According to above analyses based on the experimental results, it is known that the poor properties for the thin films are mainly due to the more oxygen incorporation into the crystalline structure although a certain additional oxygen to the sputter gas is necessary for a good crystallization of the films for most deposition processes. Latz et al (1997) have, however, found that for films with 100 nm thickness prepared by microwave assisted sputtering, the good electrical and optical properties could be achieved in the case of no additional oxygen. All these reveal a way to improve the properties of the films, i.e. prevent from more oxygen incorporating into the films at the initial of the film growth.

5.3 RF-sputtered ITO Films

5.3.1 Method of the Experiments

The ITO films were prepared by rf magnetron sputtering method on quartz substrates using the same oxidized ITO target as for dc sputtering. The substrate temperature was 300°C. Two different sputtering powers, 100 W and 400 W, were used leading to different deposition rates. For the samples sputtered with rf power of 400 W, two different Ar fluxes, 15 sccm and 30 sccm, were used. The oxygen partial pressure was varied as well for each series. The important deposition conditions are listed in Table 5-11. In order to investigate the effect of the mechanisms of the plasma excitation, i.e. dc and rf mode, on the properties of ITO films, the properties of the dc-sputtering deposited films prepared under the comparable conditions are also compared simultaneously.

Table 5-11 Deposition conditions of rf and dc sputtered samples (the deposition rates listed in the table belong to the central samples with $q_{O_2} = 0\%$)

Deposition Parameter	RF sputtering			DC sputtering		
	100	400		100	200	
Sputter power (W)	100	400		100	200	
Sputter press. (mbar)	6.2×10^{-3}	1.2×10^{-2}	6.1×10^{-3}	1.2×10^{-2}	6.3×10^{-3}	6.3×10^{-3}
Substrate temp. (°C)	300	300	300	300	300	300
q_{O_2} (%)	0 ~ 2	0 ~ 1	0 ~ 1	0 ~ 1	0 ~ 1	0 ~ 1.5
Discharge voltage (V)	74	160	150	302	314	349
Deposition rate (nm/s)	0.26	1.40	1.14	1.12	1.21	2.8

5.3.2 Results and Discussion (comparing with dc-sputtered films)

5.3.2.1 Physical properties

The deposition rate, mass density, band gap, free carrier density and mobility, and electrical conductivity of the ITO samples prepared by rf and dc sputtering under different deposition conditions are shown as a function of oxygen partial pressure q_{O_2} in Figure 5-56 (a) – (f).

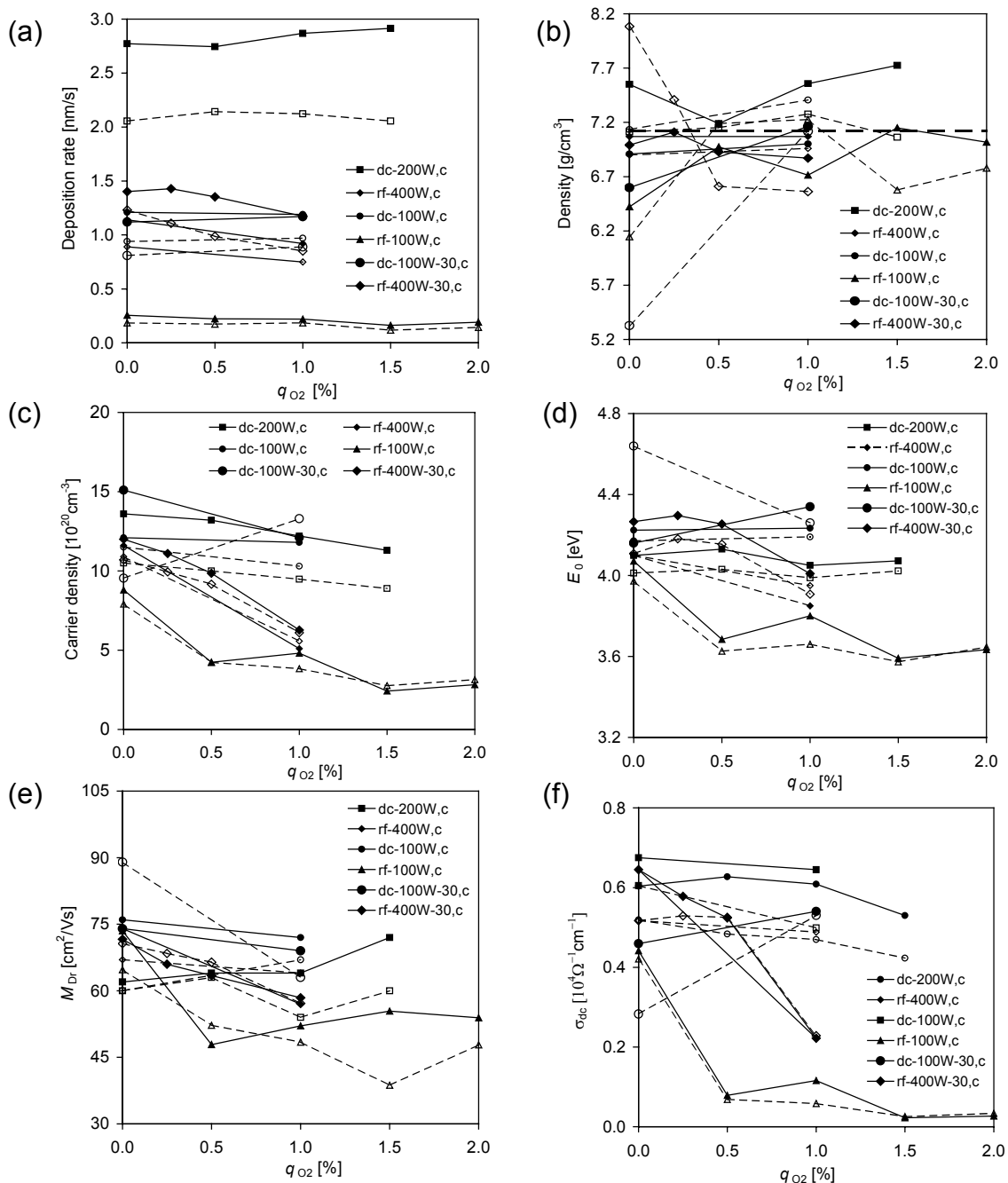


Figure 5-56 Comparison of the physical properties of dc and rf sputtered ITO films. (a) The deposition rate, (b) mass density, (c) band gap, (d) free carrier density (e) carrier mobility, (f) electrical conductivity as a function of q_{O_2} . The solid lines with solid symbols stand for the central samples, while the dash lines with open symbols stand for the peripheral samples. The small symbols stand for the low sputtering pressure (Ar 15 sccm), while the big ones stand for the high pressure (Ar 30 sccm, also stated as 30)

It is clearly displayed in Figure 5-56 (a) that the deposition rate is always proportional to the sputtering power and is bigger for central samples in both cases of rf and dc sputtering. The deposition rate as a function of q_{O_2} shows a general decrease. The mode of the excitation influences the deposition rate strongly, i.e. the deposition rate for rf sputtering is significantly lower than that of dc sputtering under the condition of constant discharge power, e.g. the deposition rate for rf 400 W deposited films is nearly a half of that deposited with dc 200 W power. This can be interpreted in terms of the lower discharge voltage V_{dis} on the target for a rf magnetron discharge compared to a dc sputtering process (see Table 5-11, the discharge voltage for rf 400 W is also nearly a half of that for dc 200 W) (Ellmer 2000), because it is well-known that the deposition rate strongly depends on the energy of sputtered particles arriving at the substrate (see section 2.5.4.1). It can also be observed that the deposition rate decreases with increasing sputtering pressure for dc excitation, while for rf sputtering such phenomena has not been observed. This can also be attributed to the different excitation mechanisms of the plasma in dc and rf sputtering modes (Ellmer 2000).

The mass densities for both rf- and dc-sputtered films scatter around the crystalline value of 7.12 g/cm^3 (see Figure 5-56 (b)).

The carrier density always decreases with increasing q_{O_2} , which can be explained by the oxygen incorporation model as described in section 5.2.1. Comparing the samples sputtered by rf 400W with the dc 100W sputtered samples which have the similar deposition rate, it is found that the rf-sputtered films have a lower carrier density than dc-sputtered films at the same q_{O_2} . This can be explained by more oxygen incorporation in rf-sputtered films compared to dc-deposited films as will be mentioned in the next section, and the incorporated oxygen behaves as electron traps. It is also observed that the carrier density increases with increasing rf power. This behaviour has been reported as well by Terzini et al (1999) for their rf-sputtered ITO samples, where the carrier concentration increased from 1.8×10^{19} to $3.8 \times 10^{20} \text{ cm}^{-3}$ when the rf power increased from 0.27 to 0.8 W/cm². The reason is that higher rf power leads to bigger deposition rate and, consequently, relative less oxygen incorporation.

The band gap decreases with increasing q_{O_2} , which obeys the Burstein-Moss shift. Generally, the carrier mobilities decrease with q_{O_2} , but there are also some exceptions. The conductivity follows the same tendency with the q_{O_2} as the carrier density.

The optically determined electrical conductivity σ_{Dr} ($\sigma_{Dr} = N_{Dr}eM_{Dr}$) is also compared with the direct current conductivity σ_{dc} determined with a four-point probe as in section 5.2.1.2. All data points lie above the line for $\sigma_{Dr} = \sigma_{dc}$. This is in

agreement with previous results and the reason has been described in section 5.2.1.

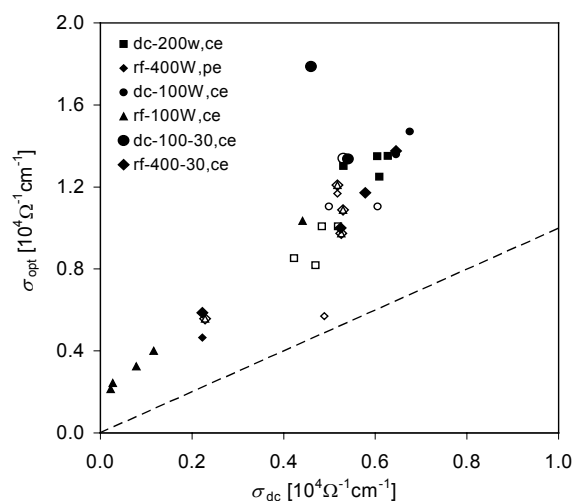


Figure 5-57 Conductivity σ_{Dr} , as calculated from N_{Dr} and M_{Dr} , against direct current conductivity σ_{dc} (The symbols have their usual meanings)

5.3.2.2 Crystalline orientation and texture

As shown in Figure 5-58, for rf-sputtered samples, the predominant orientation is (222) in both cases of 100 W and 400 W discharge power. The (400) orientation completely disappears in the case of 100 W power and is very small for the power of 400 W. It is also observed that there are more pronounced reflex peaks for ITO films with higher rf power. Generally, the XRD patterns of central and peripheral samples are similar and there is no clear effect of oxygen partial pressure on the microstructure of the rf-sputtered films. Joshi, Singh and McClure (1995) and Deng et al (2001) have prepared ITO films by rf magnetron sputtering at 40 W and 100 W with 300°C and 325°C, respectively. They have also found that for as deposited ITO films the (222)-reflex is almost the only peak that can be observed. It has also been reported that the intensity ratio of $I(222)/I(400)$ decreases with increasing rf power (Terzini, Thilakan and Minarini 2000) or substrate temperature (El Akkad et al 2000).

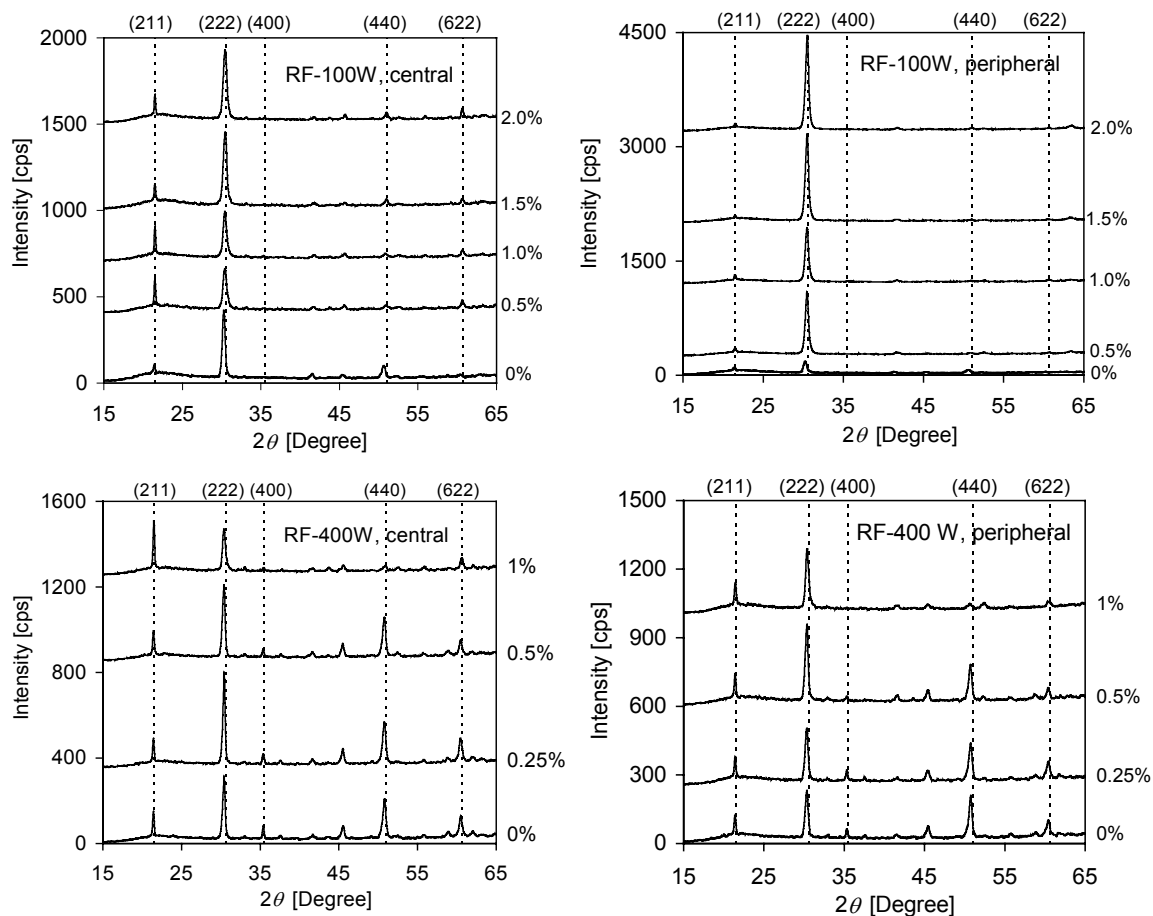


Figure 5-58 X-ray diffraction patterns for ITO films prepared by rf sputtering

In contrast, for dc-sputtering, the peaks of the (400)-reflexes are very sharp and (400) is the predominant orientation for both central and peripheral samples (see Figure 5-59). It is also shown that the intensity of the (400)-reflex decreases with increasing q_{O_2} in both cases of 100 W and 200 W power. For central films, (222) orientation is pronounced, whereas it is almost missing in peripheral films. Finally, (622) orientation is more significant for dc-sputtered ITO films than for rf-sputtered.

The differences of the crystalline orientation and texture between the rf- and dc-sputtered ITO films can be attributed to probably the different excitation modes and the different deposition rate. Exciting the plasma by dc generates higher discharge voltages compared with rf mode, which has been explained by the different roles of the secondary electrons from the target for dc and rf excitation of a magnetron plasma (Ellmer 2000). This behaviour leads to a higher energy input by reflected argon and negative oxygen ions into the growing films for dc sputtering than that for rf sputtering. And it has been reported (Kumar and Mansingh 1989) that the sputtered particles arriving at the substrate with higher energy favour the (400) orientation, while for evaporated ITO films the dominant

orientation is usually the (222)-reflex resulting from the low energy particles deposition.

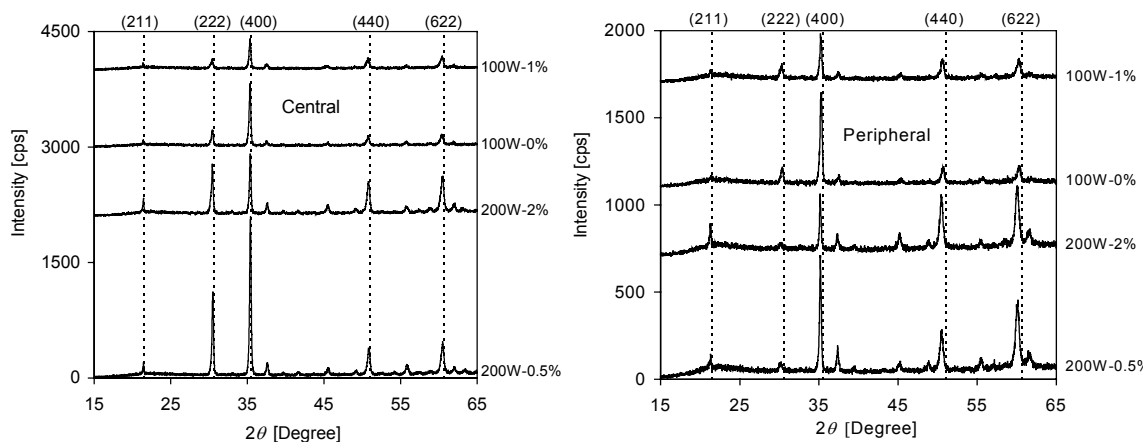


Figure 5-59 X-ray diffraction patterns for ITO films prepared by dc sputtering

On the other hand, the predominant orientation of (222) in rf-sputtered ITO films may be contributed to the larger amounts of reactive, i.e. atomic or excited oxygen and ozone in the rf discharge (Mientus and Ellmer 2001), because a reactive oxygen component is much more effective than molecular oxygen for oxidizing indium and tin (Alam et al 1999). Additionally, the lower deposition rate for rf-sputtered films also benefits the accumulation of oxygen on the growing film surface. While it has already been revealed that, if the film contains sufficient oxygen, the crystal growth is preferentially with (222)-oriented grains; otherwise, the crystal growth is much faster, with (400) orientation (Terzini 2000).

Based on above analysis, it is inferred that the preferential orientation of (222) in rf-sputtered ITO films is related to the growing films impinged by particles with lower energy and the effect of efficient oxidising.

5.3.2.3 Lattice distortion and grain size

The average grain size and lattice distortion for rf- and dc-sputtered ITO films under different discharge power and q_{O_2} are listed in Table 5-12 and Table 5-13. It is observed that the average lattice distortions for peripheral samples are almost always larger than that for central samples, while the case for the corresponding grain size is completely reverse. For rf-sputtering, the lattice distortion and grain size for central and peripheral samples are similar compared to that of the dc 200 W sputtered samples. This could be explained by that the rf-plasmas are more extended, which causes the ambient of the plasmas in which the central and peripheral samples exposed are more similar; while the dc-plasmas are more

localized, the peripheral samples are just above the erosion track. Furthermore, the lattice distortion and grain size of dc-sputtered films with 100 W powers is much similar to that of rf-sputtered films with 400 W powers, which may be due to the similar deposition rate.

Compared to dc sputtering, the lattice distortion and grain size for rf-sputtered samples under the different discharge powers are also quite close. This phenomenon can also be interpreted in terms of the different discharge mechanism between rf and dc excitation as follows. In a dc discharge, most of the energetic particles stem from the target surface (e.g. reflected neutral argon atoms or negative oxygen ions), while in a rf magnetron discharge, the largest part of the energetic particles has its origin in the plasma in front of the substrate. By varying discharge power or sputtering pressure, the virtual source will be moved (see section 2.6.3). This is possible to influence the energy of the species arriving at the substrate which have their origin at the target and consequently, the structure and morphology of thin films could be different (in the case of dc sputtering). However the energy flux into the growing film is not influenced nearly in such cases for rf sputtering (Ellmer 2000), leading to a resemble microstructure of the films.

The lattice distortion of (222) orientation is always the largest in the both cases of dc and rf sputtering.

Table 5-12 Average grain size (D_g) and lattice distortion ($\Delta d/d_0$) for rf-sputtered ITO films

q_{O_2} (%)	RF- 100 W				RF- 400 W (15 sccm)			
	central		peripheral		central		peripheral	
	D_g (nm)	$\Delta d/d_0$ (%)	D_g (nm)	$\Delta d/d_0$ (%)	D_g (nm)	$\Delta d/d_0$ (%)	D_g (nm)	$\Delta d/d_0$ (%)
0	20	0.66	19	0.88	21	0.49	19	0.69
1.0	23	0.13	21	0.20	18	0.52	18	0.82
2.0	26	0.10	22	0.14				

Table 5-13 Average grain size (D_g) and lattice distortion ($\Delta d/d_0$) for dc-sputtered ITO films

DC-100 W					DC-200 W				
q_{O_2} (%)	central		peripheral		q_{O_2} (%)	central		peripheral	
	D_g (nm)	$\Delta d/d_0$ (%)	D_g (nm)	$\Delta d/d_0$ (%)		D_g (nm)	$\Delta d/d_0$ (%)	D_g (nm)	$\Delta d/d_0$ (%)
0	26	0.4	25	0.5	0.5	28	0.25	24	0.9
1.0	22	0.4	17	0.6	2.0	26	0.33	23	1.0

In Figure 5-60, the grain size versus lattice distortion is displayed for four representative orientations of (222), (400), (440) and (622) for dc- and rf-sputtered films. It can be observed that generally the grain size decreases with increasing lattice distortion.

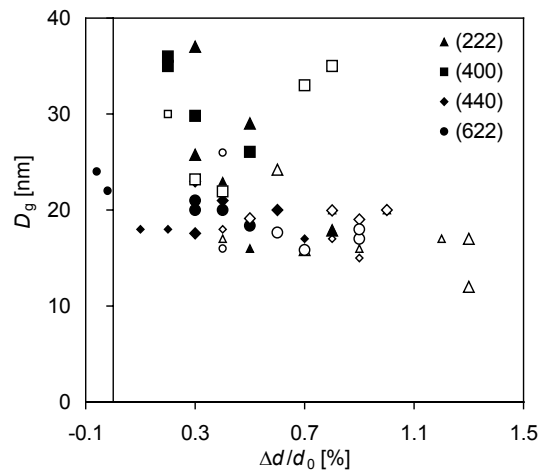


Figure 5-60 The grain size as a function of the average lattice distortion (solid and open symbols stand for central and peripheral samples, respectively; big and small symbols stand for dc- and rf-sputtered samples, respectively)

5.3.2.4 Roughness and packing density

The average vertical grain size and surface roughness measured with the AFM are shown as a function of the packing density for dc- and rf-sputtered ITO films in Figure 5-61 (a) and (b), respectively. It exhibits a clear tendency that both the vertical grain size and the surface roughness increase with increasing packing density. This is reasonable to be expected because the larger grain size means the better crystallizing structure with smaller grain boundaries, resulting in the denser films. And it has been known that the surface roughness increases with increasing grain size (Meng and Dos Santos 1997). Consequently the roughness increases with increasing packing density.

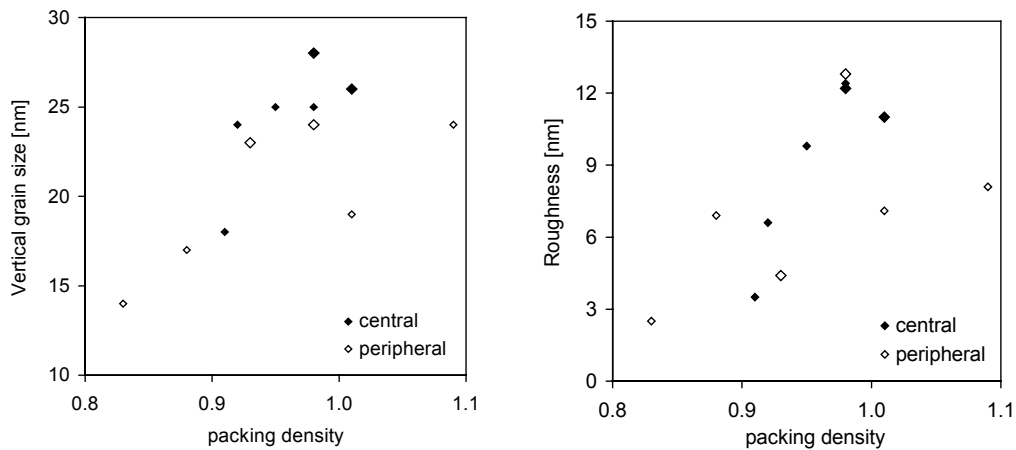


Figure 5-61 The average vertical grain size and surface roughness (rms) as a function of packing density (compared to crystal value 7.12 g/cm^3) for dc- and rf-sputtered ITO films (displayed by big and small symbols, respectively)

As shown in Figure 5-62, there is not a definite correlation between the vertical grain size and the lateral grain size.

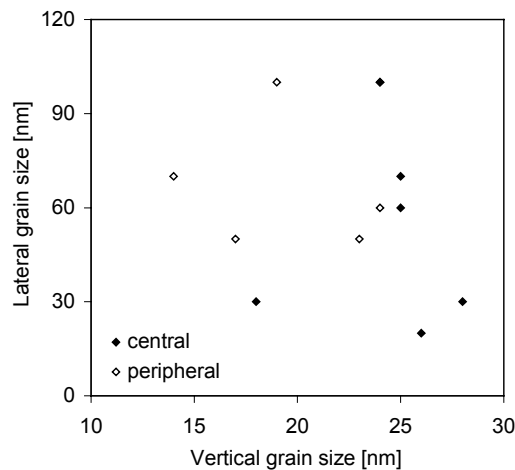


Figure 5-62 Lateral grain size versus vertical grain size for rf-sputtered ITO films

5.3.2.5 Surface morphology

Figure 5-63 (a) shows the AFM image ($1 \times 1 \mu\text{m}$) of the ITO film deposited under the condition of rf 400 W power and $q_{\text{O}_2} = 1\%$ at central position. The corresponding profile in the direction displayed by the line in the image is shown in Figure 5-63 (b). It is observed that there exists the characteristic surface morphology of grain-subgrain structure (Kamei, Shigesato and Takaki 1995). The characteristic structure possessed by sputter-deposited polycrystalline ITO films was described as grains 400 - 800 nm in size divided into highly oriented regions

10 - 40 nm in diameter. It has been revealed that there are three kinds of grains oriented with the (400), (222) and (440) direction respectively. It has also been reported that the thickness of these three kinds of grain decreased in the order of the grains consisting of (400)-, (222)- and (440)-oriented subgrains. And the thickness of the (440)-oriented grains is less than that of the other grains by about 20 nm. This behaviour was interpreted on the basis of the crystalline orientation-dependent resputtering rate of each grain type, i.e. the (400) orientation is the most resistant against resputtering (Kamei, Shigesato and Takaki 1995).

It is obviously observed in Figure 5-63 (a) and (b) that the grain size is nearly 400 nm and the subgrain size is about 10 – 40 nm which coincides with the above report. It is also worth noting that the thickness difference between region A and B is more than 20 nm, indicating that these two regions are composed of different oriented subgrains. In fact, the x-ray diffraction detection revealed that (222) and (440) are the two dominant orientations in this film. Therefore it is inferred that regions A and B are oriented (222) and (440), respectively.

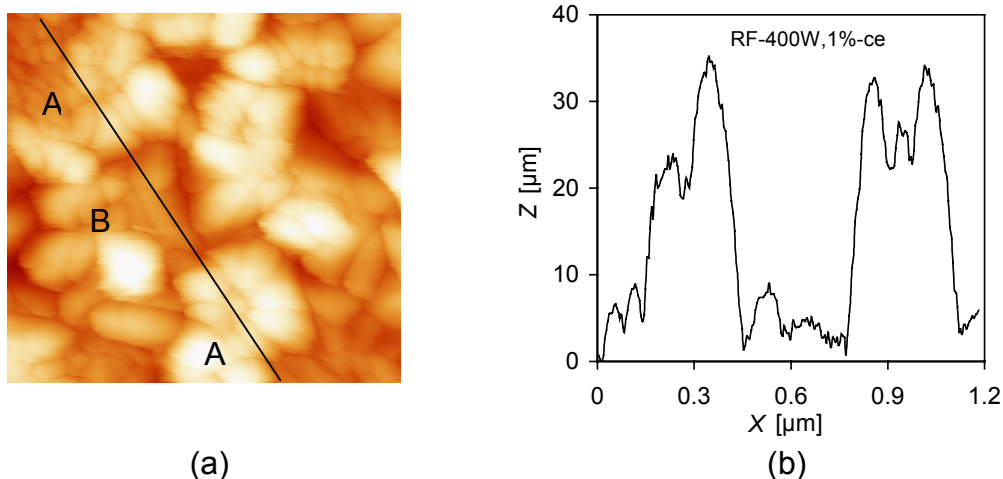
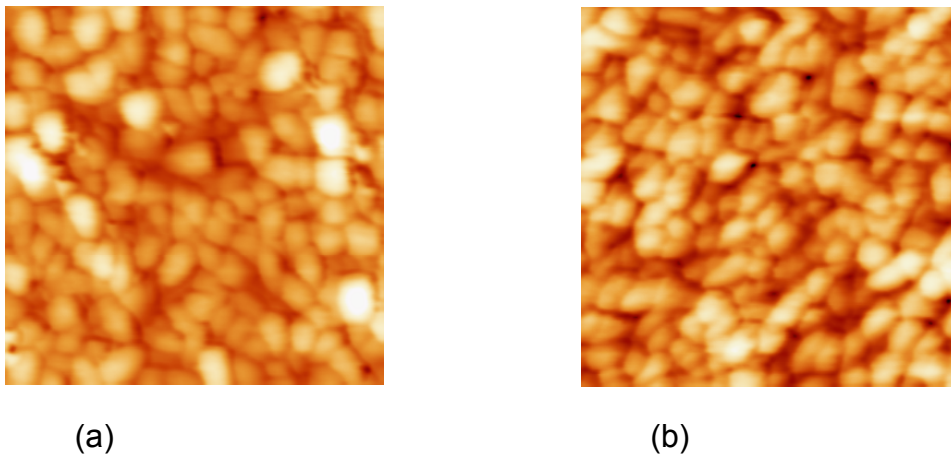


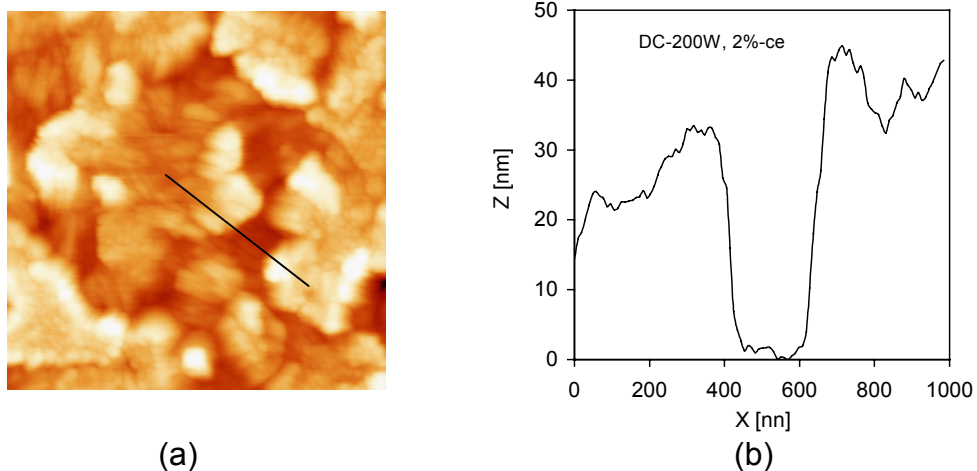
Figure 5-63 (a) AFM image ($1 \times 1 \mu\text{m}$) of central film prepared by rf 400 W at $q_{\text{O}_2} = 0\%$ (b) the profile along the direction shown by the straight line in the AFM image

For the purpose of comparison, the AFM images of samples, deposited with $q_{\text{O}_2} = 1\%$ under rf 400 W and rf 100 W discharge power, are also shown in Figure 5-64. It is observed that the surface morphologies of these two samples are quite similar in spite of the different rf powers, which is very possible due to the similar microstructure revealed by the x-ray diffraction measurement where only the (211) and (222) orientations are observed, while the (440) orientation was absent. The different morphologies between the samples prepared with the same power but different q_{O_2} (see Figure 5-63 (a) and Figure 5-64 (a)) may also result from the existence and absence of the (440) orientation.



(a) (b)
Figure 5-64 *AFM images ($1 \times 1 \mu\text{m}$) of the ITO central films prepared with $q_{\text{O}_2} = 1\%$ by (a) rf 400 W and (b) rf 100 W*

AFM measurement revealed that the characteristic grain-subgrain structure also exists in dc-sputtered ITO films (see Figure 5-65).



(a) (b)
Figure 5-65 *(a) AFM image ($2 \times 2 \mu\text{m}$) of central film prepared by dc 200 W at $q_{\text{O}_2} = 2\%$ and (b) the profile along the direction shown by the straight line in the AFM image*

6 Conclusions

(1) Dielectric modeling of semiconductors and insulators:

ITO: Transmittance and reflectance spectra of $\text{In}_2\text{O}_3:\text{Sn}$ (ITO) thin films were simulated with simple and modified dielectric models. The films were regarded as homogeneous continuous medium and the fit parameters obtained should be regarded as effective optical constants. The main concludes are listed below.

- The dielectric function used is the sum of three types of electronic excitations: band gap transition, interband transitions into upper half of the conduction band, intraband transitions of free electrons. For the standard dielectric model, the OJL model (suggested by O'Leary, Johnson and Lim to model the band gap of amorphous silicon), a harmonic oscillator and the Drude term were used to account for the above three transitions.
- The experimental plasma edge cannot be represented by the classical Drude formula. A frequency-dependent damping has to be introduced allowing for a relatively lower damping constant above the Drude frequency. With this alteration, the simulated spectra fit the experimental ones with an average error of about 0.3%.
- Both the optical mobility and carrier density are found to be higher than those of the respective electric parameters. These discrepancies are attributed to a pronounced microstructure with badly conducting grain boundaries.
- The ratio of the optically determined thickness and that obtained by profilometry is 0.95(3) for the extended Drude formula. Ratios smaller than 1 are physically meaningful because the stylus measures the top height, whereas the optical interferences average over the roughness of the film surface. The standard deviation (the number in parentheses) is an indicator of the quality of the fit.
- The band gap increases with increasing carrier density due to the Burstein-Moss shift. The refractive index at 550 nm decreases with increasing carrier density because both the band edge and the plasma edge shift towards to higher energy.

STO: Transmittance spectra of thin SrTiO₃ (STO) films prepared with different substrate temperature and sputtering power were simulated with simple and modified dielectric models.

- The concerned electron transitions for dielectrics are band gap transitions and interband transitions into the upper half of the conduction band. The standard dielectric function used for STO is the OJL model and harmonic oscillator.
- The simulation of samples with good crystallinity is worse than that of bad crystallinity. The fitting can be improved by adding an additional harmonic oscillator, i.e. introducing an additional absorption in the near infrared region. The physical meanings of the additional harmonic oscillators are not clear. They indicate probably that there are some localized states in the band gap.
- The better the crystallization the smaller the gamma and the band gap. The gamma represents the exponential tail states in the band gap. Therefore, for better crystallizing films, it is obviously to expect a smaller gamma. It has also been known that the construction of crystalline materials is closer, which could result in a smaller band gap.

TiO₂: Transmittance spectra of evaporated and sputtered thin TiO₂ films were simulated with simple and modified dielectric models.

- (The first point is the same as STO.)
- The band gap of evaporated samples is similar to that for sputtered ones. The evaporated samples have less sharp band edge.
- The fitting can be improved by adding an additional harmonic oscillator or a simple Drude model. The reason is that there probably exist some metal atoms of Ti in the films which could contribute free electrons in the conduction band. This case would occur quite probably in an oxygen-deficient ambient.

(2) Correlation of lattice distortion with structure and properties of ITO films

In this section, some empirical relationships between lattice distortion $\Delta d/d_0$, electron density N_{Dr} and mobility M_{Dr} , and grain size of ITO films have been established. The key parameter is the concentration of interstitial oxygen [O_i]. Oxygen interstitials act as electron traps and generate strain in the films. By comparing N_{Dr} with $\Delta d/d_0$, it is possible to derive an empirical relationship between [O_i] and $\Delta d/d_0$ when it is assumed that every O_i captures two electrons. Another result that could be concluded is that there are two sources attributing to the line

broadening of XRD reflections for our ITO films, i.e. finite grain size and inhomogeneous strains (also called microstrains).

Simultaneously, the following conclusions are obtained.

- The magnitude of the lattice expansion can be used to estimate the concentration of interstitial oxygen ($[O_i] = 0.5 \times 10^{21} \text{ cm}^{-3} \frac{(\Delta d / d_0)}{1\%}$).
- The lattice expansion decreases with increasing temperature. At low temperature, lattice distortion is higher for the higher oxygen partial pressure.
- The distortion of (100)-oriented grains, obtained from the (400)-peak, is always the smallest.
- The inhomogeneous strains increase with increasing lattice distortion (also called uniform strain or macrostrain).
- The grain size depends on the crystalline orientation: grains with orientation (211), (400) or (411) are always the largest. D_g decreases with increasing $\Delta d/d_0$, indicating that the formation of grain boundaries is driven by the stress in the films.
- The electrical conductivity of the films is determined by $[O_i]$ because interstitial oxygen both captures free electrons and scatters the remaining conduction electrons.
- The domain structure, which is a characteristic structure of sputtered films (the typical size of a domain is several hundreds nanometers, which is composed of many subgrains with the same crystallographic orientation), is suppressed by $[O_i]$.
- Scattering takes place at ionized donors and $\text{Sn}^*_{2\text{O}_i}$ -complexes.
- The refractive index in the visible range decreases linearly with N_{Dr} due to the Burstein-Moss (BM) shift of the band gap and the strength of the plasma oscillations that are both determined by N_{Dr} .

(3) Effect of sputter geometry and plasma distribution on the structural and electrical properties of ITO films

We have investigated the structure and properties of thin ITO films grown at the position centrally and peripherally above the target. The experimental results can be explained by the influence of plasma distribution under the substrate holder and the columnar structure resulting from the oblique particle incidence. The main results are concluded as following:

- The thickness profile for central films is homogeneous while it decreases linearly along the direction away from the target centre for periphery. The deposition rate for central samples is also larger than that for peripheral samples because of the effect of sputter geometry.
- The lattice of the films is generally expanded. In peripheral samples, the lattice expansion is bigger and (222)-grains are less frequent or very small. Grains with this orientation are the least resistant against resputtering. We conclude that more oxygen is incorporated and more resputtering takes place at oblique particle incidence. The other reason is due to the peripheral samples exposed to the plasma (above the erosion track) which could lead to bombardment with energetic particles and thus suppresses the (222) orientation. The electrical resistivity increase with increasing lattice expansion, i.e. concentration of interstitial oxygen, because interstitial oxygen captures electrons.
- The packing density of peripheral samples is smaller than the crystalline mass density and decreases with increasing oxygen partial pressure. This is attributed to a columnar microstructure arising from shadowing effects at oblique particle incidence. For the central films, packing density reaches the crystalline value because the isotropic particle flux prevents the formation of a columnar microstructure.

(4) Effect of film thickness

The effect of film thickness on the microstructure, the optical and electrical properties and the surface morphology of ITO samples has been investigated extensively. All these properties show a significant change at about 0.3 - 0.5 μm thickness. Films with thickness below 0.4 μm are named “thin”, further on; the others are named “thick”.

In the range of 0.4 to 1.4 μm , the films exhibit a mass density close to the crystalline value, small lattice distortion, similar texture of crystalline orientation, high free electron density and mobility, and a band gap of about 4.1 eV. Films that are thinner than 0.4 μm do not exhibit such favorable properties. We attribute the differences in the properties of the thin and thick films to a change of the films microstructure taking place at 0.3 - 0.5 μm . The main results are concluded as following:

- The deposition rate and packing density increase with increasing film thickness. Based on the experimental results and analyses on the film growth and microstructure, we suggest that the thick films consist of two layers, where the underlayer is looser and the top-layer is denser.

- For thick samples, the texture is independent of the layer thickness. An equidistribution of many orientations is observed with (400), (622) and (611) being the more prominent ones. While for thin films, only (400) and (222) orientations are observed. It is observed that the growth of the (222)-grains is suppressed with the increasing film thickness.

We infer that the low deposition rate contributes to more oxygen subplantation into the film structure which, leading to the favor growth of (222)-grains. As the deposition rate increases the film has the preferred orientation along the (400) direction. In return, the change in orientation from (222) to (400) also influences the deposition rate because the (400)-orientation is the most resistant against resputtering.

- The lattice distortion for thin films and peripheral samples are larger than that for thick and central samples, respectively. The grain size generally increases with increasing film thickness and there is a step between 0.3 and 0.4 μm .
- The surface roughness increases with increasing film thickness. And the surface roughness of central samples is larger than that of peripheral samples.

(5) Comparison of the dc- and rf-sputtered films

In order to investigate the effect of the mechanisms of the plasma excitation, i.e. dc and rf mode, on the properties of ITO films, the properties of the dc- and rf-sputtered samples deposited under the comparable conditions are compared and analysed.

- The deposition rate for rf sputtering is significantly lower than that of dc sputtering under the condition of constant discharge power, which can be interpreted in terms of the lower discharge voltage V_{dis} on the target for an rf magnetron discharge compared to a dc sputtering process. The deposition rate for rf sputtering does not decrease with increasing sputtering pressure as for dc sputtering.
- At the same q_{O_2} , the rf-sputtered films have a lower carrier density than dc-sputtered films which have the similar deposition rate. This can be explained by more oxygen incorporation in rf-sputtered films compared to dc-deposited films. It has also been observed that the carrier density increases with increasing rf power. It is interpreted that higher rf power leads to bigger deposition rate and, consequently, relative less oxygen incorporation.

The band gap decreases with increasing q_{O_2} , which obeys the Burstein-Moss (BM) shift. Generally, the carrier mobilities decrease with q_{O_2} , but there are

also some exceptions. The conductivities follow the same tendency with the q_{O_2} as the carrier density.

- The predominant orientation of rf-sputtered films is (222), instead of the (400) orientation for dc-sputtered films. At low rf power the (400) orientation is completely missing. The differences of the crystalline orientation between the rf- and dc-sputtered ITO films is inferred to be due to the growing films impinged by particles with lower energy and the effect of more efficient oxidizing for rf-sputtered films compared to that for dc-sputtered films.
- There is no clear effect of oxygen partial pressure on the microstructure of the rf-sputtered films, while in the case of dc sputtering, the influence of oxygen partial pressure is very significant.
- Generally, the grain size decreases with increasing lattice distortion for dc as well as rf sputtering. For rf-sputtering, the lattice distortion and grain size for central and peripheral samples are closer compared to that of the dc sputtered samples. This could be explained by that the rf-plasmas are more extended, while the dc-plasmas are more localized. Further, ITO films possess similar grain size and lattice distortion under the condition of the similar deposition rate, regardless of the sputtering mode.
- Compared to dc sputtering, the lattice distortion and grain size for rf-sputtered samples under the different discharge powers are also quite close. This phenomenon can also be interpreted in terms of the different discharge mechanism between rf and dc excitation as follows. In a dc discharge, most of the energetic particles stem from the target surface (e.g. reflected neutral argon atoms or negative oxygen ions), while in an rf magnetron discharge, the largest part of the energetic particles has its origin in the plasma in front of the substrate. For rf-sputtering, the lattice distortion and grain size for central and peripheral samples are similar, whereas for dc-sputtering, the lattice distortion for peripheral samples is much larger and the corresponding grain size is smaller.
- The lattice distortion of (222) orientation is always the largest in the case of both dc and rf sputtering. The vertical grain size and the surface roughness increase with increasing packing density. And there is not a definite correlation between the vertical grain size and the lateral grain size.
- It is observed that there exists the characteristic surface morphology of grain-subgrain structure for sputtered films in both cases of dc and rf.

7 Summary

7.1 Summary (in English)

Indium tin oxide ($\text{In}_2\text{O}_3:\text{Sn}$ or ITO) is a well-known transparent conducting oxide (TCO). It is a highly degenerate n -type wide gap semiconductor which is produced by doping Sn atoms in In_2O_3 . They are widely used in a variety of electronic and optoelectronic fields. For typical high-quality ITO films, the transmittance is above 90% in the visible range and the electrical resistivity is below $200 \mu\Omega\text{cm}$.

So far, many techniques have been developed to prepare ITO films. Among them, the magnetron sputtering is more attractive and widely used due to its many advantages, such as controllability, high deposition rate and deposition of films at low temperature with good optical and electrical properties. And it is also well-known that both the microstructure and the physical properties of the films are strongly dependent on the deposition conditions, most significantly on substrate temperature, oxygen partial pressure, and the distance between the target and the substrate.

In ITO films, the free carriers come from two different mechanisms: substitutional tetravalent tin atom and divalent oxygen vacancies. In order to improve the resistivity of ITO films, both the free carrier density and mobility should be increased. It has been revealed that increasing the free carrier density via doping Sn is self-limiting practically because a portion of the tin are deactive at high doping level resulting from the formation of neutral defect (Sn_2O_4). Increasing the former also leads to an increase in the visible absorption. In heavily degenerate polycrystalline ITO films, the main scattering mechanisms limiting the carrier mobility are neutral scatter center and ionized donor impurities. The later one also gives the physical limitation of the carrier mobility.

Due to the complicated crystal structure, the electric band structure of ITO has not been discovered very clearly so far. However, it has been reported that both direct transitions and indirect transitions could take place. And the widening of the band gap with the increasing of carrier density, which is known as Burstein-Moss shift, has been verified by many authors.

The optical properties of a material is described by the complex dielectric function ($\varepsilon = \varepsilon_1 + i\varepsilon_2$) or complex refractive index ($\tilde{n} = n + ik$). The optical properties of

doped semiconductors in the spectral range of interest, 200 nm to 3 μm , are controlled by three types of electronic excitations: band gap transitions, interband transitions from the bulk of the valence band into the bulk of the conduction band, and intraband transitions of the electrons in the conduction band. In this work, the optical transmittance and reflectance of ITO, SrTiO_3 (STO) and TiO_2 films have been simulated based on the dielectric modeling using a commercial computer program SCOUT98. For ITO films, the standard dielectric model is composed of the OJL model (named after the three authors, used to model the band gap of amorphous silicon), a harmonic oscillator and the classical Drude term. While for STO and TiO_2 insulators the standard model consists of the OJL model and a harmonic oscillator. However, it has been found that the standard models are usually too simple to simulate these films. Therefore, in practice, the Drude model has to be modified with a frequency-dependent damping term to overcome the too strong absorption in the visible range and sometimes the OJL model should be replaced by the other band gap transition models to account for the crystalline films. Additionally, more harmonic oscillators and a Drude term would be also helpful sometimes for the simulation of insulating films.

From the simulation, the other properties of the films, such as carrier density and mobility, band gap and the effective mass of electron, could be derived as well. It has been found that both the optically derived carrier density and mobility are higher than those of the respective electrically derived parameters. This could be attributed to the microstructure of the films, namely, the badly conducting grain boundaries and electrically isolated grains. The optically determined thickness was always compared with that obtained by profilometry. The difference between them is generally less than 5% and the ratio is normally smaller than 1, which can be explained in terms of the measurement mechanisms of these two methods. The other result that has been observed is that the band gap increases with increasing carrier density, resulting from the Burstein-Moss shift.

In this work, ITO films were prepared with the von Ardenne Laboratory System LA 500S by dc and rf magnetron sputtering methods under different oxygen partial pressures, substrate temperatures, sputtering powers and pressures in order to investigate the effect of the deposition conditions on the films properties, furtherly, the correlations between the films properties and their microstructures. All samples were characterized by a comparator balance Sartorius C50, a Tencor P10 profilometer, a Perkin-Elmer Lambda-9 spectrometer, a Simens Me 200 CY2 x-ray diffractometer and four-point probe, some of them also with a Thermomicroscopes AutoProbe CP Research atomic force microscope.

It has been observed that the lattice distortion generally increases with increasing oxygen partial pressure and decreases with increasing substrate temperature. This can be explained by the model of oxygen incorporation into the crystal lattice of the bixbyite structure. The magnitude of the lattice expansion can be used to estimate the concentration of interstitial oxygen $[O_i]$ assumed that every O_i captures two electrons.

There are two sources attributing to the line broadening of XRD reflections, i.e. finite grain size and inhomogeneous strains (also called microstrains) in the films. Actually, it is not easy to separate them. And it is revealed that the line broadening arises from both sources for our ITO films. Furtherly, the inhomogeneous strains increase with increasing lattice distortion (also called uniform strain or macrostrain).

It is found that the grain size determined from the peak width by means of Scherrer formula decreases with lattice distortion increasing, i.e. with $[O_i]$ increasing. This is explained by segregation of superstoichiometric oxygen during deposition or post-annealing into grain boundaries. More grain boundaries are formed when the initial concentration of interstitials is higher. The grain size depends on the crystalline orientation: grains with orientation (211), (400) or (411) are always the largest.

On the other hand, as oxygen incorporates into the films, the optical and electrical properties of the films would also be changed. The carrier density and mobility decrease with increasing $[O_i]$ because interstitial oxygen both captures free electrons and scatters the remaining conduction electrons, which results in the decrease of electrical conductivity. And it is concluded that the scattering centers of our polycrystalline ITO films are ionized donors and $Sn^*_2O_i^-$ -complexes. The refractive index in the visible range decreases linearly with N_{Dr} due to the shift of band edge (Burstein-Moss shift) and plasma edge.

Sputtered ITO films often exhibit a domain-subgrain structure where all subgrains in a domain (of about 500 nm diam) have the same crystallographic orientation. The altitude of the domains depends on the orientation of their subgrains: for (400) it is bigger than for (222) which was explained by orientation dependent resputtering. It has been found in this work that the domain structure is suppressed by $[O_i]$.

The effect of sputter geometry and plasma distribution on ITO films was studied in this work. In every run, two quartz substrates were always prepared simultaneously, one substrate ("central") above the center and the other one ("peripheral") above the erosion track on the target. And it is found that the

structural and electrical properties of these two samples are quite different. The thickness profile of central films is much more homogenous compared with peripheral one, resulting from the different distribution of the direction of the particle fluxes that can reach these two places. This also explains a lower deposition rate for peripheral samples. The packing density of peripheral films is less than that of central films which is attributed to a columnar microstructure arising from shadowing effects at oblique particle incidence. For the central films, packing density reaches the crystalline value because the isotropic flux prevents pores.

The lattice distortion for peripheral samples is always larger than that for central samples, which indicates more oxygen interstitials in peripheral films. This may be due to the direct effect of plasma. Because the peripheral sample is just above the erosion track, the oxygen there is more active and therefore, easy to implant into the films. The texture of the peripheral samples also differs from that of the central samples: grains with (222)-orientation are absent or very small and broad. This could be due to the more bombardments for the peripheral films. It has also been observed a shift from (400) to (222) with oxygen admixture to the sputter gas increasing, which has been reported by other authors.

It was found that there exists a critical film thickness ($\sim 0.5 \mu\text{m}$) in terms of the film growth and the structural and physical properties of ITO films. Above the critical thickness, films exhibit a mass density close to the crystalline value, small lattice distortion, similar texture of crystalline orientation, high free electron density and mobility, and a band gap of about 4.1 eV. On the contrary, films which are thinner than this thickness do not exhibit such favorable properties. The grain size increases with film thickness increasing. The rms surface roughness increases with grain size increasing and is larger for central films. Based on the x-ray diffraction studies, it is inferred that the (222)-oriented grains only grow when the film is below the critical thickness. The results can be interpreted by more oxygen incorporation at the initial of film growth. According to these findings, a guidance to prepare a high quality for thin ITO films is suggested, namely, reducing the oxygen partial pressure at the beginning of the deposition to prevent from over oxygen implantation into the films.

In this work, the effect of the plasma excitation mode, i.e. dc and rf sputtering has been investigated. It was observed that the deposition rate for rf sputtering is significantly lower than that of dc sputtering, which can be interpreted in terms of the lower discharge voltage V_{dis} on the target for an rf magnetron discharge compared to a dc sputtering process. At the same q_{O_2} , the rf-sputtered films have a lower carrier density than dc-sputtered films which have the similar deposition

rate. This can be explained by more oxygen incorporation arising from the excited oxygen in rf plasma.

The predominant orientation of rf-sputtered films is (222), instead of the (400) orientation for dc-sputtered films. And contrary to dc sputtering, there is no clear effect of oxygen partial pressure on the microstructure of the rf-sputtered films. These results are attributed to the growing films impinged by particles with lower energy and the effect of more efficient oxidizing for rf-sputtered films compared to that for dc-sputtered films.

For rf-sputtering, the lattice distortion and grain size for central and peripheral samples are closer compared to dc sputtered samples. This could be explained by that the rf-plasmas are more extended, while the dc-plasmas are more localized

Compared to dc sputtering, the lattice distortion and grain size for rf-sputtered samples under the different discharge powers are also quite close. This phenomenon can also be interpreted in terms of the different discharge mechanism between rf and dc excitation as follows. In a dc discharge, most of the energetic particles stem from the target surface (e.g. reflected neutral argon atoms or negative oxygen ions), while in a rf magnetron discharge, the largest part of the energetic particles has its origin in the plasma in front of the substrate.

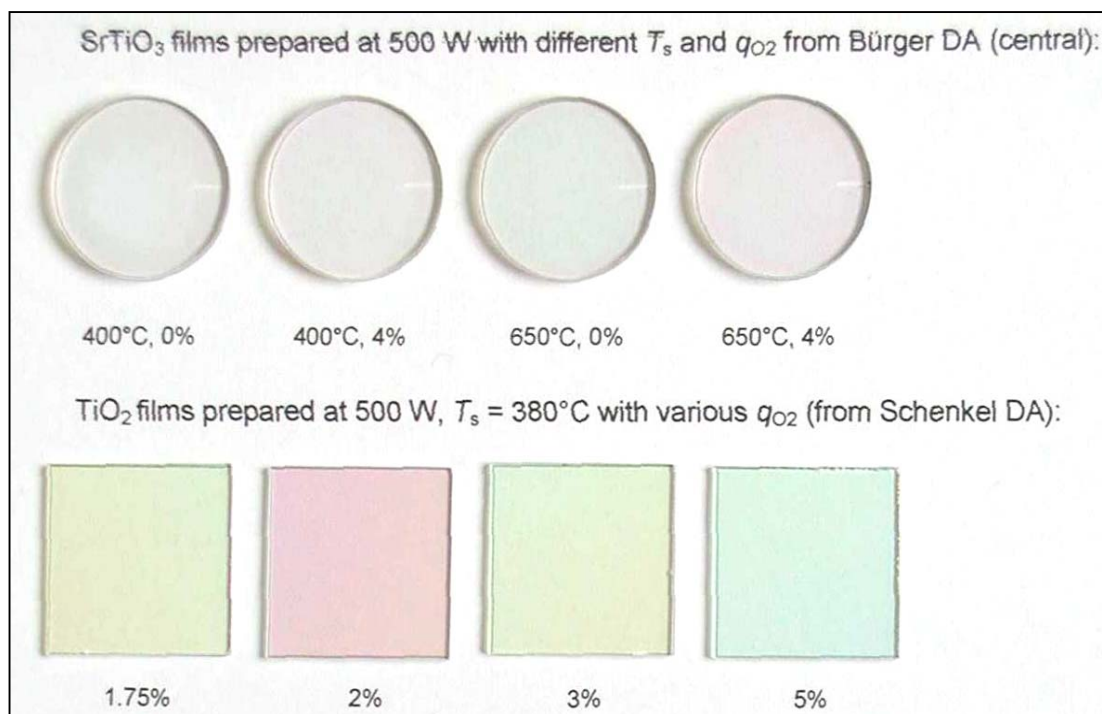


Figure 7-1 The photo of SrTiO₃ and TiO₂ thin films

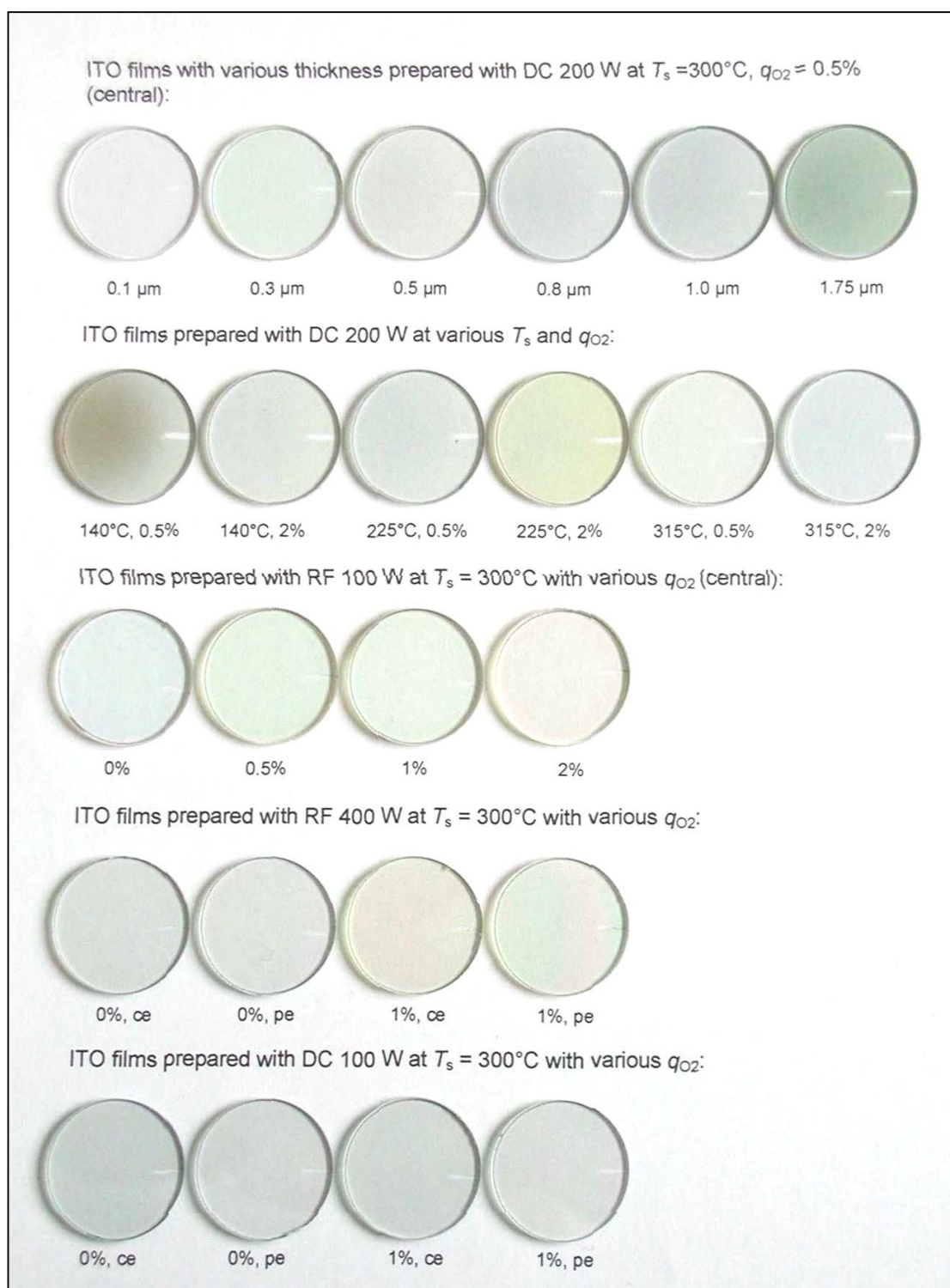


Figure 7-2 The photo of ITO thin films

7.2 Zusammenfassung (in German)

Indiumzinnoxid ($\text{In}_2\text{O}_3:\text{Sn}$ oder ITO) ist ein gut bekanntes transparentes leitfähiges Oxid (TCO). Hierbei handelt es sich um einen hoch degenerierten n -Halbleiter mit weiter Bandlücke, der durch Dotieren von Sn-Atomen in In_2O_3 hergestellt wird. Es wird in einer Vielzahl von elektronischen und optoelektronischen Bereichen eingesetzt. Für eine typische hochqualitative ITO-Schicht, ist die Transmission im sichtbaren Bereich über 90% und der elektrische Widerstand ist unter $200 \mu\Omega\text{cm}$.

Bis jetzt wurde eine Vielzahl von Verfahren entwickelt, um ITO-Schichten herzustellen. Unter ihnen ist Magnetronspalter, wegen seiner vielen Vorteile wie Kontrollierbarkeit, hoher Abscheiderate und niedriger Substrattemperatur bei guter optischen und elektrischen Eigenschaften, am attraktivsten und am weitesten verbreitet. Ebenso ist bekannt, dass sowohl die Mikrostruktur als auch die physikalischen Eigenschaften der Schichten stark von den Abscheidebedingungen abhängen, insbesondere von der Substrattemperatur, dem Sauerstoffpartialdruck und dem Abstand von Substrat und Target.

In ITO-Filmen treten freie Ladungsträger durch zwei verschiedene Mechanismen auf: Substitutionale tetravalente Zinnatome und divalente Sauerstoffleerstellen. Um den Widerstand von ITO-Schichten zu verringern sollten sowohl die Dichte der freien Ladungsträger als auch deren Mobilität erhöht werden. Es wurde festgestellt, dass die Erhöhung der Dichte der freien Ladungsträger durch das Dotieren mit Zinn praktisch selbstlimitierend ist, weil ein Teil der Zinnatome bei hohen Dotierungen durch die Bildung von neutralen Defekten (Sn_2O_4) deaktiviert wird. Eine Erhöhung dieser Defekte führt auch zu einem Anstieg der Absorption im Sichtbaren. In besonders degenerierten polykristallinen ITO-Schichten, wird die Mobilität der Ladungsträger hauptsächlich durch neutrale Streuzentren und ionisierte Donator Verunreinigungen eingeschränkt. Letztere sind auch die physikalische Grenze der Ladungsträgermobilität.

Wegen der komplizierten Kristallstruktur, ist die elektrische Bandstruktur von ITO bis jetzt nicht ganz geklärt. Es wurde aber berichtet, dass sowohl direkte als auch indirekte Übergänge stattfinden können. Und die Verbreiterung der Bandlücke durch eine Erhöhung der Dichte der freien Ladungsträger, als Burstein-Moss-Verschiebung bekannt, wurde von vielen Autoren verifiziert.

Die optischen Eigenschaften eines Materials werden durch die komplexe dielektrische Funktion ($\varepsilon = \varepsilon_1 + i\varepsilon_2$) oder den komplexen Brechungsindex ($\tilde{n} = n + ik$) beschrieben. Die optischen Eigenschaften eines dotierten Halbleiters im Spektralbereich von 200 nm bis 3 μm werden durch drei Typen elektronischer Anregung bestimmt: Bandlückenübergänge, Zwischenbandübergänge, die vom

Inneren des Valenzbandes ins Innere des Leitungsbandes führen und Innerbandübergänge der Elektronen im Leitungsband. In dieser Arbeit wurde die optische Transmission und Reflexion von ITO-, SrTiO₃- (STO) und TiO₂-Schichten auf der basis von dielektrischen Modellen mit dem kommerziellen Computerprogramm SCOUT 98 simuliert. Für ITO-Schichten wurde das dielektrische Standardmodell aus einem OJL-Modell (bennant nach den drei Autoren, beschreibt die Bandlücke im amorphen Silizium), einem harmonischen Oszillator und einem klassischen Drudetherm zusammengefügt. Während für STO- und TiO₂-Nichtleiter das dielektrische Standardmodell aus einem OJL-Modell und einem harmonischen Oszillator besteht. Es hat sich jedoch herausgestellt, das die Standardmodelle für die Simulation dieser Schichten zu einfach sind. Dadurch muss in der Praxis das Drudemodell mit einem frequenzabhänigen Dämpfungstherm modifiziert werden um eine zu starke Absorption im sichtbaren Bereich zu verhindern und manchmal muss das OJL-Modell durch ein anderes Bandübergangsmodell ersetzt werden um der Kristallinität der Schichten Rechnung zu tragen. Zusätzlich, können auch mehrere harmonische Oszillatoren und ein Drudetherm nützlich sein, um nichtleitende Schichten zu simulieren.

Durch die Simulation können auch die anderen Eigenschaften der Schichten, wie Ladungsträgerdichte und Mobilität, Bandlücke und die effektive Masse der Elektronen bestimmt werden. Es stellte sich heraus, dass sowohl die optisch bestimmte Ladungsträgerdichte als auch deren Mobilität höher waren als die entsprechenden elektrisch bestimmten Parameter. Dies kann der Mikrostruktur der Schichten zugeschrieben werden, namentlich den schlecht leitenden Korngrenzen und den elektrisch isolierten Körnern. Die optisch bestimmte Schichtdicke wurde immer mit Profilometermessungen verglichen. Der Unterschied zwischen beiden ist immer unter 5% und das Verhältnis ist normalerweise kleiner als 1. Dies kann durch Eigenheiten der beiden Messmethoden erklärt werden. Hervorgerufen durch die Burstein-Moss-Verschiebung steigt die Energie der Bandlücke mit der Erhöhung der Dichte der freien Ladungsträger.

In dieser Arbeit, wurden ITO-Schichten mit einer von Ardenne Laboratory System LA 500S durch DC- und RF-Magnetronsputtermethoden mit unterschiedlichen Sauerstoffpartialdrücken, Substrattemperaturen, Sputterleistungen und Drücken hergestellt um den Einfluss der Abscheidebedingungen auf die Schichteigenschaften zu untersuchen. Desweiteren wurde die Korrelation zwischen Schichteigenschaften und ihrer Mikrostruktur ermittelt. Alle Proben wurden mit einer Komparatorwaage "Sartorius C50", einem "Tencor P10"

Profilometer, einem "Perkin-Elmer Lambda-9" Spektrometer einem "Simens Me 200 CY2" Röntgendiffraktometer, und einer elektrischen Vierpunktsonde untersucht. An einigen Proben wurden zusätzlich AFM-Untersuchungen mit einem "Thermomicroscopy AutoProbe CP Research" AFM durchgeführt.

Es wurde beobachtet, dass die Gitterverzerrungen i.a. mit steigendem Sauerstoffpartialdruck stärker werden und mit ansteigender Substrattemperatur abnehmen. Dieses kann durch das Modell des Sauerstoffeinbaus in das Kristallgitter der Bixbyite Struktur erklärt werden. Der Grad der Gitterverzerrung kann zur Abschätzung der Konzentration von Sauerstoff auf Zwischengitterplätzen $[O_i]$ herangezogen werden, wenn man annimmt, dass auf jedes O_i zwei Elektronen übertragen werden.

Es gibt zwei Eigenschaften, die man mit der Linienverbreiterung von XRD Reflexen in Verbindung bringt, und zwar die endliche Korngrösse und inhomogene Verzerrungen (micro-Verzerrung) in den Schichten. Im Allgemeinen ist es schwer diese beiden auseinanderzuhalten. Und es hat sich gezeigt, dass die Linienverbreiterung durch beide Einflüsse für unsere ITO Schichten ansteigt. Desweiteren nehmen die inhomogenen Verzerrungen mit ansteigender Gitterverzerrung (macro-Verzerrung) zu.

Es wurde festgestellt, dass die Korngrösse, die mit Hilfe der Scherrer Formel aus der Halbwertsbreite ermittelt wurde mit steigender Gitterverzerrung, d.h. mit steigender $[O_i]$ kleiner wird. Dieses wird erklärt durch die Abscheidung von überstöchiometrischem Sauerstoff in die Korngrenzen während der Beschichtung oder beim nachträglichen Ausheizen. Wenn die anfängliche Konzentration von $[O_i]$ höher ist, werden mehr Korngrenzen gebildet. Die Korngrösse hängt auch von der Orientierung ab. Körner mit den Orientierungen (211), (400) oder (411) sind immer die grössten.

Auf der anderen Seite werden auch die optischen und elektrischen Eigenschaften der Schichten verändert, wenn Sauerstoff in die Schichten eingebracht wird. Die Ladungsträgerdichte und -mobilität nimmt mit steigender $[O_i]$ ab, weil Sauerstoff auf Zwischengitterplätzen sowohl freie Elektronen einfängt als auch die verbleibenden Leitungselektronen streut, was zur Abnahme der elektrischen Leitfähigkeit führt. Daraus wird geschlossen, dass die Streuzentren in unseren polykristallinen ITO Schichten ionisierte Donatoren und $Sn^*_2O_i$ Komplexe sind.

Der Brechungsindex im sichtbaren Bereich nimmt in linearer Abhängigkeit mit N_{Dr} ab, dieses wird hervorgerufen durch eine Verschiebung der Bandkante (Burstein-Moss Verschiebung) und der Plasmakante.

Gesputterte ITO-Schichten zeigen oft eine Struktur aus Domänen (von ungefähr 500nm Durchmesser), in der alle Körner dieselbe kristallographische Orientierung haben. Die Grösse der Domänen hängt von der Orientierung ihrer einzelnen Körner ab: Für (400) ist sie grösser als für (222). Dieses wird erklärt durch das von der Orientierung abhängige Rückspattern. In dieser Arbeit wurde festgestellt, dass die Domänenstruktur durch $[O_i]$ unterdrückt wird.

Der Effekt der Sputtergeometrie und der Plasmapverteilung auf ITO-Schichten wurde in dieser Arbeit ebenfalls untersucht. In jedem Experiment wurden zwei simultan präparierte Quarzsubstrate beschichtet. Ein Substrat ("central") über der Mitte und das zweite ("peripheral") über dem Erosionsgraben des Targets. Und es wurde festgestellt, dass die strukturellen und elektrischen Eigenschaften ziemlich unterschiedlich sind. Das Schichtdickenprofil der mittigen Beschichtung ist im Vergleich zur Randbeschichtung wesentlich homogener. Dieses resultiert aus der unterschiedlichen Verteilung der Richtungen der Teilchflüsse, die diese Orte erreichen können. Das erklärt auch die niedrige Abscheiderate für die Randschichten. Die Packungsdichte der Randschichten ist niedriger als die der mittleren Schichten. Das wird durch eine zunehmende columnare Mikrostruktur, die durch Abschattungseffekte bei schrägem Partikeleinfall hervorgerufen wird, erklärt. Für die Schichten aus der Mitte erreicht die Packungsdichte kristallines Niveau, weil der isotropische Fluss eine Porenbildung verhindert.

Die Gitterverzerrung für die Randproben ist immer grösser, als die der mittleren Proben, was als Anzeichen für einen höheren Sauerstoffgehalt auf Zwischengitterplätzen im Falle der Randschichten gesehen wird. Dieses könnte ein direkter Effekt des Plasmas sein. Weil die Randprobe genau über dem Erosionsgraben liegt und der Sauerstoff dort aktiver ist, wird er dadurch einfacher in die Schichten eingebaut. Die Textur der Randproben unterscheidet sich ebenfalls von der der mittleren Probe: Körner mit (222)-Orientierung sind nicht vorhanden oder im XRD-Spektrum kaum zu sehen. Dieses kann mit dem verstärkten Bombardement der Randschichten zusammenhängen. Auch die von anderen Autoren berichtete Texturverschiebung von (400) nach (222) durch Abnahme des Sauerstoffgehalts im Sputtergas wurde beobachtet.

Es wurde herausgefunden, dass eine kritische Schichtdicke ($\sim 0.5\mu\text{m}$) in bezug auf Schichtwachstum und die strukturellen und physikalischen Eigenschaften von ITO Schichten existiert. Oberhalb dieser kritischen Schichtdicke zeigen diese Schichten eine Massendichte nahe den kristallinen Werten, geringe Gitterverzerrungen, gleiche Textur der kristallinen Orientierungen, eine hohe Dichte und Mobilität freier Elektronen und eine Bandlücke von 4.1eV. Im Gegensatz dazu zeigen dünnere Schichten, die unterhalb der kritischen

Schichtdicke liegen, nicht diese gewünschten Eigenschaften. Die Korngrösse wächst mit ansteigender Schichtdicke. Die Oberflächenrauigkeit steigt mit steigender Korngrösse und ist grösser für die mittleren Proben. Aus XRD Messungen lässt sich schliessen, dass die (222) orientierten Körner nur unterhalb der kristischen Schichtdicke wachsen. Diese Resultate können durch einen erhöhten Sauerstoffeinbau zu Beginn des Schichtwachstums interpretiert werden. Aufgrund dieser Feststellung kann eine Anleitung zur Herstellung von hochqualitativen, dünnen ITO-Schichten vorgeschlagen werden, nämlich die Reduzierung des Sauerstoffpartialdrucks zu Beginn der Abscheidung, um einen zu hohen Sauerstoffeintrag in die Schichten zu verhindern. In dieser Arbeit wurde der Effekt der Plasma-Anregung, d.h. DC und RF Sputtern untersucht. Es wurde beobachtet, dass die Abscheiderate für RF-Sputtern signifikant niedriger liegt als für DC-Sputtern, was durch die niedrigere Entladungsspannung auf dem Target bei einer RF-Magnetron Entladung im Vergleich zu einem DC-Sputterprozess erklärt werden kann. Für denselben Sauerstofffluss haben RF gesputterte Schichten eine niedrigere Ladungsträgerdichte als DC gesputterte, die beide mit derselben Abscheiderate hergestellt wurden. Dieses kann durch den vermehrten Sauerstoffeinbau, verursacht durch den angeregten Sauerstoff im RF-Plasma, erklärt werden.

Die vorherrschende Orientierung für die RF-gesputterten Filme ist (222) im Gegensatz zur (400) Orientierung für DC gesputterte Schichten. Und im Gegensatz zum DC Sputtern gibt es keine klaren Effekte des Sauerstoffpartialdrucks auf die Mikrostruktur von RF gesputterten Schichten. Diese Resultate können wachsenden Filmen zugeschrieben werden, die sich aus Teilchflüssen mit niedrigen Energien abscheiden und dem Effekt der effizienten Oxidierung von RF gesputterten Filmen im Vergleich zu DC gesputterten.

Im Falle des RF-Sputterns liegen Gitterverzerrungen und Korngrössen für die mittlere und die Randprobe im Vergleich zu DC gesputterten Proben näher beieinander. Das kann dadurch erklärt werden, dass RF Plasmen ausgedehnter sind, während DC Plasmen lokalisierter sind.

Im Vergleich zum DC Sputtern sind die Gitterverzerrungen und Korngrössen für RF gesputterte Proben mit verschiedenen Entladungsleistungen ebenfalls nahe beieinander. Dieses Phänomen kann auch durch die unterschiedlichen Entladungsmechanismen von RF und DC Entladungen wie folgt interpretiert werden. In einer DC Entladung stammen die meisten energetischen Partikel von der Target-Oberfläche (z.B.: reflektierte neutrale Ar-Atome oder negative Sauerstoffionen), während in einer RF Magnetron Entladung der grösste Teil der energetischen Partikel seinen Ursprung im Plasma vor dem Substrat hat.

8 References

- Alam, A. H. M. Z. Saha, P. K. Hata, T. and Sasaki, K. (1999) High-rate reactive deposition of indium oxide films on unheated substrate using ozone gas. *Thin Solid Films* 352(1-2), pp. 133-137.
- Amaral, A. Brogueira, P. Nunes de Carvalho, C. and Lavareda, G. (2000) Early stage growth structure of indium tin oxide thin films deposited by reactive thermal evaporation. *Surface and Coatings Technology* 125, pp. 151-156.
- Behrisch, R. ed. (1983) *Topics in applied physics: Sputtering by particle bombardment II*. Vol. 47. Berlin, Heidelberg, New York, Springer-Verlag. ISBN = 3-540-12593-0.
- Behrisch, R. and Wittmaack, K. eds. (1991) *Topics in applied physics: Sputtering by particle bombardment III*. Vol. 64. Berlin, Heidelberg, New York, Springer-Verlag. ISBN = 3-540-53428-8.
- Bel Hadj Tahar, R. Ban, T. Ohya, Y. and Takahashi, Y. (1997) Optical, structural, and electrical properties of indium tin oxide thin films prepared by the sol-gel method. *J. Appl. Phys.* 82(2), pp. 865-870.
- Bel Hadja Tahar, R. Ban, T. Ohar, Y. and Takahashi, Y. (1998) Tin doped indium oxide thin films: Electrical properties. *J. Appl. Phys.* 83(5), pp. 2631-2645.
- Bellingham, J. R. Philips, W. A. and Adkins, C. J. (1992) Intrinsic performance limits in transparent conducting oxides. *J. Mater. Sci. Lett.* 11, pp. 263-265.
- Bender, M. Seelig, W. Daube, C. Frankenberger, H. Ocker, B. and Stollenwerk, J. (1998) Dependence of oxygen flow on optical and electrical properties of DC-magnetron sputtered ITO films. *Thin Solid Films* 326(1-2), pp. 72-77.
- Bender, M. and Trude, J. (1999) Deposition of transparent and conducting indium-tin-oxide films by the r.f.-superimposed DC sputtering technology. *Thin solid Films* 354(1-2), pp. 100-105.
- Binnig, G. Quate, C. F. Gerber, C. H. (1986) Atomic Force microscope. *Phys. Rev. Lett.* 56, pp. 930-933.
- Brune, D. Hellborg, R. Whitlow, H. J. and Hunderi, O. eds. (1997) *Surface characterization: A user's book*. Weinheim, WILEY-VCH Verlag GmbH. ISBN = 3-527-28843-0.

- Buchanan, M. Webb, J. B. and Williams, D. F. (1981) The influence of target oxidation and growth-related effects on the electrical properties of reactively sputtered tin-doped indium oxide. *Thin Solid Film* 80, pp. 373-383.
- Bunshah, R. F. Blocher, Jr. J. M. Mattox, D. M. Bonifield, T. D. McGuire, G. E. Fish, J. G. Schwartz, M. Ghate, P. B. Thornton, J. Jacobson, B. E. and Tucker, Jr. R. C. (1982) *Deposition technologies for films and coatings*. Park Ridge, New Jersey, U.S.A., Noyes Publications. ISBN = 0-8155-0906-5.
- Bürger, C. (2000) *Herstellung von $In_2O_3:Sn$ - und $SrTiO_3$ -Schichten mit Magnetron-Zerstäubung und deren mikrostrukturelle Charakterisierung*. Diploma Thesis, Universität GH Essen (in German).
- Burstein, E. (1954) Anomalous optical absorption limit in InSb. *Phys. Rev.* 93, pp. 632-633.
- Carl, K. Schmitt, H. and Friedrich, I. (1997) Optimization of sputtered ITO films with respect to the oxygen partial pressure and substrate temperature. *Thin Solid Films* 295(1-2), pp. 151-155.
- Chapman, B. (1980) *Glow discharge processes*. New York, John Wiley & Sons, Inc. ISBN = 0-471-07828-X.
- Choi, C.G. No, K. Lee, W.-J. Kim, H.-G. Jung, S.O. Lee, W.J. Kim, W.S. Yoon, C. and Kim, S.J. (1995) Effects of oxygen partial pressure on the microstructure and electrical properties of indium tin oxide film prepared by d.c. magnetron sputtering *Thin Solid Films* 258(1-2), pp. 274-278.
- Chopra, K. L. (1969) *Thin film phenomena*. New York, McGraw-Hill Book Company.
- Coutts, T. J. Perkins, J. D. Ginley, D. S. and Mason, T. O. (1999) Transparent conducting oxides: status and opportunities in basic research. *The 195th Meeting of the Electrochemical Society Seattle, Washington*.
- Deng, W. Ohgi, T. Nejo, H. and Fujita, D. (2001) Characteristics of indium tin oxide films deposited by DC and RF magnetron sputtering. *Jpn. J. Phys.* 40(5A), pp. 3364-3369.
- Dietrich, D. Schmalzbauer, K. Hoffmann, H. and Szczyrbowski, J. (1984) The effect of annealing on the optical properties of indium tin oxide films. *Thin Solid Films* 122, pp. 19-29.
- Ehl, G. (1997) *Wachstum, Mikrostruktur, elektrische und optische Eigenschaften von oxidischen Mehrschichten mit ITO-Elektroden*. Diploma Thesis, Universität GH Essen (in German).

- El Akkad, F. Marafi, M. Punnoose, A. and Prabu, G. (2000) Effect of substrate temperature on the structural, electrical and optical properties of ITO films prepared by rf magnetron sputtering. *Phys. Stat. Sol. (a)* 177, pp. 445-452.
- El Akkad, F. E. Punnoose, A. and Prabu, G. (2000) Properties of ITO films prepared by rf magnetron sputtering. *Appl. Phys. A* 71(2), pp.157-160.
- Ellmer, K. (2000) Magnetron sputtering of transparent conductive zinc oxide: relation between the sputtering parameters and the electronic properties. *J. Phys. D: Appl. Phys.* 33, pp. R17-R32.
- Fan, J. C. Bachner, F. J. and Foley, G. H. (1977) Effect of O₂ pressure during deposition on properties of rf-sputtered Sn-doped In₂O₃ films. *Appl. Phys. Lett.* 31, pp. 773-775.
- Fan, J. C. C. and Goodenough, J. B. (1977) X-ray photoemission spectroscopy studies of Sn-doped indium-oxide films. *J. Appl. Phys.* 48, pp. 3524-3531.
- Frank, G. Köstlin, H. (1982) Electrical properties and defect model of tin-doped indium oxide layers. *Appl. Phys. A*27, pp. 197-206.
- Galasso, F. S. (1970) *Structure and properties of inorganic solids*. Oxford New, York, Toronto, Sydney, Branschweig, Pergamon Press. pp. 90-102.
- Gersdorff, M. (1999) *Herstellung von ITO und SrTiO₃ Schichten durch Magnetron-Sputtern und deren Charakterisierung*. Diploma Thesis, Universität GH Essen (in German).
- Guittoum, A. Kerkache, L. and Layadi, A. (1999) Effective of thickness on the physical properties of ITO thin films. *The European Physical Journal: Applied Physice* 7, pp. 201-206.
- Gupta, L. Mansingh A. and Srivastava, P. K. (1989) Band gap narrowing and the band structure of tin doped indium oxide films. *Thin Solid Films* 176, pp. 33-44.
- Hamberg, H. Granqvist, C. G. (1989) Evaporated Sn-doped In₂O₃ films: Basic optical properties and applications to energy-efficient windows. *J. Appl. Phys.* 60(11), pp. R123-159.
- Hartmut, F. and Gerhard, K. eds. (1987) *Dünnschichttechnologie*. Düsseldorf, VDI-Verlag. ISBN = 3-18-400670-0 (in German).
- Higuchi, M. Uekusa, S. Nakano, R. and Yokogawa, K.(1993) Micrograin structure influence on electrical characteristics of sputtered indium tin oxide films. *J. Appl. Phys.* 74(11), pp. 6710-6713.

- Honda, S. Watamori, M. and Oura, K. (1996) The effects of oxygen content on electrical and optical properties of indium tin oxide films fabricated by reactive sputtering. *Thin Solid Films* 281-282(1-2), pp. 206-208.
- Hong, J. P. Kwak, J. S. and Kim, C. O. (2000) dielectric properties of pulsed-laser deposited SrTiO₃ films at microwave frequency ranges. *J. Appl. Phys.* 88(6), pp. 3592-3595.
- Hoon Yi, C. Shigesato, Y. Yasui, I. and Takakil, S. (1995) Microstructure of low-resistivity tin-doped indium oxide films deposited at 150 ~ 200°C. *Jpn. J. Appl. Phys.* 34(2B), pp. L244 – L247.
- Kamei, M. Shigesato, Y. and Takaki, S. (1995) Origin of characteristic grain-subgrain structure of tin-doped indium oxide films. *Thin Solid Films* 259(1), pp. 38-45
- Kim, H. Horwitz, J. S. Kushto, G. Piqué, A. Kafafi, Z.H. Gilmore, C.M. and Chrisey, D.B. (2000) Effect of the film thickness on the properties of indium tin oxide thin films. *J. Appl. Phys.* 88(10), pp. 6021-6025.
- Jarzębski, Z. M. (1982) Preparation and physical properties of transparent conducting oxide films. *Phys. Stat. Sol. (a)* 71(13), pp. 13-41.
- Jellison, Jr. G. E. (1998) Spectroscopic ellipsometry data analysis : measured versus calculated quantities. *Thin Solid Films* 313-314, pp. 33-39.
- Jerman, M. Optical workshop of Essen University Email: martin.jerman@uni-essen.de.
- Joshi, R.N. Singh, V.P. and McClure, J.C. (1995) Characteristics of indium tin oxide films deposited by r.f. magnetron sputtering. *Thin Solid Films* 257, pp. 32-35.
- Kane, J. Schweizer, H. P. and Kern, W. (1975) Chemical vapor deposition of transparent electrically conducting layers of indium oxide doped with tin. *Thin Solid Films* 29, pp. 155-163.
- Karasawa, T. Miyata, Y. (1993) Electrical and optical properties of indium tin oxide thin films deposited on unheated substrates by dc reactive sputtering. *Thin Solid Films* 233, pp. 135-139.
- Kikuchi, N. Kusano, E. Kishio, E. Kinbara, A. and Nanto, H. (2001) Effect of excess oxygen introduced during sputter deposition on carrier mobility in as-deposited and postannealed indium-tin-oxide films. *J. Vac. Sci. Technol. A* 19(4), pp. 1636-1641.

- Kim, C. C. Garland, J. W. Abad, H. and Raccah, P. M. (1992) Modeling the optical dielectric function of semiconductors: Extension of the critical-point parabolic-band approximation. *Physical Review B* 45(20), pp. 11749-11767.
- Kim, J. S. Granström, M. Friend, R. H. Johansson, N. Salaneck, W. R. Daik, R. Feast, W. J. Ohkana, K. and Hommel, D. (1998) Indium-tin oxide treatments for single and double-layer polymeric light-emitting diodes: The relation between the anode physical, chemical and morphological properties and the device performance. *J. Appl. Phys.* 84(12), pp. 6859-6870.
- Klabunde, K. J. ed. (1985) *Thin films from free atoms and particles*. Orlando, Academic Press, INC. ISBN = 0-12-410755-9.
- Kobayashi, H. Ishida, T. Nakamura, K. Nakato, Y. and Tsubomura H. (1992) Properties of indium tin oxide films prepared by the electron beam evaporation method in relation to characteristics of indium tin oxide/silicon oxide/silicon junction solar cells. *J. Appl. Phys.* 72(11), pp.5288-5293.
- Köstlin, H. Jost, R. and Lems, W. (1975) Optical and electrical properties of doped In_2O_3 . *Phys. Stst. Sol. (a)*29, pp.87-93.
- Korobov, V. Leibovitch, M. and Shapira, Y. (1993) Indium oxide Schottky junctions with InP and GaAs. *J. Appl. Phys.* 74(5), pp. 3251-3256.
- Kovac, A. (2002) Department of mathematics and information of University Essen, Statistics group. Email: Kovac@ikarus.stat-math.uni-essen.de.
- Kubota, E. Shigesato, Y. Igarashi, M. Haranoh, T. and Suzuki, K. (1994) Effects of magnetic field gradient on crystallographic properties in tin-doped indium oxide films deposited by electron cyclotron resonance plasma sputtering. *J. Appl. Phys.* 33(9A), pp. 4997-5004.
- Kulkarni, A. K. and Knickerbocker, S. A. (1996) Estimation and verification of the electrical properties of indium tin oxide based on the energy band diagram. *J. Vac. Sci. Technol. A* 14(3), pp.1709-1713.
- Kumar, C. V. R. V. and Mansingh, A. (1989) Effect of target-substrate distance on the growth and properties of rf-sputtered indium tin oxide films. *J. Appl. Phys.* 65(3), pp. 1270-1280.
- Latz, R. Michael, K. and Scherer, M. (1991) High conducting large area indium tin oxide electrodes for displays prepared by DC magnetron sputtering. *Jpn. J. Appl. Phys.* 30(2A), pp. L149-L151.
- Latz, R. Daube, C. Haranou, T. Ocker, B. and Suzuki, K. (1997) Microwave plasma assisted sputtering. *Journal of Non-Crystalline Solids* 218, pp. 329-334.

- Lesaiherre, P.-Y. Yamaguchi, H. Miyasaka, Y. Watanabe, H. Ono, H. and Yoshida, M. (1995) SrTiO₃ thin films by MOCVD for 1 Gbit DRAM application. *Integrated Ferroelectrics* 8, pp. 201-225.
- Löbl, P. Huppertz, M. and Mergel, D. (1994) Nucleation and growth in TiO₂ films prepared by sputtering and evaporation. *Thin Solid Films* 251, pp. 72-79.
- Löbl, P. Huppertz, M. and Mergel, D. (1996) ITO films for antireflective and antistatic tube coatings prepared by dc magnetron sputtering. *Surf. Coat. Techn.* 82(1-2), pp. 90-98.
- Mader, S. (1970) Determination of structures in films. In: Maissel, L. I. and Glang, R. eds. *Handbook of thin film technology*. New York, McGraw-Hill Book Company.
- Martinez, G. (1993) The optical response of semiconductors: An overview. In: Martinez, G. ed. *Optical properties of semiconductors*. Dordrecht, Boston, London, Kluwer Academic Publishers.
- McMeeking, G. D. (2000) *Techniques for the deposition of optimum tin-doped indium oxide films*. Research Report. Chicago U.S.A.
- Meng, L.-J. and Dos Santos, M. P. (1996) Structure effect on electrical properties of ITO films prepared by RF reactive magnetron sputtering. *Thin Solid Films* 289(1-2), pp. 65-69.
- Meng L.-J. and Dos Santos, M. P. (1997) Properties of indium tin oxide (ITO) films prepared by r.f. reactive magnetron sputtering at different pressures. *Thin Solid Films* 303(1-2), pp.151-155.
- Meng, L.-J. and Dos Santos, M. P. (1998) Properties of indium tin oxide films prepared by rf reactive magnetron sputtering at different substrate temperature. *Thin Solid Films* 322(1-2), pp. 56-62.
- Meng, L.-J. and Dos Santos, M. P. (2000) Influence of the target-substrate distance on the properties of indium tin oxide films prepared by radio frequency reactive magnetron sputtering. *J. Vac. Sci. Technol. A* 18(4), pp. 1668-1671.
- Mergel, D. Buschendorf, D. Eggert, S. Grammes, R. and Samset, B. (2000a) Density and refractive index of TiO₂ films prepared by reactive evaporation. *Thin Solid Films* 371 (1-2), pp. 218-224.
- Mergel, D. Stass, W. Ehl, G. and Barthel, D. (2000) Oxygen incorporation in thin films of In₂O₃:Sn prepared by radio frequency sputtering. *J. Appl. Phys.* 88(5), pp. 2437-2442.
- Mergel, D. Schenkel, M. Ghebre, M. and Sulkowski, M. (2001) *Thin Solid Films* 392(1), pp. 91-97.

- Mergel, D. (2001) Modeling thin TiO₂ films of various densities as an effective optical medium. *Thin Solid Films* 397(1-2), pp. 216-222.
- Mergel, D. and Qiao, Z. (2002) Dielectric modeling of optical spectra of thin In₂O₃:Sn films. *J. Phys. D: Appl. Phys.* 35, pp. 794-801.
- Mientus, R. and Ellmer, K. (2001a) In situ investigation by energy dispersive x-ray diffraction (EDXRD) of the growth of magnetron sputtered ITO films. *Surface and Coating Technology* 142-144, pp. 748-754.
- Mientus, R. and Ellmer, K. (2001) Reactive magnetron sputtering of tin-doped indium oxide (ITO): influence of argon pressure and plasma excitation mode. *Surface and coating Technology* 142-144, pp. 748-754.
- Montserrat, E. Boy, P. and Marcel, C. (1998), Communication at the 1998 Optical Interference Coatings conference.
- Moss, T. S. (1954) The interpretation of the properties of indium antimonide. *Proc. Phys. Soc. London, Sect. B*67, p. 775-782.
- Movchan, B. A. and Demchishin, A. V. (1969) Investigation of the structure and properties of thick vacuum- deposited films of nickel, titanium, tungsten, alumina and zirconium dioxide. *Phys. Met. Metallogr.* 28(83) pp. 653-660.
- Nadaud, N. Lequeux, N. Nanot, M. Jové, J. and Roisnel, T. (1998) Structural studies of tin-doped indium oxide (ITO) and In₄Sn₃O₁₂. *J. Solid State Chem.* 135, pp. 140-148.
- Nam, S.-H. and Kim, H.-G. (1992) The effect of heat treatment on the SrTiO₃ thin films prepared by radio frequency magnetron sputtering. *J. Appl. Phys.* 72(7) October, pp. 2895-2899.
- Nyaiesh, A. R. (1986) Target profile change during magnetron sputtering. *Vacuum* 36, pp. 307-309.
- Odaka, H. Iwata, S. Taga, N. Ohnishi, S. Kaneta, Y. and Shigesato, Y. (1997) Study on Electronic Structure and Optoelectronic Properties of Indium Oxide by First-Principles Calculations. *Jpn. J. Appl. Phys.* 36(9A) september, pp. 5551-5554.
- Odaka, H. Shigesato, Y. Murakami, T. and Iwata, S. (2001) Electronic structure analyses of Sn-doped In₂O₃. *Jpn. J. Appl. Phys.* 40(5A) May, pp. 3231-3235.
- Ohhata, Y. Shinoki, F. and Yoshida, S. (1979) *Thin Solid Films* 59, pp. 255-261)
- Ohring, M. (1992) *The materials science of thin films*. London, Academic Press, Inc. ISBN = 0-12-524990-X.

- O'Leary, S. K. Johnson, S. R. and Lim, P. K. (1997) The relationship between the distribution of electronic states and the optical absorption spectrum of an amorphous semiconductor: An empirical analysis. *J. Appl. Phys.* 82(7), pp. 3334-3340.
- Omata, T. Fujiwara, H. Otsuka-Yao-Matsuo, S. and Ono, N. (1998) *In-Situ* observation of the electrical conductivity upon release and uptake of oxygen in indium tin oxide sinter. *Jpn. J. Appl. Phys.* 37(3A), pp. 868-871.
- Ramaiah, K. S. Raja, V. S. Bhatnagar, A. K. Tomlinson, R. D. Pilkington, R. D. Hill, A. E. Chang, S. J. Su, Y. K. and Juang, F. S. (2000) Optical, structural and electrical properties of tin doped indium oxide thin films prepared by spray-pyrolysis technique. *Semicond. Sci. Technol.* 15, pp. 676-683.
- Rauf, I. A. (1993) Low resistivity and high mobility tin-doped indium oxide films. *Mater. Lett.* 18, pp. 123-127.
- Rauf, I. A. and Yuan, J. (1995) Effects of microstructure on the optical properties of tin-doped indium oxide thin films studied by electron energy loss spectroscopy. *Mater. Lett.* 25(5-6) December, pp. 217-222.
- Rohde, D. Kersten, H. Eggs, E. and Hippler, R. (1997) Thin film deposition by reactive magnetron sputtering: On the influence of target oxidation and its effect on surface properties *Thin Solid Films* 305(1-2) August, pp. 164-171.
- Paine, D. C. Whitson, T. Janiac, D. Beresford, R. and Yang, C. (1999) A study of low temperature crystallization amorphous thin film indium-tin-oxide. *J. Appl. Phys.* 85(12) June, pp. 8445-8450.
- Panicke, M. P. R. and Essinger, W. F. (1981) RF sputtering of yttria on indium tin oxide substrates. *J. Electrochem. Soc.* 128, pp. 1943-1947.
- Perkin Elmer, Überlingen. <http://www.spectroscopynow.com/>
- PDF (powder diffraction file), (1991) *Joint committee on powder diffraction standard*, ASTM, Philadelphia, PA, JCPDS-ICDD 6-416.
- Sartorius AG <http://www.sartorius.com/cgi-bin/wt/antik.pl?sprache=e>
- Schenkel, M. (1999) *Herstellung von transparenten Dünnschichtkondensatoren mit TiO₂ als Dielektrikum*. Diploma Thesis, Universität GH Essen (in German).
- Shigesato, Y. Takaki, S. and Haranou, T. (1991) Crystallinity and electrical properties of tin-doped indium oxide films deposited by DC magnetron sputtering. *Appl. Surf. Sci.* 48/49 pp. 269-275.

- Shigesato, Y. Hayashi, Y. and Haranoh, T. (1992) Doping mechanisms of tin-doped indium oxide films. *Appl. Phys. Lett.* 61(1), pp. 73-75.
- Shigesato, Y. Takaki, S. and Haranoh, T. (1992) Electrical and structural properties of low resistivity tin-doped indium oxide films. *J. Appl. Phys.* 71(7), pp. 3356-3364.
- Shigesato, Y. Paine, D. C. and Haynes, T. E. (1993) Lattice defects in O⁺ implanted tin-doped indium oxide films. *Jpn. J. Appl. Phys.* 32, pp. L1352-1355.
- Shigesato and Paine (1994) A microstructural study of low resistivity tin-doped indium oxide prepared by d.c. magnetron sputtering. *Thin solid films* 238 pp. 44-50.
- Song, P. K. Shigesato, Y. Yasui, I. Ow-Yang, C. and Paine, D. C. (1998) Study on crystallinity of tin-doped indium oxide films. *Jpn. J. Appl. Phys.* 37(4A), pp. 1870-1876.
- Song, P.K. Shigesato, Y. Kamei, M. and Yasui, I. (1999) Electrical and structural properties of tin-doped indium oxide films deposited by dc sputtering at room temperature. *Jpn. J. Appl. Phys.* 38(5A), pp. 2921-2927.
- Stenzel, O. (1996) *Das Dünnschichtspektrum: Ein Zugang von den Grundlagen zur Spezialliteratur*. Berlin Akademie-Verlag (in German).
- Szczyrbowski, J. Dietrich, A. and Hoffmann, H. (1983) Optical and electrical properties of RF-sputtered indium-tin oxide films. *Phys. Stat. Sol. (a)* 78, pp. 243-252.
- Tait, R. N. Smy, T. & Brett, M. J. (1990) *Thin Solid Films* 187, pp. 375-384.
- Tencor P-10 http://www.ifm.ethz.ch/mems/eq_tencor.htm
- Terzini, E. Nobile, G. Loreti, S. Minarini, C. Polichetti, T. and Thilakan, P. (1999) Influence of sputtering power and substrate temperature on the properties of RF magnetron sputtered indium tin oxide thin films. *Jpn. J. Appl. Phys.* 38(6A), pp. 3448-3452.
- Terzini, E. Thilakan, P. and Minarini, C. (2000) Properties of ITO thin films deposited by RF magnetron sputtering at elevated substrate temperature. *Materials Science and Engineering* B77(1) , pp. 110-114.
- Theiss, M. *Hard-and Software for Optical Spectroscopy*, Dr. Bernhard-Klein-Str. 110, 52078 Aachen, Germany, Available from: <http://www.mtheiss.com>.
- Thilakan, P. and Kumar, J. (1997) Studies on the preferred orientation changes and its influenced properties on ITO thin films. *Vacuum* 48(5) , pp. 463-466.

- Thornton, J. A. (1974) Influence of apparatus geometry and deposition conditions on the structure and topography of thick sputtered coatings. *J. Vac. Sci. Technol.* 11, pp. 666-670.
- Thornton, J. A. (1982) Coating deposition by sputtering. In: Bunshah, R. F. ed. *Deposition technologies for films and coatings*. New Jersey, Noyes Publications.
- Tominaga, K. Ueda, T. Ao, T. Kataoka, M. and Mori, I. (1996) ITO films prepared by facing target sputtering system. *Thin Solid Films* 281-282 (1-2) , pp.194-197.
- Uthanna, S. Reddy, P. S. Naidu, B. S. and Reddy, P. J. (1996) Physical investigations of dc magnetron sputtered indium tin oxide films. *Vacuum* 47(1), pp. 91-93.
- Van der Pauw, L. J. (1958) A method of measuring specific resistivity and Hall effect of discs of arbitrary shape. *Phil. Res. Rep.* 13 February, pp. 1-9; see also <http://www.eeel.nist.gov/812/hall.html>.
- Vink, T. J. Walrave, W. Daams, J. L. C. Baarslag, P. C. and Van Den Meerakker, J. E. A. M. (1995) On the homogeneity of sputter-deposited ITO films Part I. Stress and microstructure. *Thin Solid Films* 266(2), pp. 145-151.
- Vook, R. W. and Witt, F. (1965) Structure and annealing behavior of metal films deposited on substrates near 80°K. II. gold films on glass. *J. Vac. Sci. Tech.* 2(49), pp. 243-249.
- Weiher, R. L. and Ley, R. P. (1966) Optical properties of indium oxide. *J. Appl. Phys.* 37(1), pp. 299-302.
- Weijtens, C. H. L. (1990) *Indium tin oxide for solid-state image sensors*. PhD Thesis, TU Eindhoven
- Weijtens, C. H. L. and van Loon, P. A. C. (1991) influence of annealing on the optical properties of indium tin oxide. *Thin Solid Films* 196, pp.1-10.
- Wen, S. J. Couturier, G. Chaminade, J. P. Marquestaut, E. Claverie, J. and Hagenmuller, P. (1992) Electrical properties of pure In₂O₃ and Sn-doped In₂O₃ single crystals and ceramics. *J. Sol. State Chem.* 101, pp 203-210.
- Wu, W.-F. and Chiou, B. S. (1993) Effect of annealing on electrical and optical properties of RF magnetron sputtered indium tin oxide films. *Appl. Surf. Sci.* 68, pp. 497-504.
- Wu, W.-F. and Chiou, B.-S. (1994) properties of radio-frequency magnetron sputtered ITO films without *in-situ* substrate heating and post-deposition annealing. *Thin Solid Films* 247, pp. 201-207.

Yamada, N. Yasui, I. Shigesato, Y. Li, Y. Ujihira, Y. and Nomura, K. (1999) Doping Mechanisms of Sn in In_2O_3 Powder Studied Using ^{119}Sn Mössbauer Spectroscopy and X-Ray Diffraction. *Jpn. J. Appl. Phys.* 38(5A), pp. 2856-2862.

Yao, J. L. Hao, S, and Wilkinson, J. S. (1990) Indium tin oxide films by sequential evaporation. *Thin Solid Films* 189, pp. 227-233.

9 Acknowledgments

The experiments for this study were carried out in the thin-film technology workgroup of Professor Dieter Mergel in the Department of Physics in the University of Essen.

First I would like to express my deeply gratitude and appreciation to my supervisor, Prof. Dr. Dieter Mergel, for his kindly providing me the work and study opportunities in this workgroup, and for his insights, knowledgeable and strict guidance during this work.

I would like to acknowledge Prof. Dr. Rudolf Latz in the University of Applied Sciences of Gelsenkirchen for providing the profilometer for the film thickness measurement, and for his constructive and helpful suggestions on this work.

I am very grateful to my colleague Martin Jerman for his enthusiastic support and pleasant cooperation, and also for his carefully translating the summary of this work into German.

My sincere thanks are due to Andreas Schlarb for his kindly help, cooperation and friendship all the time.

To all members in our group I am very grateful for the excellent working atmosphere. Special thanks to Y. K. V. Reddy for his revising the manuscript.

I want to thank Dr. Martin Solkowski in the Department of Chemistry for the x-ray diffraction measurements. I would also thank Thorsten Wagner for the help of the AFM measurement and Barstian Weyers for his help to solve computer problems.

I would also sincerely thank all the people and friends who have helped me during this work.

Finally, I own special gratitude to my husband for his care and attention, and inspiring encouragement and support in these years.